Full title: Conjunctive spatial and idiothetic codes are topographically organized in the GABAergic cells of the lateral septum

Short title: Spatial and self-motion coding in the lateral septum

Authors: Suzanne van der Veldt[1], Guillaume Etter[1], Coralie-Anne Mosser[1], Frédéric Manseau[1], Sylvain Williams[1*]

[1] McGill University & Douglas Mental Health University Institute, Montreal, Canada
6875, Boul. LaSalle, Verdun (Quebec), H4H 1R3, Phone: 514 761-6131, Fax: 514 888-4067
*Corresponding author: sylvain.williams@mcgill.ca

Author contributions

SV and SW designed the study. SV performed surgeries, behavioral recording experiments, immunohistological experiments, and calcium data analysis. GE wrote code for MI calculation and Bayesian decoding and implanted mice for CA1 recordings. CAM implanted and recorded four mice that were used in the current study. FM performed and analyzed patch-clamp in vitro electrophysiology. SV and SW wrote the manuscript with inputs from all authors.

Abstract

The hippocampal spatial code's relevance for downstream neuronal populations – particularly its major subcortical output the lateral septum (LS) - is still poorly understood. Here, using calcium imaging combined with unbiased analytical methods, we functionally characterized and compared the spatial tuning of LS GABAergic cells to those of dorsal CA3 and CA1 cells. We identified a significant number of LS cells that are modulated by place, speed, acceleration, and direction, as well as conjunctions of these properties, directly comparable to hippocampal CA1 and CA3 spatially modulated cells. Interestingly, Bayesian decoding of position based on LS spatial cells reflected the animal's location as accurately as decoding using the activity of hippocampal pyramidal cells. A portion of LS cells showed stable spatial codes over the course of multiple days, potentially reflecting long-term episodic memory. The distributions of cells exhibiting these properties formed gradients along the anterior-posterior and dorsal-ventral axes of the LS, directly reflecting the topographical organization of hippocampal inputs to the LS. Finally, we show using trans-synaptic tracing that LS neurons receiving CA3 and CA1 excitatory input send projections to the hypothalamus and medial septum, regions that are not targeted directly by principal cells of the dorsal hippocampus. Together, our findings demonstrate that the LS accurately and robustly represents spatial, directional as well as self-motion information and is uniquely positioned to relay this information from the hippocampus to its downstream regions, thus occupying a key position within a distributed spatial memory network.

Abbreviations

LH lateral hypothalamus

LS lateral septum

MS medial septum

VTA ventral tegmental area

Introduction

The lateral septum (LS) is an anatomically complex structure uniquely positioned within a broader distributed spatial memory network. The LS consists almost exclusively of highly interconnected inhibitory GABAergic cells [1,2] that are densely innervated by the principal cells of the hippocampus [3,4], in contrast to the medial septum (MS), which receives inputs solely from the inhibitory neurons of the hippocampus [5]. Previous research has implicated the LS in a wide variety of behaviors, including spatial and working memory [6–10], regulation of feeding [11–14], anxiety [15–18], locomotion [19,20], and social behaviors [21–24].

To date, functional characterizations of the LS have often focused on the spatial coding properties of these neurons, primarily due to the extensive excitatory input from positionally-tuned hippocampal pyramidal neurons, commonly referred to as 'place cells' [4,24–26]. Yet, this body of work has not yet yielded a consensus. Several studies have reported place-like cells in the LS, but the number, information content, and stability vary widely from study to study [20,27–31], while others described a lack of canonical place cells altogether [4]. As previous studies often depended on variable criteria of what defines a place cell, estimates range from 5.3% [4] to 56.0% [20] of LS cells classified as spatially-modulated. Strikingly, even estimates by the same authors on data acquired from the same subjects engaging the same task ranged between 26.5% [32] to 56.0% [20]. When reported, LS place cells are typically described as of lesser quality than classic hippocampal place cells, with lower within-session stability and larger place fields [30,31]. Adding to this complexity, the LS is a large structure that is cytoarchitecturally subdivided into dorsal,

intermediate, and ventral subregions that spread across its anterior-posterior axis [5,26,33]. This suggests that, in addition to subjective criterias, the striking differences in LS spatial coding characteristics between studies may be in part a product of variations in recording locations within the region. In addition to positional information, LS neurons may also encode direction and self-motion information, including acceleration and velocity [20,30,31].

Beyond their spatial tuning properties, hippocampal place cells are also noted for the rapid reorganization of the place fields across time (on the order of days) and navigational contexts, a phenomenon termed remapping [34–38]. If the LS spatial code is directly inherited from its hippocampal inputs, one would expect comparable dynamics over a similar timescale. While the LS, similar to the hippocampus, has been implicated in behaviors that may require a stable representation of space over time, including context-reward [39,40], contextual fear conditioning [16,41–44], spatial learning and memory [32,45,46] remapping dynamics in the LS remain largely understudied. Thus, whether and how the LS spatial code changes across time is crucial to clarifying its relationship to the upstream hippocampal spatial code, with important implications for its involvement in this broader spatial memory network and how it supports behaviors across longer timescales.

To resolve these outstanding questions, we functionally characterize hippocampal connectivity of LS, and asked how information rich LS GABAergic neurons are in relation to their main pyramidal inputs in dorsal CA3 and CA1. To this end, we used head-mounted miniaturized microscopes to record ~2000 LS neurons across the anterior-posterior and dorsal-ventral axes of the LS, and compared their firing characteristics to pyramidal cells recorded in CA1 and CA3, as animals navigated linear track and open field environments. Results demonstrate that the LS accurately and robustly represents spatial, speed, and directional information in an anatomically-organized fashion. While the information of LS neurons is generally comparable to CA3 and CA1, our tracing studies suggest that LS

information is sent to downstream brain regions such as the MS and hypothalamus that are not directly connected by the principal cells of the dorsal hippocampus.

Results

LS GABAergic neurons exhibit stable spatial activity during alternation on a linear track

Previous electrophysiological studies of the LS disagree on both the proportion of place encoding cells in this region and their spatial content. Cells have been previously described to be of lower quality than the classically described hippocampal place cells [20,30,32] or to be virtually absent [4].

First, to assess the distribution of excitatory pyramidal inputs from each hippocampal subregion to the GABAergic cells of the LS, we injected a monosynaptic retrograde rabies tracer in dorsal LS (Fig 1A, S1 Fig, n = 5 mice), utilizing the monosynaptically restricted, Cre-dependent retrograde tracing features of this technique. We observed strong labelling of pyramidal neurons of the hippocampus in areas CA1 and CA3 (Fig 1B, S1 Fig). To investigate how the spatial coding properties of the LS compare to these main dorsal hippocampal inputs, we expressed the calcium (Ca^{2+}) indicator GCaMP6f in GABAergic cells of the LS or in the pyramidal cells of the dorsal CA1 (dCA1) and dorsal CA3 (dCA3) of mice (Fig 1C, S2 Fig, S3 Fig). We recorded Ca^{2+} activity from 1082 LS GABAergic neurons (n = 15 mice), 1251 dCA1 pyramidal cells (n = 5 mice) and 464 cells from dCA3 (n = 6 mice) from animals alternating on a linear track. We subsequently filtered and binarized the recorded calcium traces (S4A Fig) [47] and excluded periods of immobility (< $5 cm.s^{-1}$). Using an information-theoretic framework [48–50], we computed the mutual information (MI) between calcium activity and spatial location for each cell and expressed the results in

bits (S4B Fig). As we observed a significant correlation between probability of a cell to be active (P(A)) and MI (S4B Fig), we computed the MI value for 30 bootstrap samples (50% data sampling) and compared those to 30 circularly shuffled surrogates, which allowed us to compute significance of the MI value independently of P(A) (S4C-E Fig) [47]. We found that LS GABAergic activity was significantly spatially modulated ($p < .01$, Fig 1D, S4H Fig). Indeed, both mutual information and within-session stability was higher for spatially modulated LS cells compared to non-modulated cells (Mann-Whitney test, $p < .0001$, S4E-F Fig). Using this approach, a total of 43.90% of LS GABAergic cells qualified as spatially modulated (475/1082 cells), with LS cells similarly distributed along the linear track as place cells recorded from dorsal CA1 and dorsal CA3 (Fig 1E). In contrast to previous reports [4,20,32], we observed a significant difference in the proportion of spatially modulated cells across recording regions (LS: 43.57 ± 4.46 %; dCA1: 29.60 ± 2.99 %; dCA3: 27.01 ± 7.07 %; Kruskal-Wallis, H(3) = 6.212, $p = .0448$; Dunn's multiple comparisons test: LS-dCA1: $p = 0.1757$; LS-dCA3: $p = 0.1101$; Fig 1F). We found that within-session stability of spatially modulated cells (expressed as a correlation where 0 means no stability while 1 means perfectly stable) was significantly different between LS (0.44 ± .0165) and dCA3 (0.73 ± 0.26; Kruskal-Wallis, H(3) = 80.48, $p < .0001$; Dunn's multiple comparisons test, $p < .0001$), and between dCA1 and dCA3 ($p < .0001$; Fig 1G). Even though LS GABAergic cells are not fast spiking (S5 Fig, S6 Fig) [51], P(A) in LS ($0.02005 \pm 4.692 \times 10^{4}$) is higher than both dCA1 ($0.0094 \pm 2.544 \times 10^{4}$, Kruskal-Wallis, H(3) = 502.0, $p < .0001$; Dunn's multiple comparisons test, $p > .0001$) and dCA3 ($0.009225 \pm 3.759 \times 10^{4}$, $p < .0001$, S6A,B). Therefore, we assessed the mutual information in bits carried in each binarized event, and observed that the LS ($5.624 \times 10^{5} \pm 1.151 \times 10^{6}$ bits/binarized event) carries significantly less information per binarized event than CA1 ($1.430 \times 10^{4} \pm 1.613 \times 10^{6}$ bits/binarized event; Kruskal-Wallis, H(3) = 1288, $p < .0001$; Dunn's multiple comparisons test, $p < .0001$); and

CA3 ($1.130 \times 10^4 \pm 2.507 \times 10^6$; bits/binarized event; $p < .0001$, Fig 1H). To confirm that the observed differences in proportion of spatially modulated cells and within-session stability were not due to differences in P(A), we used an activity cut-off of P(A) > .001 and confirmed our previous results (S6D Fig).

In contrast to their omnidirectional firing properties in open field environments, hippocampal neurons rapidly develop strong directional selectivity on linear tracks [52–54]. To test whether the LS place code developed comparable directional selectivity, we ranked spatially modulated cells as a function of the difference between MI for left and right traversals (S7A-D Fig), and found LS cells tuned to the absolute location regardless of direction (7.67%, 83/1082 cells), while other cells were selective to the left- (15.52%, 168/1082 cells), or right-trajectories (22.08%, 239/1082 cells).

Fig 1: LS shares spatial coding characteristics with its main hippocampal inputs CA1 and CA3 during goal directed navigation in a 1D environment.

(A) Retrograde rabies tracing injection site, blue = DAPI staining, green = TVA.oG coupled to an enhanced green fluorescent protein (eGFP), red = Rabies coupled to mCherry, orange: starter cells expressing both TVA.oG.eGFP and Rabies.mCherry. (B) Retrograde labelling in the dorsal hippocampus, coronal section. Bottom left: example of mCherry-positive CA1 pyramidal cell, bottom right: mCherry-positive CA3 pyramidal cells, blue = DAPI staining, red = Rabies coupled to mCherry. (For additional images see S1 Fig). (C) Top: Diagram of one-photon calcium recording setup in LS, CA1 and CA3 in freely behaving mice, with GCaMP6f expression restricted to GABAergic cells in LS, and restricted to pyramidal cells in dorsal CA1 and CA3, middle: histological verification of implantation site (see also S2 Fig and S3 Fig) and bottom: extracted calcium transients for LS, CA1 and CA3. (D) Top: Linear track paradigm, with sucrose rewards on either end. Bottom: Probability of an example cell to be active given the location on the linear track (red) with 95% upper and lower percentile (grey). Examples shown are from two different LS mice, and a representative

177 spatially modulated cell from one CA1 and CA3 animal each. (E) Activity of cells sorted along
178 location in the maze for each region (blue, low; yellow, high). (F) Percent of significantly spatially
179 modulated cells for each animal for each recording region. LS: N = 15 mice. CA1: N = 5 mice, N = 6
180 mice. (G) Within-session stability of spatially modulated cells in each region active (LS: n = 475
181 cells, CA1: n = 336 cells, CA3: n = 143 cells). (H) MI per binarized event for all cells (LS: n = 1030
182 cells, n = 15 mice. CA1: n = 1251 cells, n = 5 mice, CA3: n = 464 cells, n = 6 mice). *, $p < .05$, **, p
183 < .01, ****, $p < .0001$. Test used in F-H: Kruskal-Wallis with Dunn's multiple comparisons test.
184
185 Previous studies have used decoding methods to predict behavioral variables from
186 calcium imaging data recorded in the hippocampus [34,38,55], yielding insights into the
187 amount of information encoded by a neuronal assembly. Here, we asked whether we could
188 reliably estimate the mouse location solely from LS neuronal activity patterns (Fig 2). Using
189 30 bootstrap samples of 60 cells (Fig 2B,C), decoding location using LS neuronal activity
190 significantly outperformed a decoder that was trained using shuffled data (paired t-test, $t(6) =$
191 13.56, $p < .0001$, Fig 2D), even when decreasing the number of neurons used (S8A,B Fig).
192 Similarly, a decoder trained using CA1 or CA3 data also yielded significantly less error than
193 one using shuffled surrogates (CA1: $t(4) = 7.558$, $p = .0016$; CA3: $t(3) = 3.233$, $p = .0481$,
194 Fig 2D, S8C,D Fig). While using a small bootstrap sample size allowed a fair comparison
195 between recording regions, it also induced higher error rates. To ensure the proper
196 functioning of our decoder, we confirmed that the decoding error decreased significantly
197 when increasing bootstrapped sample size (S8C,D Fig).
198 In order to compare decoding accuracy for LS, CA1 and CA3, a decoding score was
199 computed (Fig 2E, see methods), and we found that LS significantly outperformed CA3 (one-
200 way ANOVA, $F(2,13) = 6.277$, $p = .0124$; Holm-Sidak's multiple comparisons test $p < .05$),
201 but not CA1. Overall, spatially modulated cells recorded in LS were significantly more active
202 than those recorded in the hippocampus ($H(3) = 155.1$, $p < .0001$, S5A,B Fig), which could

be a contributing factor to the overall higher decoding accuracy using LS cells. To confirm that the differences observed in decoding error are not due to the inclusion of a large number of pseudo-silent cells in the dCA1 or dCA3 bootstrapped samples, we confirmed our findings using an activity cut-off of P(A) > .001 (S8E-F). Similarly, to confirm that the observed differences in decoding error are not due to the use of a temporal smoothing window, we replicated our results using a decoder that omitted temporal filtering (S8G-H).

Fig 2: Location can be reliably decoded from lateral septum GABAergic cells.

(A) Top: Posterior probabilities for each frame estimated from binarized calcium activity, bottom: corresponding actual (green) and decoded (red) location. (B) Schematic representation of bootstrapping approach. (C) Method for computing mean Euclidean distance decoding error (in cm) for each bootstrapped estimate. (D) Decoding error for actual vs shuffled dataset (30 bootstrapped samples of 60 cells, LS: N = 7 mice, CA1: N = 5 mice, CA3: LS = 4 mice). (E) Mean decoding score for each region. *, $p < .05$, **, $p < .01$, ****, $p < .0001$, Test used in D, paired t-test, E, one-way ANOVA, Holm-Sidak's multiple comparisons test.

LS GABAergic neurons exhibit stable spatial activity during free exploration in a 2D environment

In order to assess spatial coding during free exploration in a two-dimensional environment, we recorded Ca^{2+} activity of 1899 GABAergic neurons in 28 mice implanted in distinct subregions of the LS, while the animals were freely exploring a novel open field. Out of 1899 recorded cells, 37.80% (718/1899 cells, n = 28 mice) of LS cells displayed significant spatial information ($p < .01$; Fig 3A-B, S9 Fig), as compared to 31.33% (323/1031 cells, n = 6 mice) in CA1 and 25.84% (138/534 cells, n = 8 mice) CA3 cells. Despite the LS' known involvement in feeding-related behaviors [11–14], we did not observe any increased number of cells with firing fields around food zones, nor did we observe overrepresentation of objects

or walls (S10 Fig). To assess reward-modulation in the context of increased task demand, we assessed spatial firing of LS GABAergic neurons recorded while animals performed a delayed non-matching to place task in a T-maze, but did not observe any significant reward code compared to shuffled surrogates (S11 Fig).

With theta-rhythmic cells in the LS having higher firing rates than theta-rhythm independent cells [56], and the suggestion that theta-rhythmic cells could receive direct hippocampal inputs (though see [57,58]), we asked whether LS cells with higher firing rates were also more likely to be spatially modulated. Indeed, spatially-modulated cells were significantly more active than non-modulated cells (Mann-Whitney test, U = 342219, $p < .0001$; S9G-H Fig) and displayed a higher bursting index, defined as the probability of a cell being active, given it was already in an active state, or $P(A_t|A_{t-1})$, than non spatially modulated cells (Mann-Whitney test, U = 368276, $p < .0001$; S9H Fig).

We compared the place field properties of cells recorded in LS to those of dorsal CA1 and CA3 (Fig 3). For each animal, we computed the portion of significantly positionally modulated cells per region, which was not significantly different across LS (36.71 ± 2.16 %), dCA1 (38.32 ± 9.36 %), and dCA3 (28.39 ± 6.73 %; one-way ANOVA, F(2,39) = 1.105, $p = .3414$; Fig 3B). We computed the information for each binarized event, and observed that the LS ($1.020 \times 10^4 \pm 7.56 \times 10^7$ bits/binarized event) carries significantly less information per binarized event than CA1 ($1.200 \times 10^4 \pm 1.067 \times 10^6$ bits/binarized event; Kruskal-Wallis, H(3) = 264.6, $p < .0001$; Dunn's multiple comparisons test, $p < .0001$) and CA3 ($1.199 \times 10^4 \pm 1.605 \times 10^6$ bits/binarized event; $p < .0001$). As expected on the basis of prior results [4,28,30,31], within-session stability of LS cells (0.31 ± 0.011) was significantly lower than that of spatially modulated cells recorded in CA1 (0.44 ± 0.017; Kruskal-Wallis, H(3) = 89.52, $p < .0001$; Dunn's multiple comparisons test, $p < .0001$) and CA3 (0.56 ± 0.027; $p < .0001$; Fig 3D), and place fields were more dispersed (LS: 14.47 ± 0.13 cm; CA1: 12.00 ±

0.207 cm; CA3: 10.61 ± 0.35 cm; Kruskal-Wallis, H(3) = 155.7, $p < .0001$, Fig 3E). Similar to recordings in a 1D environment, we observed large differences in P(A) between spatially modulated cells recorded from LS and those from dorsal CA1 and CA3 (S12A Fig). Therefore, we also assessed for each region the proportion of spatially modulated cells, split-half stability and mean-dispersion using an activity cut-off of P(A) > .001, and confirmed our results (S12B Fig).

When decoding the location of the animals using bootstrap samples of 80 cells from each region (Fig 3F), decoding error was significantly lower in LS (20.16 ± 1.48 cm) compared to shuffled surrogates (26.03 ± 0.84 cm; two-way RM ANOVA, F(1,13) = 89.09, $p < .0001$ for main effect of shuffle), even when decreasing the number of neurons used to only 40 neurons (S13A,B). Omission of temporal filtering recapitulated these results (S13E Fig). The same held true for decoders trained using CA1 or CA3 data respectively (S13C,D). Strikingly, a decoder trained on data from LS does not perform significantly worse than a decoder trained on CA1 or CA3 data (F(2,13) = 2.186, $p = 0.2384$ for main effect of region; Fig 3H). Similarly to recordings on the linear track, we used an activity cut-off of P(A) > .001 to confirm that the differences observed in decoding error between regions are not due to the inclusion of a large number of pseudo-silent cells in the bootstrapped sample (S13F Fig).

Fig 3: LS shares spatial coding characteristics with its main hippocampal inputs CA1 and CA3 during free exploration in a 2D environment.

(A) Example tuning maps of spatially modulated cells recorded from LS, dorsal CA1 and dorsal CA3 in a 45 x 45 cm open field (3 x 3 cm bins). (B) Proportion of spatial cells per animal (LS: n = 28 mice; dCA1: n = 6 mice; dCA3: n = 8 mice). (C) MI (bits) per binarized event for all cells recorded from each region (LS: n = 1899 cells from n = 28 mice; dCA1: n = 1031 cells, n = 6 mice; dCA3: n = 534 cells, n = 8 mice). (D) Within session stability for spatial cells (LS: n = 734 spatial cells from n = 28 mice; dCA1: n = 424 spatial cells, n = 6 mice; dCA3: n = 138 spatial cells, n = 7 mice). (E) Left:

mean dispersion computation, right: mean dispersion for all spatial cells recorded from each region. (F) Method for computing the mean decoding error. (G) Bootstrapping approach using 80 randomly selected cells, for 30 bootstrapped samples. (H) Mean decoding error for LS (n = 8 mice), CA1 (n = 4 mice) and CA3 (n = 4 mice). *1, $p < .05$, **, $p < .01$, ****, $p < .0001$, Test used in B, one-way ANOVA, C-E, Kruskal-Wallis, Dunn's multiple comparison test, H, two-way ANOVA, Sidak's multiple comparisons test.

A subset of LS cells has stable spatial representations up to 8 days, similar to CA1

To test whether the LS and the hippocampus exhibit comparable evolutions of their spatial code over time, we recorded from animals implanted in LS and dorsal CA1 in a novel open field over both short (3 days) and longer timescales (8 days, Fig 4, S14 Fig). We assessed the stability of the spatial map across sessions, and observed a subset of LS spatially modulated cells that were stable over time (Fig 4B). Correlating the tuning maps of aligned LS cell pairs over days lead to a significant increase in mean pairwise correlation value over days (two-way ANOVA, $F(2, 808) = 3.259$, $p = 0.0389$, main effect of time) with LS cells being statistically more stable than shuffled comparisons ($F(2,808) = 277.0$, $p < .0001$, main effect of shuffling, Fig 4C, S14C Fig). We observed the opposite pattern for pyramidal cells recorded from dorsal CA1, with a significant decrease in mean pairwise correlation value over days (two-way ANOVA, $F(2,766) = 33.47$, $p < 0.0001$ main effect of time, $F(1,766) = 319.8$, $p < 0.0001$ main effect of shuffle, Fig 4C). For cells recorded in the LS, we observed the strongest within-session stability on day 3 (Kruskal-Wallis, $H(4) = 19.16$, $p = 0.0003$; S14E Fig), as well as an increase in spatial information (Kruskal-Wallis, $H(4) = 13.27$, $p = 0.0041$; S14B Fig). There was no significant increase in the proportion of stable cell pairs over subsequent days (one-way ANOVA, $F(3) = .400$, $p = .9537$, S14D Fig), or the proportion of spatially modulated cells per animal for each days (one-way ANOVA, $F(3,16) = 1.618$, $p = .2247$, S14E Fig).

We next assessed the significant tuning map correlations on subsequent day-pairs for those cells that were significantly spatially modulated on day 1 and were subsequently found on all recording days (Fig 4D), as well as those that passed our criteria for spatial modulation on all days (Fig 4E). We then compared the place field correlation for different day pairs ($F(5,363) = 2.625$, $p = .0239$, interaction effect), and we found that on shorter timescales, tuning maps for LS cells (0.316 ± 0.0507) are significantly less correlated than CA1 (0.497 ± 0.0411; Fisher's LSD day 1-2, $p = 0.0153$, Fig 4F). On the other hand, the correlation for day pairs 3-8 is higher for the LS (0.369 ± 0.0513) compared to dorsal CA1 (0.174 ± 0.0669; Fisher's LSD, $p = 0.0098$; Fig 4F). Together, this suggests that a subset of LS spatial cells encodes spatial information over longer periods of time.

Fig 4: LS place code remains similar to CA1 over longer periods of time.

(A) Experimental setup (top) with a representative example of an animal implanted in the LS, and aligned spatial footprints of cells recorded over days (bottom). (B) Tuning maps for two sets of stable cells recorded over all days, with each row being one aligned cell. Within-session correlation indicated in blue. Tuning map correlation indicated at the bottom in red. (C) Significant tuning map correlation for aligned cell-pairs (black) versus shuffled pairs (red) for progressive days for LS (day 1-2, n = 157 cells; day 2-3, n = 122 cells; day 3-8, n = 129 cells; n = 5 mice) and dorsal CA1 (day 1-2, n = 165 cells; day 2-3, n = 122 cells; day 3-8, n = 99 cells ; n = 3 mice). (D) Significant tuning map correlations for all cells found on all days for LS (n = 84) and CA1 (n = 86). (E) Matrix of mean tuning map correlation for all aligned cells that were significantly spatially modulated on each day, for LS (n = 23-37 cells, n = 5 mice) and CA1 (n = 23 - 41 cells, n = 3 mice). (F) Mean tuning map correlation for data shown in E. *, $p < .05$, **, $p < .01$, ****, $p < .0001$. Test used in C, two-way ANOVA, with Sidak's multiple comparisons test, F, two-way ANOVA, with Fisher's LSD post-hoc test.

LS represents direction, velocity, and acceleration information

In CA1, place cells have been found to carry directional [59–61] and speed-related information [61–64]. Previous studies found that subsets of LS neurons show some degree of modulation by direction of travel [31] as well as velocity and acceleration [20] through correlative measures in spatial alternation or T-maze navigation tasks, where the relationship between cell activity patterns and movement-associated variables may be confounded with task-dependent variables. Here, we again employed an information-theoretic approach to compute the MI between calcium activity and each of these self-motion correlates in a subset of mice recorded during a 15 min free foraging task in the open field. We found that 28.13% of LS cells are significantly modulated by head-direction (346/1230 cells, n =19 mice, Fig 5A, S15 Fig), 18.70% by velocity (230/1230 cells, Fig 5C) and 24.63% by acceleration (303/1230 cells, Fig 5E). We assessed the stability of LS directional and self-motion tuning over short (3 days) and longer timescales (8 days, S16 Fig), and we observed a subset of LS directionally modulated cells that were stable over time (S16A Fig). Mean tuning vectors correlation of aligned LS cell pairs significantly increased over days (two-way ANOVA, $F(2,774) = 3.682$, $p = 0.0256$, main effect of time) with LS cells being statistically more stable than shuffled surrogates ($F(1,774) = 54{,}42$, $p < .0001$, main effect of shuffling, S16C Fig). For velocity or acceleration tuning, we did not observe such stable tuning over time (two-way ANOVA, velocity: $F(1,506) = 2.609$, $p = .1069$, acceleration: $F(1,320) = .1986$, $p = .6561$, main effect of shuffle, S16D,E).

We compared the proportion of LS cells significantly modulated by each of these variables with the proportion of those cell-types found in dCA1 and dCA3. The proportion of directionally modulated cells was significantly different across regions (LS: 27.89 ± 2.16, dCA1: 46.11 ± 4.98, dCA3: 28.92 ± 4.52; Kruskal-Wallis, $H(3) = 6.586$, $p = .0371$, Fig 5B) with a higher proportion of directionally modulated cells in CA1 as compared to LS (Dunn's multiple comparisons test, $p = .0340$; Fig 5B). The proportion of velocity encoding cells was

not significantly different between LS (20.43 ± 2.598), CA1 (24.38 ± 7.73), or CA3 (20.04 ± 3.62; Kruskal-Wallis, H(3) = 0.1016, p = 0.9504, Fig 5D). Similarly, no difference was found in the proportion of acceleration encoding cells between LS (25.11 ± 2.34), CA1 (24.14 ± 4.13), or CA3 (22.60 ± 2.98, Kruskal-Wallis, H(3) = 0.3337, p = 0.8463, Fig 5F). We found a proportion of cells that were significantly tuned to more than one of these variables in both LS as well as dCA1 and dCA3 (Fig 5G, S15A-D Fig, S17 Fig), with 22.03% of LS cells (271/1230 cells) encoding more than one modality (Fig 5H). Together, this conjunctive coding for location, directionality, and velocity indicates that LS cells fire in response to more complex navigational features, similarly to the hippocampus.

Fig 5: LS GABAergic cells encode direction, speed, and acceleration.

(A) Left: Activity of an example LS neuron during free exploration in an open field, top: head direction (HD, red), middle: binarized activity (yellow), bottom: raw calcium activity (blue). Right: Corresponding polar plot indicating the probability of the cell being active as a function of the animals' HD with (black, p(active | direction), red lines indicate 95% upper and lower percentile. Blue line indicates the normalized time spent for each direction. MI calculated using 40 bins of 9°. S15 Fig. (B) Proportion of significantly directionally modulated cells in LS, dCA1 and dCA3. (C) Left: Activity of an example LS neuron during free exploration modulated by velocity (top, red), middle: binarized activity (yellow), bottom: raw calcium activity (blue). Right: Tuning curve for velocity for the example cell (red) with 95% upper and lower percentile in grey. MI calculated using 20 bins. (D) Proportion of significantly speed modulated cells in LS, dCA1 and dCA3. (E) Left: Activity of an example LS neuron during free exploration modulated by acceleration (top, red), middle: binarized activity (yellow), bottom: raw calcium activity (blue). Right: Tuning curve for acceleration for the example cell (red) with 95% upper and lower percentile in grey. MI calculated using 20 bins. (F) Comparison of proportions of significantly modulated cells for each region. (G) Example of an LS cell that is both significantly head direction modulated (left), as well as spatially modulated (right). (H) Left: Proportion of cells that are significantly modulated by only one modality (grey), two

385 modalities (yellow), three (red) or all 4 of the investigated variables (black). The number above the
386 bars indicates the absolute number of cells found to be modulated in the total population (n = 1230
387 cells, n = 19 mice). Right: absolute proportion of cells modulated by any combination of variables.
388 Test used in B, D, F: Kruskal-Wallis test with Dunn's multiple comparisons test. *, $p < .05$. D =
389 direction, A = acceleration, S = spatial coding, V = velocity.
390
391 To understand the function of this downstream copy of the hippocampal spatial code,
392 we assessed the downstream targets of the dCA1/dCA3 to LS projection. First, we used a
393 Cre-dependent, anterograde tracing approach to confirm LS projections to the hypothalamus
394 and ventral tegmental area in the mouse (S18 Fig), as it was initially described in the rat
395 [3,5,25]. Next, we leveraged the anterograde transsynaptic properties of Cre-expressing
396 AAV1 viral vector [65] and assessed the targets of the dorsal CA1-lateral septum (dCA1-LS)
397 as well as dorsal CA3-LS (dCA3-LS) projections (Fig 6). For either dCA1 or dCA3
398 injections (Fig 6A, S19 Fig), we observed a direct pathway from the principal cells of the
399 hippocampus, via the LS, leading to dense innervation of the medial septum (Fig 6B) and the
400 hypothalamic regions (Fig 6C). We observed that dCA1-LS preferentially targets the LH, and
401 dCA3-LS targets the hypothalamus more broadly as well as the nuclei of the medial zone.
402 Whether the GABAergic cells of the lateral septum form functional synapses at the level of
403 the medial septum/diagonal band complex is debated [5,26,66–68]. Thus, in order to
404 determine whether the projections observed at the level of the MS with both our anterograde
405 tracing approaches constituted passing fibers or synaptic connections, we used an AAV-Flex-
406 Synaptag [69], a Cre-dependent viral construct to express mRuby in the cytosol and eGFP
407 bound to synaptophysin, a protein primarily expressed in the presynaptic endings of cells
408 participating in synaptic transmission (Fig 6D). For this, we used a CaMKIIα-Cre mouse line,
409 expressing Cre only in CAMKII-positive cells, a marker that is abundant in the GABAergic
410 cells of the LS but absent in the MS, thereby preventing any unspecific labelling. After

411 expressing AAV-Flex-Synaptag in the intermediate LS, we observed significant
412 synaptophysin-bound projections in the MS (Fig 6E), confirming the existence of a synaptic
413 interface between the LS and the MS. Together, our work shows that LS receives direct
414 inputs from dorsal CA1 and CA3 and in turn projects to regions that are not directly receiving
415 inputs from the hippocampus itself (Fig 6F).
416
417 **Fig 6: LS cells receiving hippocampal inputs project directly to hypothalamus and medial**
418 **septum.**
419 (A) Diagram of dual-viral injection strategy for anterograde transsynaptic tracing. The diagram is
420 based on dorsal CA1 targeted injection, dCA3 is also used for injections, together with coronal
421 sections showing primary injection sites in dorsal CA1 (top) or dorsal CA3 (bottom). Red = tdTom
422 expression, blue = DAPI, with zoomed images showing tdTom-positive cell bodies are predominantly
423 located in the pyramidal layer (bottom). For additional images of spread of injection, see S19 Fig. (B)
424 eYFP-positive cell bodies at the anterior dorsal LS and fibers at the level of the medial septum
425 following dCA1 injection (left) and dCA3 injection (right). Inset left: eYFP-positive fibers at the level
426 of MS. (C) eYFP positive axons are seen bilaterally at the level of the lateral hypothalamus following
427 dCA1 injection (left) and dCA3 injection (right). (D) Injection strategy for Cre-dependent AAV.
428 Synaptag mediated tracing in the LS. (E) Coronal section of dorsal LS, with synaptophysin-bound
429 eYFP at the MS. Top right: Zoomed images showing transduction at the injection site. Bottom right:
430 eYFP-positive fibers. (F) Schematic with proposed connections of the LS within the hippocampal
431 network. Scale bars: B, left and right: 800 μm. C, left and right: 500 μm. DM = dorsomedial
432 hypothalamic nucleus, LH = lateral hypothalamus.
433
434 **LS-cells coding for space, direction and self-motion are non-uniformly distributed**
435 To map out the monosynaptic connections between hippocampal and LS neurons, we injected
436 the anterograde transsynaptic Cre-expressing AAV1 viral vector [65], in either dCA1 or
437 dCA3 (S19 Fig, S20A Fig). We subsequently injected a Cre-dependent eYFP expressing

virus in the LS to visualize cells that receive direct hippocampal input (S20B Fig). Importantly, this approach allowed us to quantify the cells along the LS anterior-posterior and dorsal-ventral axis receiving direct hippocampal inputs, and assess their distribution density within the anterior regions of the LS (Bregma +1.0 to 0.0 anterior-posterior). Because we can only observe secondary labelled cell-bodies at locations where there was infusion of the secondary, Cre-dependent virus, we used a relatively large injection volume (total 800 nL, targeted at the intermediate LS). Both dorsal dCA1 and dCA3 injections resulted in a majority of labelled LS cell bodies in dorsal regions compared to intermediate and ventral LS (S20D-F Fig). Hence, LS neurons receiving direct inputs from dorsal CA1 and CA3 appear to be localized at more dorsal-posterior regions as compared to more ventral-anterior regions of LS.

Next, we examined whether spatially modulated cells recorded in LS had spatial properties that were dependent on the localization of their recording. To measure this, we classified the location of GRIN lens implants along the dorsal-ventral and anterior-posterior axis (Fig 7A). Post-mortem histological verification of GRIN lens implant combined with within-animal analysis of the location of recorded cells enabled us to approximate the location of each cell (Fig 7B). While we observed no differences in cell activity characteristics, such as bursting index or activity probability along the anterior-posterior axis, medial-lateral or dorsal-ventral axis (S21 Fig), we found a pronounced increase in the portion of stable spatially modulated cells (within-session stability > .5) along the anterior-posterior axis (linear regression, $R^2 = 0.1071$, $p = 0.0022$, the proportion of stable cells per 0.2 mm bin per animal, n = 24 mice, Fig 7C). We observed a similar gradient along the dorsal-ventral axis, with a larger proportion of stable spatial cells found at the more dorsal regions of the LS, although this trend failed to reach significance (linear regression, $R^2 = 0.1399$, $p = .0718$, n = 24 mice, Fig 7C). Taken together, these data strongly suggest that regions of the LS that

receive stronger innervation from the dorsal hippocampus have a larger proportion of cells that reliably encode space. This suggests that this information could be directly inherited from the hippocampus, which should be tested using targeted inactivation of the hippocampal pyramidal inputs to LS.

We also assessed the topographical distribution of direction and self-motion tuned cells within the LS. We observed a relatively strong dorsal-ventral gradient in the distribution of stable (within-session stability > .5) directionally modulated cells (linear regression, R^2 = 0.3837, p = 0.0061, n = 17 mice, Fig 7C), with most directionally modulated cells located at the more dorsal regions of the LS, but we did not observe such a gradient along the anterior-posterior axis (linear regression, R^2 = 0.0544, p = .0615, n = 24 mice, Fig 7C). Velocity modulated cells were primarily found at the ventral pole of the LS (linear regression, R^2 = 0.1836, p = 0.0367, n = 24 mice), but no such gradient was found along the anterior-posterior axis (linear regression, R^2 = .00348 p = .0874, n = 24 mice). Acceleration-modulated cells were found evenly distributed throughout the LS (DV: R^2 = .0133, p = .2928; AP: R^2 = .01332, p = .2929, n = 24 mice).

Fig 7: LS-cells coding for space, direction and self-motion correlates are non-uniformly distributed along the dorsal-ventral and anterior-posterior axis.

(A) Strategy to record from different anterior-posterior levels in LS (left) and implantation sites covered. (B) Strategy to approximate cell location. Background: Maximal projection of representative recording, red: outline of approximated GRIN lens position, white: distance from the centre of the GRIN lens to the cells of interest. (C) Top: For .2 mm bins along dorsal-ventral axis, proportion of stable (within-session stability > .5) spatially modulated cells (n = 24 mice), directionally modulated cells (n = 17 mice), velocity cells (n = 24 mice) and acceleration cells (n = 24 mice) respectively. Bottom: Same as top for anterior-posterior axis. Each red dot represents the average per animal per

bin along the anterior-posterior axis (left) and along the dorsal-ventral axis. Black lines indicate 95% confidence intervals. *, $p < .05$, **, $p < .01$, Test used in C: linear regression.

Discussion

While spatial coding has been extensively characterized in the hippocampal formation, how downstream regions integrate this information has only recently begun to receive attention. The LS has re-emerged as a critical region implicated in a space encoding network, although electrophysiological recordings of the LS in rats have led to disparate estimates of the quantity and quality of place cells in the region [4,20,28,32]: LS place cells recorded on a circular track were described to be almost absent [4], but were found to be abundant in reward-seeking tasks [20,32]. Using a large calcium imaging dataset and unbiased information metric and decoding approaches, we found that 37.80% of GABAergic LS cells robustly code for space during free exploration in an open field and 43.90% of cells during linear track alternation. One of the major features of the linear track is the induction of directional place fields in LS, which may underlie some of the differences we observed in 1D versus 2D spatial coding characteristics.

In addition to spatial information, we found that the LS also reliably encodes velocity, acceleration, and directional information, suggesting that the LS encodes more complex navigational features than previously thought. Neuronal representations in the hippocampus have been found to change over time, with place code ensembles changing rapidly: an estimated ~40% [34] to ~75-85% [38] of CA1 neurons were found to remap over days. The stability of the LS spatial code has received little attention to date. In the current study, we found a subpopulation of cells in the posterior LS that display stable place fields over eight days. The functional role of such stability remains to be elucidated. One possibility is that this ensemble may mediate the stable encoding of contexts over longer durations of time, which

513 could account for the critical importance of the LS for a number of spatial behaviors,
514 including contextual fear conditioning [16,41–44], context-reward associations [39,40] and
515 radial-maze navigation tasks [45,46].

516 Similar to the change in properties of hippocampal place cells along the dorsal-ventral
517 axis [70,71], previous work has hinted at a dorsal to ventral organization of the LS place
518 code: electrophysiology studies recorded a slightly larger proportion of LS place cells in the
519 more dorsal regions [30]. A complementary anatomical microstructure has been previously
520 described for the rate-independent phase code in the LS, where the strength of the phase code
521 increased as a function of recording depth along the dorsal-ventral axis [4]. Here we find that
522 lateral septal spatially modulated cells are arranged along an anterior-posterior gradient
523 similar to the gradient of hippocampal inputs into the LS – a finding that helps to reconcile
524 the variation in previously reported estimates of spatial cells in the LS, which ranged between
525 5.3% of cells recorded along the dorsal-ventral axis [4] up to 56% recorded at the most dorsal
526 level of the LS [20]. This pattern suggests that the inhibitory neurons of the LS may inherit a
527 place code from the hippocampus, with subregions receiving dorsal hippocampal inputs being
528 most similar to the classical hippocampal place cells. Interestingly, this is not the only case of
529 GABAergic neurons inheriting some spatial properties from hippocampal pyramidal cells:
530 interneurons within CA1 have been shown to exhibit significant spatial modulation and
531 comparable information as pyramidal place cells, although with a higher firing rate and
532 greater spatial dispersion [72]. It should be considered that, although the hippocampus seems
533 a likely source of the positional information encoded by the LS, this information could also
534 arise from incoming projections from any other region projecting to LS, such as the
535 entorhinal cortex [5,25] which could account for part of head direction and velocity tuning.

536 In addition to spatial modulation of LS cells, we observed a significant number of
537 velocity and acceleration modulated cells in the LS. These cells have been previously

538 described by others on the basis of correlative measures, although estimated proportions vary
539 widely: for velocity tuning in reward-seeking tasks, estimates range from almost absent [4] to
540 almost 60% of cells [20]. For acceleration, approximately 45% of LS cells were found to
541 show some degree of correlation, with almost 30% of recorded cells correlated with both
542 speed and acceleration [20]. Here, using information metrics and a free exploration task in
543 which firing characteristics are not confounded with task parameters, we find that 18.70% of
544 cells were modulated by velocity and 24.63% by acceleration. Cells reliably coding for both
545 velocity and acceleration were relatively rare (2%). Velocity and acceleration cells were
546 distributed dissimilarly in the LS, with velocity cells being more abundant towards the ventral
547 pole, whereas acceleration modulated cells were found to be distributed equally. This raises
548 the question whether velocity and acceleration information are inherited from different areas
549 upstream of the LS. Interestingly, cells coding for direction were more abundant towards the
550 dorsal portion of the LS, but distributed equally along the anterior-posterior axis. Previous
551 studies have identified classical head direction cells in multiple, well-described circuits,
552 including the postsubiculum [73,74], anterodorsal thalamic nucleus [75], mammillary bodies
553 [76], entorhinal cortex [77], retrosplenial cortex [78,79] and parasubiculum [80,81]. A likely
554 source of directional information to the LS is the entorhinal cortex [82]. Our work supports
555 the perspective that LS neurons combine a wide range of modalities and may form a complex
556 representation of context over longer timescales than previously reported. In addition to
557 space, velocity, and reward information, hippocampal pyramidal cells have been shown to
558 encode variables such as time [83,84], odor [85,86] and sound frequency [87]. Whether this
559 information is also relayed to the LS remains to be elucidated. Despite this
560 interconnectedness with the LH and previous reports of LS place cells being skewed towards
561 reward in a spatial navigation task [32], we did not observe any overrepresentation of LS

562 spatially modulated cells around food zones during free exploration or around the reward
563 zone in a T-maze non-match-to-place paradigm.

564 The question arises of what the function could be of having a region downstream of
565 the hippocampus that expresses such seemingly similar coding characteristics. Previous work
566 estimated the convergence of hippocampal efferents onto LS neurons to be 20 to 800 times
567 more dense than to any of its cortical targets [4]. Understanding how individual LS neurons
568 integrate the thousands of synaptic inputs they receive from these hippocampal pyramidal
569 neurons will be critical to understanding how the hippocampal map is processed downstream.
570 Through the process of synaptic integration, a target neuron can fire an action potential upon
571 receiving sufficient temporally coincidental excitatory input on its dendrites. The activation
572 of a LS neuron could thus require multiple hippocampal pyramidal cells to spike
573 simultaneously or in close temporal proximity. Hippocampal pyramidal cells will fire
574 concomitantly when their place fields are in overlapping regions or in close vicinity of
575 another. Due to the high interconnectivity of LS GABAergic neurons [88,89], the activation
576 of one LS cell could subsequently lead to the inhibition of other neurons in the nucleus
577 [24,90], thereby reducing noise. Thus, through this process of coincidence detection and
578 recurrent inhibition, the spatial map could converge to be represented by a much lower
579 number of cells. As such, the LS could accurately convey hippocampal information to
580 downstream regions using a much more distributed code, and thereby support more effective
581 information transmission and associative learning [91,92].

582 Finally, our tracing work shows LS cells receiving hippocampal inputs from principal
583 cells in dorsal CA1 and CA3 in turn project directly to the LH and the MS. Although the
584 existence of an LS-MS projection has long been debated [5,26,66,68,93], we observed both
585 dense innervation at the level of the MS after transduction of dCA1-input and dCA3-input
586 receiving LS cells, as well as synaptic densities between the LS and MS. This suggests that

principal cells of the hippocampus send indirect projections to the MS through LS neurons. This circuit is complementary to the well-described projections of hippocampal GABAergic interneurons directly to the MS which may play a key role in theta rhythm generation [94,95]. The MS plays a role in generating and propagating theta rhythms throughout the hippocampal formation [96–98], which in turn organizes hippocampal place cell activity [99], as well as a behavioral role in the initiation and velocity of locomotion [100,101]. One hypothesis is that the information on locomotion-related information reported in specific MS neurons [101] may originate from the LS. Moreover, we observed a direct projection from CA1 and CA3, via the LS, to the hypothalamus. This pathway was previously shown by previously using non-specific monosynaptic anterograde tracing [3], with similar unilateral projection patterns for CA1 and bilaterally for CA3 as described here. Here we show for the first time that the same LS neurons that receive inputs from dorsal CA1 and CA3 project directly to the hypothalamus. The hypothalamus is a highly connected region known for its role in regulating feeding behaviors [102], arousal and motivation [103], and more recently learning and memory [104–107]. Additionally, the LH is crucial for the control of locomotion [108–111] and thought to mediate motivational and goal-directed processes underlying feeding [12,102,112,113].

Together, our findings show that GABAergic cells of the LS may provide the hypothalamus and MS with information about location, direction, and speed, and therefore constitute a core node within a distributed spatial memory network. Within this network, the LS may be necessary for the translation of spatial information to goal-directed or environmentally appropriate actions necessary for survival.

Methods

612 **Ethics statement**

613 All procedures were approved by the McGill University and Douglas Hospital Research
614 Centre Animal Use and Care Committee and in accordance with the Canadian Council on
615 Animal Care.

616

617 **Animals**

618 Naive mice (8-16 weeks old) were housed individually on a 12-hour light/dark cycle at 22°C
619 and 40% humidity with food and water ad libitum. All experiments were carried out during
620 the light portion of the light/dark cycle. Both male and female mice were used for this study.

621

622 **Virus injections**

623 Mice, 8-16 weeks old, were anesthetized with isoflurane (5% induction, 0.5-2% maintenance)
624 and placed in a stereotaxic frame (David Kopf Instruments). Body temperature was
625 maintained with a heating pad, and eyes were hydrated with gel (Optixcare). Carprofen (10
626 ml/kg) was administered subcutaneously. All viral injections were performed using a glass
627 pipette connected to a Nanoject III (Drummond) injector at a flow rate of 1 nL/second. All
628 stereotaxic coordinates are taken from Bregma (in mm). After surgery, animals were
629 continuously monitored until recovery. For three days after surgery, mice were provided with
630 a soft diet supplemented with Carprofen for pain management (MediGel CPF, ~5mg/kg/day).

631

632 *Virus-mediated expression of genetically encoded calcium indicator*

633 Adeno-associated virus (AAV) of serotype 9 containing the genetically encoded calcium
634 indicator (GECI) 6 fast (GCaMP6f) under a flex promoter was obtained from the University
635 of Pennsylvania Vector Core (AAV2/9.Syn.Flex.GCaMP6f.WPRE.SV40, CS0641, Penn
636 Vector Core via Addgene). Lateral septum viral injections were targeted at the following

coordinates: Anterior LS, AP: 0.86; ML: 0.35; DV: -3.0; Intermediate LS, AP: 0.38; ML: 0.35; DV: -2.7, Posterior LS, AP: 0.10; ML: 0.35; DV: -2.5, with DV + or - .2 to adjust for more dorsal or ventral placement of injection. Lateral septum injections were done in VGAT-IRES-Cre transgenic mice (Slc32a1$^{tm2(cre)Lowl}$/J, JAX stock #016962). For hippocampal principal cell imaging, C57Bl/6J mice (JAX stock #000664) were injected with a viral vector specifically targeting GCaMP6f expression to CaMKII-positive cells (AAV5.CamKII.GCaMP6f.WPRE.SV40, Penn Vector Core via Addgene, CS1024). GCaMP6f injections were targeted at the following coordinates: CA1, AP: -1.8; ML: 1.5; DV: -1.5; CA3, AP: -2.1; ML: 2.3; DV: -2.2. Three of CA3 animals were Grik4-Cre transgenic mice (C57BL/6-Tg(Grik4-cre)G32-4Stl/J, JAX stock #006474), restricting GCaMP6f expression to the pyramidal cells of CA3 specifically.

Retrograde tracing

Retrograde tracing studies were done using a Cre-dependent retrograde Rabies tracing approach. Briefly, 100 nL of helper virus (AAVdj.hSyn.Flex.TVA.P2A.eGFP.2A.oG, NeuroPhotonics Center, Laval, Canada; [114,115]) was injected in the LSd (coordinates as above) of VGAT-IRES-Cre transgenic mice (n = 5 animals, Slc32a1$^{tm2(cre)Lowl}$/J, JAX stock #016962). Cre specificity was tested by the NeuroPhotonics center. After 4 weeks of incubation time to allow for the complete expression of the helper virus, 200 nL of inactivated EnvA pseudotyped rabies virus coupled to mCherry was injected (RABV-EnvA-deltaG-mCherry, NeuroPhotonics Center) at the same coordinates as the helper virus injection, and brains were collected 7 days later.

Anterograde transsynaptic tracing

To distinguish synaptic targets from passing projection fibers of dCA1 and dCA3 within the LS, C57Bl/6J mice (JAX stock #000664) received a bilateral injection of transsynaptic Cre-inducing anterograde virus (AAV1-hSyn-Cre-WPRE-hGH, Penn Vector Core via Addgene, V24784) mixed with a Cre-dependent tdTom-expressing reporter virus to visualize injection sites (AAV2-Ef1a-flex-tdTomato, NeuroPhotonics Center, AAV602) in a 3:1 ratio, 80 nL total injection volume per hemisphere (n = 5 mice per group). Injections were targeted at the following coordinates: CA1: AP: -1.86; ML: 1.5; DV: -1.5; CA3: AP: -2.1; ML: 2.3; DV: -2.2. Following 1 week of incubation time, animals received a bilateral injection of a Cre-dependent anterograde vector in LS expressing enhanced yellow fluorescent protein (400 nL, bilateral, AP: 0.5; ML: 0.35; DV: -2.6, AAVdj-DIO-Cheta-eYFP, NeuroPhotonics Center, AAV938). Brains were collected and processed three weeks post-injection.

Synaptag tracing

To verify presence of synaptic connections at the level of the LS-MS projection, AAVdj-hSyn-flex-mRuby2-syp-eGFP construct (lot AAV799, NeuroPhotonics Center; Oh et al., 2014) was injected in the LS of CaMKIIα-Cre mice (B6.Cg-Tg(Camk2a-cre)T29-1Stl/J, JAX stock #005359), with 100 nL total injection volume injected at 1 nL/second (unilateral, AP: 0.5; ML: 0.35; DV: -2.7). After 4 weeks of incubation time, animals were perfused, and brains were processed as described below.

GRIN lens implant and baseplate

Two to four weeks post GCaMP6f injection, a 0.5 mm diameter gradient refractive index (GRIN, Inscopix) lens was implanted above LS, dorsal CA1 or CA3, or a 1.8 mm GRIN (Edmund Optics) lens was implanted above dorsal CA1. For .5 mm LS lens implant, the lens was glued to an aluminium baseplate prior to the surgery, which provided two main

686 advantages: 1) it allowed us to implant the baseplate/lens assembly in one surgery (instead of
687 separate surgeries) and 2) during the surgery the miniscope (V3, miniscope.org) was used to
688 image for fluorescence while lowering the lens. The mouse was anesthetized with isoflurane,
689 and the skull was cleared. A ~.6 mm diameter hole was drilled in the skull at the level of the
690 injection site. An anchor screw was placed above the contralateral cerebellum to stabilize the
691 implant. The baseplate and GRIN combination were attached to the miniscope and together
692 secured to the stereotaxic frame. After making a leading track using a .5 mm diameter needle,
693 the implant was lowered in place. While lowering the GRIN lens into the tissue, an increase
694 in fluorescent signal indicates that the injection site has been reached. Both the GRIN lens
695 and baseplate were permanently secured using C&B-Metabond (Patterson Dental). A plastic
696 cap was used to protect the GRIN lens from scratching during the recovery period and in
697 between recording sessions. The animal was given 4 - 6 weeks of recovery time before
698 experiments started. LS implants were targeted at the following coordinates: Anterior LS,
699 AP: 0.86; ML: 0.35; DV: -2.9; Intermediate LS, AP: 0.38; ML: 0.35; DV: -2.65; Posterior
700 LS, AP: 0.10; ML: 0.35; DV: -2.45; with DV + or - .2 to adjust for dorsal, ventral or
701 intermediate targets; CA3 implants were targeted at AP: -2.1; ML: 2.2; DV: -2.2.

702 For 1.8 mm GRIN lens implantation, a ~2 mm diameter cranial window was prepared.
703 Again, an anchor screw was used to secure the implant in place. After removing the dura, a
704 portion of the cortex above the injection site was gently aspirated using a vacuum pump
705 without applying pressure on the underlying hippocampal tissue. The 1.8 mm GRIN lens was
706 lowered at the following coordinates: AP: -1.8; ML: 1.5; DV: -1.8. The GRIN lens was
707 permanently attached to the skull using Metabond, and Kwik-Sil (World Precision
708 Instruments) silicone adhesive was placed on the GRIN to protect it. On average 4 weeks
709 post-implant, the silicone cap was removed and CA1 was imaged using a miniscope mounted
710 with an aluminium base plate while the mouse was under light anesthesia (~0.5 % isoflurane)

to allow the visualization of cell activity. When a satisfying field of view was found (large number of neurons, visible landmarks), the baseplate was cemented above the GRIN lens and a protective cap was used to protect the GRIN from scratches. Imaging would start approximately 1 week after baseplating.

Miniscope recordings

The animals were habituated by being gently handled for ~5 min per day for 3 days. Animals were then water or chow-scheduled (2h access per day). Miniscope recordings performed at 30 Hz for 15 minutes, with just one recording session per day to minimize photobleaching. For open field recordings, animals were freely foraging for randomly placed 10% sucrose or 10% sweetened condensed milk in water rewards.

Recording environments consisted of a 45 x 45 cm dark grey open field with visual cues, or a 49 x 49 cm white plexiglass open field, which was placed in different recording chambers. For linear track recordings, rewards (30 ul of 10% sucrose water) were placed at each end of the 100 cm linear track, or a 130 cm linear track, and the mouse had to consume one reward before getting the next one delivered. To ensure that all animals received the same amount of exposure, for analysis of spatial and self-motion modulation, only recordings were included from the first time the animal spent time in the open field.

For analysis of modulation by food zones or objects, animals were placed again in the, now familiar, open field on day 1, 3 and 5. On day 2 and 4, food zones or objects were added in opposing corners of the familiar open field without changing any of the existing visual cues. Food zones or objects were visible to the animal. Time spent in the region of interest was computed by taking all timestamps in which animals had their nose within less than 2 cm from the edge of the food zone or the object.

Non-match to place paradigm: Mice were water scheduled (2 h per day) and trained in an automatized T-maze (MazeEngineers) to a non-match to place task. Briefly, each trial was divided into two distinct phases: sample and test. In the initial sample phase, a randomly selected arm was blocked, which forced mice to explore the opposite arm where the animal received a 10% sucrose water reward. After consuming the reward, animals would return to the start box for the test phase, during which both arms could be explored. In the test phase, only the previously unexplored arm is baited, so that mice have to alternate locations between sample and test phases. Mice were subjected to 10 trials (sample + test) per day, for 10 consecutive days, and calcium activity in LS was recorded on all days. Data provided in S11 Fig are from Day 10 of training.

Miniscope and behavior video acquisition

Miniscopes (V3 and V4, miniscope.org) were assembled using open-source plans as described previously (miniscope.org) [116,117]. Imaging data were acquired using a CMOS imaging sensor (Aptina, MT9V032) and multiplexed through a lightweight coaxial cable. Data was acquired using a data acquisition (DAQ) box connected via a USB host controller (Cypress, CYUSB3013). Animal behavior was recorded using a webcam mounted above the environment. Calcium and behavioral data were recorded using Miniscope custom acquisition software. The DAQ simultaneously acquired behavioral and cellular imaging streams at 30 Hz as uncompressed .avi files (1000 frames per file), and all recorded frames were timestamped in order to perform the subsequent alignment.

Histology

After completion of all experiments, animals were deeply anesthetized with ketamine/xylazine/acepromazide (100, 16, 3 mg/kg, respectively, intraperitoneal injection).

Mice were then transcardially perfused with 4% paraformaldehyde in PBS (PFA). Brains were extracted and postfixed in PFA at 4 °C for a minimum of 48 hours. Brains were sectioned at 50 μm using a vibratome and cryoprotected in a solution of 30% ethylene glycol, 30% glycerol and 40% PBS until used.

Immunohistochemistry

Sections were washed 3 x 20 min in PGT (0.45% Gelatin and 0.25% Triton in 1x PBS) at room temperature. Next, primary antibodies (1:1000 goat anti-GFP from Novus Biologicals or 1:10 000 rabbit anti-RFP from VWR (Rockland) were incubated with PGT overnight at 4°C. Following 10, 20, and 40 min washes in PGT, sections were incubated with secondary antibodies (1:1000 donkey anti-goat coupled to A488 or 1:1000 donkey anti-rabbit coupled to A555, both from Molecular Probes) in PGT at room temperature for 1 hour. Sections were subsequently washed for 10 and 20 minutes in PGT and 30 minutes in PBS. Sections were then mounted on glass slides and permanently coverslipped with Fluoromount that contained DAPI.

***In-vitro* patch clamp electrophysiology**

Mice were deeply anesthetized and acute brain slices were obtained following the protective recovery method [118]. Briefly, mice were transcardially perfused with N-methyl-D-glutamine (NMDG-based) solution containing (in mM): 93 NMDG, 93 HCl, 2.5 KCl, 1.2 NaH2PO4, 30 NaHCO3, 20 HEPES, 25 glucose, 5 sodium ascorbate, 2 thiourea, 3 sodium pyruvate, 10 $MgSO_4$ and 0.5 $CaCl_2$, (pH 7.4, oxygenated with carbogen). The brain was then quickly extracted and coronal slices (300 μm) were cut using a vibrating microtome (Leica-VT1000S). Slices were incubated for 10–12 min in 32°C NMDG solution before being transferred to a holding chamber filled with artificial cerebrospinal fluid (aCSF), kept at room

785 temperature and containing (in mM): 124 NaCl, 24 $NaHCO_3$, 2.5 KCl, 1.2 NaH_2PO_4, 5
786 HEPES, 12.5 glucose, 2 $MgSO_4$, and 2 $CaCl_2$, (pH 7.4, oxygenated with carbogen). For
787 electrophysiology, slices were transferred to a submerged recording chamber perfused with
788 aCSF (3 ml /min flow rate, 30 °C). Patch-clamp recordings were obtained from LS
789 GABAergic (VGAT-positive) neurons expressing the fluorescent marker GFP and visualized
790 using a 40x water immersion objective on an upright Olympus microscope. Recordings were
791 performed and analysed using an Axon Multiclamp 700B amplifier and the Clampfit10
792 software (Molecular Devices). The intrapipette solution contained (in mM) 126 K-gluconate,
793 4 KCl, 10 HEPES, 4 Mg2ATP, 0.3 Na_2GTP, and 10 PO-Creatine, adjusted to pH 7.25 with
794 KOH (272 mosm). Pipette resistance was 4-6MΩ.
795
796 **Calcium imaging analysis**
797 Calcium imaging videos were analyzed using the Miniscope Analysis pipeline
798 (https://github.com/etterguillaume/MiniscopeAnalysis) as described previously [47]. Non-
799 rigid motion correction was applied using NoRMCorre [119], and videos were spatially
800 downsampled (3x) before concatenation. Calcium traces were extracted using CNMFe [120]
801 using the following parameters: gSig = 3 pixels (width of gaussian kernel), gSiz = 20 pixels
802 (approximate neuron diameter), background_model = 'ring', spatial_algorithm = 'hals',
803 min_corr = 0.8 (minimum pixel correlation threshold), min_PNR = 8 (minimum peak-to-
804 noise ratio threshold). After extraction, cells and traces were visually inspected, and cells
805 with low signal to noise ratio were removed. Raw calcium traces were filtered to remove
806 high-frequency fluctuations and binarized (normalized amplitude > 2 sd and the first-order
807 derivative > 0) [47].
808 Mouse position and head orientation was tracked using a DeepLabCut [121,122]
809 model trained on several mouse pose markers including head centroid (for position) and nose

tip (used to compute head direction angle, see below). Velocity was extracted by dividing $\Delta d/\Delta t$ where *d* is the distance and *t* is time, and subsequently smoothed using a gaussian filter with sigma = 33 ms to remove movement artefacts. Acceleration was computed by differentiating (Matlab function *diff*) velocity. Head direction was computed as the angle between the vertical axis and the line formed by the head centroid and nose tip. Location data was interpolated to calcium imaging sampling frequency using linear interpolation. Head directions were interpolated using the same method, but direction data was first unwrapped, interpolated and converted back into radians.

Activity and bursting index

Following the binarization of raw calcium traces, we compute the probability of a neuron to be active P(A) using the following formula:

$$P(A) = \frac{time\ active}{total\ time}$$

The bursting index was computed as the probability of a cell being active, given it was already in an active state, or P(Active, t | Active, t-1). The activity index is computed as the probability of a cell becoming active when it is in an inactive state, or P(Active, t | Inactive, t-1).

Spatial modulation

Before processing, input variables were binned (Position in open field: 17 x 17 bins of 3 x 3 cm; Position in linear track: 34 bins of 3 cm; velocity, min = 2.5 cm/s, max = 30 cm/s, 20 bins; acceleration: min = -2 cm/s^2, max = +2 cm/s^2 , 20 bins; head direction: 40 bins of 9°). Velocity was smoothed over thirty frames to reduce discontinuities. For head direction and positional information, all frames were velocity was < 5cm/s were excluded. The probability of being active P(A) informs on the activity rate of a neuron. Next, we compute the

probability of spending time in a given bin i (spatial, velocity, acceleration or head direction bin).

$$P(S_i) = \frac{time\ in\ bin\ i}{total\ time}$$

Next, we compute the joint probability:

$$P(S_i \cap A) = \frac{time\ active\ while\ in\ bin\ i}{total\ time}$$

And the probability that a cell is active given the animal is in a bin:

$$P(A \mid S_i) = \frac{time\ active\ while\ in\ bin\ i}{time\ in\ state}$$

After plotting the binarized activity in space, we perform n = 1000 random circular permutations. Circular permutations are used to remove the temporal relationship between neuronal activity and behavior, but it preserves the temporal structure of calcium transients and therefore leads to more conservative results (as opposed to complete randomization of every data point, which inflates the significance value of results). Because shuffled surrogates were not systematically normally distributed, we used a non-parametric approach where the *p*-value corresponds to the number of datapoints from the shuffled distribution that are greater than the actual data for each bin, divided by the number of permutations [123]. A threshold of $p < .01$ is used to determine the significant data points that make up a significant place field. In our case, for a cell to be considered spatially modulated, at least one of the spatial bins must contain activity that is significantly non-random. To compute within-session stability, the halfway point in the recording was determined by taking the timestamps where half of the total number of binarized events for the session was reached. Tuning maps were computed for both the first and second half of the session using the methodology described above. A Gaussian smoothing filter ($\sigma = 3$) was used to smooth the tuning maps before computing a correlation between the two. A within-session correlation value of >.5 was considered a stable field.

855

856 **Calculating mutual information content**

857 Mutual information is used to describe the amount of information about one variable (spatial
858 location, head direction, velocity or acceleration) through the observation of neuronal
859 activity, and was calculated using the following formula:

860 $$MI = \sum_{i=1}^{M} \sum_{j=1}^{2} P(S_i \cap A_j) \times log2(\frac{P(S_i \cap A_j)}{P(S_i) \times P(A_j)})$$

861 Where *M* is the total number of possible behavioral states, $P(S_i \cap A_j)$ is the joint probability of
862 the animal being in bin *i* concurrently with activity level *j*. As we are using binarized activity,
863 *j* can only be active or inactive. MI was calculated using 30 bootstrapped surrogates using 50
864 percent of the data (randomly chosen data points) with replacement, to allow for computation
865 of mean MI and SEM. Next, the trace was circularly shuffled in order to calculate a shuffled
866 MI and SEM. Cells were then sorted along with the magnitude of the difference between
867 mean MI and mean shuffled MI, and a two-way ANOVA with a $p < .01$ threshold was used
868 to determine whether the difference between the two numbers was significant in order for the
869 cell to be deemed significantly spatially modulated. In case the assumptions for parametric
870 ANOVA are not met (normal distribution, variance homogeneity), the significance value was
871 computed by taking the sum of the shuffled MI values of greater magnitude than actual MI
872 values, divided by the number of shuffles.

873

874 **Bayesian decoding**

875 A Bayesian decoder was used to evaluate how well LS neural activity estimated the animal's
876 location as compared to neural activity recorded from dorsal CA1 and CA3. We used
877 decoding methods specifically adapted for calcium imaging data with binarized calcium
878 transients [47]. Using only epochs with velocity > 5 cm/s, a training dataset was generated

879 using 50% of the data. The remaining 50% of the data was used for testing. Decoding
880 efficiency (as measured by a decoding error and a decoding agreement score as outlined
881 below) was calculated using 30 bootstrapped surrogates using randomly chosen data points
882 with replacement, to allow for computation of mean MI and SEM. In order to allow for fair
883 comparison between recordings with different numbers of cells recorded, this approach was
884 done using either 40, 60, 80 or 100 randomly chosen cells with replacement for each
885 bootstrapped sample. The posterior probability density function, which is the probability that
886 an animal is in a particular bin S_i , given the neural activity A is calculated using the
887 following equation:

$$P(S_i \mid A) = \frac{P(A \mid S_i) \times P(S_i)}{P(A)}$$

888 P(S|A) is the posterior probability distribution of states given neuronal activity. No prior
889 assumption is made about the location of the mouse on the linear track, P(S) is kept uniform
890 to attribute equal probability for each location. Every neuron is assumed to be independent of
891 each other. To construct the tuning curves from multiple neurons, we use the following
892 equation:

$$P(S \mid A) = \prod_{k=1}^{N} \frac{P(A_k \mid S) \times P(S)}{P(A_k)}$$

893 With *P(S|A)* a vector of *a posteriori* behavioral states and *N* corresponding to the number of
894 neurons used. For every neuron *k* the tuning curves are constructed, and corresponding
895 posterior location probability can be derived.

896 To reconstruct the position of the mouse, we will consider the location associated with
897 the maximum a posteriori:

$$\hat{y} = arg\,max\,exp\left[\sum_{k=1}^{N} log\left(1 + \frac{P(A_k \mid S) \times P(S)}{P(A_k)}\right) - 1\right]$$

With the estimated state among all possible states S. We used a temporal filtering window in the open field of 1.5 seconds and in the linear track of 0.5 seconds to remove erratic jumps in the decoded position of the mouse. Decoding accuracy was measured as 1) decoding error and 2) decoding agreement. In one-dimensional space, decoding error was assessed as

$$decoding\ error\ =\ |\ decoded\ position\ -\ actual\ position\ |$$

In two-dimensional space, decoding error was assessed as

$$decoding\ error\ =\ (\sqrt{actual\ position\ -\ decoded\ position})^2$$

Decoding score was computed as

$$decoding\ score\ =\ \frac{mean\ (shuffled\ decoding\ error)\ -\ mean\ (decoding\ error)}{length\ of\ track}$$

Decoding agreement was defined as the portion of time where the exact location or head direction bin was successfully decoded:

$$decoding\ agreement\ =\ \frac{time\ points\ successfully\ decoded}{total\ time}$$

Tracking cells across sessions

Neurons were tracked over multiple days using a probabilistic method as previously described [124]. Briefly, spatial footprints were aligned using non-rigid alignment (transformation smoothness = 2) to correct for brain tissue displacements or miniscope placement. After alignment, we considered candidate sets of cells to be the same neuron if their maximal distance was < 12 um, and the spatial correlation between sets of cells was > .65. Next, we visually identified candidate cell pairs across sessions and manually deleted those cell pairs that were erroneously selected (< 1% of cases). We assessed the stability of the spatial representation in LS using simple field correlation, which was assessed by correlating smoothed place fields of cell pairs. To generate the null hypothesis for place

fields' displacements between pairs of days, we used the place fields tuning maps but shuffled cell identities over days (30 shuffles).

Materials availability

This study did not generate new unique reagents.

Data and Code availability

All data used for main and supplemental figures are publicly available at [insert DOI from Gnode]. Code for cell extraction is available at https://github.com/etterguillaume/MiniscopeAnalysis. Code for behavior extraction is available at https://github.com/etterguillaume/PIMPN. Code for extraction of tuning curves and decoding were adapted from [47] and can be downloaded at the following address: https://github.com/etterguillaume/CaImDecoding. All other code is available at https://github.com/suzannevdveldt/spatialcodingLS.

Statistics

Statistics Statistical analyses were performed using Matlab (Mathworks) and GraphPad Prism version 6.00 (GraphPad Software, La Jolla, California USA). All data are presented as mean ± standard error of the mean (SEM) and statistical test details are described in the corresponding results. All t-tests are two-tailed. Normality distribution of each group was assessed using the Shapiro-Wilk normality test and parametric tests were used only when distributions were found normal, using Student's t-tests, one-way ANOVA or two-way ANOVA. For non-normal distributions, non-parametric tests Mann-Whitney or Kruskal-Wallis tests were performed and described where applicable. Significant main effects or interactions were followed up with appropriate post hoc testing using Bonferroni corrections

were applicable. $p < 0.05$ was considered statistically significant, or $p < .01$ and described where applicable *, $p < 0.05$; **, $p < 0.01$; ***, $p < 0.001$, ****, $p < 0.0001$.

Funding

This work was supported by funding from the Canadian Institutes for Health Research (CIHR), Fonds de la Recherche en Santé du Québec (FRSQ), and the Natural Sciences and Engineering Research Council of Canada (NSERC). SVDV is supported by a Vanier Canada Graduate Scholarship and the Richard H. Tomlinson Doctoral Fellowship. C-AM is supported by a FRQS fellowship.

Acknowledgments

We thank Fernanda Sosa for help with behavioral recording experiments, training of the animals, immunohistological experiments and quantifications. Alexandra T. Keinath for valuable comments on a previous version of the manuscript, and Ke Cui for help with colony maintenance and mice perfusions. We also thank Daniel Aharoni (UCLA) for guidance in using the UCLA miniscope and Bruno Rivard for help building the miniscopes. The present study used the services of the Molecular and Cellular Microscopy Platform at the DHRC.

Competing interests

The authors declare no competing interests.

Supplemental figures

S1 Fig: LS receives direct inputs from the pyramidal cells of the hippocampus.

(A) Strategy for retrograde rabies tracing in LS. (B) Mean proportion of cells found in the hippocampus for each 300µm coronal section; two-way RM ANOVA, $F(24, 126) = 2.738$, p

968 = .002, interaction effect, n = 5 mice. (C) Coronal section of ventral hippocampal region,
969 showing retrogradely labelled cell bodies in subiculum, CA1 and CA3. (D) Retrogradely
970 labelled cell bodies in the *fasciola cinereum* (FC). (E) Retrogradely labelled cells in the
971 ventral tegmental area (VTA). (F) Bilateral labelling of the hypothalamic region. (G) Cell
972 bodies in the periaqueductal grey. (H) Total number of starter cells for each LS subregion,
973 ANOVA, $F(2,12) = 24.61$, $p > .0001$. Scale bars: C, left: 500 μm, right: 300 μm. D,200 μm.
974 E, 500 μm, F, 500 μm and G, 400 μm. *, $p < .05$, **, $p < .01$, ***, $p < .001$, ns = not
975 significant. Test used in B, one-way ANOVA. Sub = subiculum, FC = fasciola cinereum, Aq
976 = aqueduct, mtg = mammillotegmental tract, VTA = ventral tegmental area, MM = medial
977 mammillary nucleus, PH = posterior hypothalamic area, 3V = third ventricle, LH = lateral
978 hypothalamus, f = fornix, PAG = periaqueductal grey.
979
980 **S2 Fig: Histological verification of CA1 implant location.**
981 (A) Examples for CA1 animals included in 1D spatial navigation task, with Cre-dependent
982 GCaMP6f (green) in a CaMKIIα-Cre mouse with DAPI counterstaining (blue). (B)
983 Corresponding spatial footprints (SFPs) from extracted cells, color coded for minimum to
984 maximum mutual information value. (C) Example of approach to compute the correlation
985 between mutual information and position on the X-axis, linear regression $R^2 = 0.005682$, $p =$
986 2678. (D) Summary of all R^2 values for n = 5 mice.
987
988 **S3 Fig: Histological verification of CA3 implant location.**
989 (A) Coronal section of dorsal hippocampal region, showing location of GRIN lens implant.
990 Left: Animals implanted trans-hippocampally. Right: Animals implanted with an
991 extrahippocampal approach. (B) Coronal sections from anterior to progressively more
992 posterior regions of the hippocampus, showing extent of damage for a 500 um lens implant.

(C) Comparison between mutual information and probability being active for spatially modulated cells recorded in animals with trans-hippocampal versus extra-hippocampal implants (MI: unpaired t-test, t(64) = 0.0367, p = 0.9708; P(A): unpaired t-test, t(51) = .3908, p = 6875; extra-hipp: n = 22 cells from 2 animals, trans-hipp: n = 44 cells from 3 animals).

S4 Fig: GABAergic cells in the lateral septum are significantly spatially modulated in a 1D environment.

(A) Example of raw calcium fluorescence trace (top), and binarized events (green, bottom). Trace is divided into early and late recording epochs using 50% of total calcium (using the area under the curve). Inset: zoomed calcium trace with binarized traces. (B) Linear correlation between MI and probability being active (linear regression, R^2 = 0.5006, p < .0001, n = 1030 cells from n = 15 mice). (C) Method for computing the MI and 95% confidence interval from bootstrapped samples (left) and 30x shuffled surrogates (right). (D) MI computed from actual traces (black) and shuffled traces (red), sorted by the magnitude of the difference between these values, two-way ANOVA, F(1029,59740) = 126.3, p < .0001 for interaction effect. Left inset: zoomed version first 20 cells. Right inset: zoomed version for 20 not significant cells. (E) Scatterplot for significance level for spatial modulation and probability being active (linear regression, R^2 = .0145, p = 0.007, n = 1030 cells, n = 15 mice). (F) Group averages of actual (grey) versus shuffled (red) MI for spatially modulated LS cells recorded on linear track (Mann-Whitney test, U = 116394, p < .0001). (G) LS group averages of spatial cells (grey) versus non-spatial cells (red) for split half stability (Mann-Whitney test, U = 17743, p < .0011). (H) Examples of significantly spatially modulated cells representative for each rank, as ranked according to panel C. *, p < .05, ****, p < .0001.

S5 Fig: Intrinsic properties and firing frequency in GABAergic neurons of the lateral septum and parvalbumin-positive (PV) fast-spiking interneurons of the hippocampus.

(A) VGAT-cre mice were injected with AAVdj-Flex-GFP in LS and patch-clamp whole cell recordings were performed from fluorescent neurons of the dorsal LS. (B) Representative photos showing the localization of Cre-dependent fluorescence and VGAT-positive neurons two weeks after bilateral micro-injections at LS coordinates. Scale bar: 200, 200, 10 µm, (asterisk marks the location of a patched cell). (C) Current-clamp traces from an GFP positive LS neuron (shown in b) characterized using depolarizing current injection steps (0-200pA). (D) Sample traces showing hyperpolarizing and depolarizing responses from a fast-spiking (PV) hippocampal interneuron. (E) Plot of mean firing frequencies in response to injected currents of increasing supra-threshold amplitudes in hippocampal PV interneurons (open circles) and LS VGAT neurons (solid squares). Current injections were 600 ms square pulses. Firing-frequencies are plotted from threshold current (t) to t + 220 pA (two-way ANOVA with Bonferroni's multiple comparison test, $F(11, 154) = 21.74$, $p < .0001$ for interaction effect). *, $p < .05$, ***, $p < .001$, ****, $p < .0001$.

S6 Fig: High proportion of spatially modulated cells in LS is not caused by differences in probability being active.

(A) Probability being active for all cells recorded for each group (Kruskal-Wallis, $H(3) = 502.0$, $p < .0001$; LS: n = 1030 cells, n = 15 mice. CA1: n = 1251 cells, n = 5 mice, CA3: n = 464 cells, n = 6 mice). (B) Histogram of probabilities being active for all groups (C) Histogram of MI values for all cells recorded in LS, CA1 and CA3. (D) Using a cut-off of P(A) > .001 to exclude cells of low activity levels, comparison of proportion of spatially modulated cells for each region (left, Kruskal-Wallis, $H(3) = 59.57$, $p = .0509$, LS: n = 15 mice. CA1: n = 5 mice, CA3: n = 6 mice) and average split half stability for spatially

modulated cells (right, Kruskal-Wallis, H(3) = 80.48, $p < 0.0001$, LS: n = 475 cells, n = 15 mice, CA1: n = 363 cells, n = 5 mice, CA3: n = 142 cells, n = 5 mice) . ****, p < .0001.

S7 Fig: Lateral septum spatially modulated cells are significantly directionally modulated.

(A) Mouse location on day 5 of linear track training, divided in left runs (orange) and right runs (light blue) with corresponding raw calcium activity (middle, dark blue) and derived binary trace (bottom, yellow). (B) Probability of cell being active for left (orange) versus right trajectories (blue), and corresponding mutual information calculated separately for left and right runs. (C) Corresponding locations where binarized activity was detected (orange for left trajectories, blue for right trajectories and black for all trajectories). (D) MI values for right versus left trajectories ranked by magnitude of the difference between the two. Dotted line p < .01 significance level used to assess spatial modulation of cells, two-way ANOVA, F(489,28420) = 496.9, $p < .0001$ for interaction effect. (E) Proportion of spatially modulated cells in LS that are right-selective (blue, 22.08%), left-selective (orange, 15.52%), spatially modulated but not directionally modulated (red, 7.67%) and non-spatially modulated (grey, 54,71%, left), CA1 (middle) and CA3 (right).

S8 Fig: Decoding using fewer cells still leads to significant differences between septohippocampal regions and shuffled surrogates in linear track .

(A) Mean decoding error for location decoding on the linear track using LS cells computed for 30 bootstrap samples of 40, 60, 80, or 100 cells (black, each dot represents mean of an animal) compared to a decoded location using shuffled tuning maps (red, each dot represents mean of an animal), two-way RM ANOVA, F(3,19) = 571.4, $p = 0.0024$ for main effect of shuffling, F(3,19) = 6.948, $p = 0.0024$ for main effect of number of included cells. (B) Left:

same as A, for mean decoding agreement, two-way RM ANOVA, $F(3,19) = 1059$, $p < .0001$ for main effect of shuffling, $F(3,19) = 10.06$, $p = 0.0003$ for main effect of number of included cells, Right: Method for computing the mean decoding agreement for each bootstrapped estimate. (C) Same as A, for cells recorded from dorsal CA1. In addition to 30 bootstrapped samples of 40, 60, 80 and 100 cells, this panel includes mean decoding error using all recorded cells, two-way RM ANOVA, $F(1,20) = 304.3$, $p < .0001$ for main effect of shuffling, $F(4,20) = 2.647$, $p = 0.0637$ for main effect of number of included cells. (D) Same as A, for cells recorded from dorsal CA3, two-way RM ANOVA, $F(1,9) = 42.83$, $p = .0001$ for main effect of shuffling, $F(3,9) = 1.480$, $p = 0.2845$ for main effect of number of included cells. (E) Using only cells with P(A) > .001, decoding error for actual versus shuffled dataset using 60 cells (paired t-tests, LS: $t(5) = .10$, $p = 0.001$, n = 6 mice; CA1: $t(4) = 6.732$, $p = .0025$, n = 5 mice; CA3: $t(3) = 2.966$, $p = .0592$, n = 4 mice). (F) Using only cells with P(A) > .001, mean decoding score for each region (one-way ANOVA, $F(2,12) = 5.765$, $p = 0.0167$. (G) Same as E, without using a temporal smoothing window (paired t-tests, LS: $t(6) = 10.08$, $p < 0.0001$, n = 7 mice; CA1: $t(4) = 7.897$, $p = .0014$, n = 5 mice; CA3: $t(3) = 2.614$, $p = .0794$, n = 4 mice). (H) Same as F, without using a temporal smoothing window (ANOVA, $F(2,13) = 5.462$, $p = .0190$). *, $p < .05$, **, $p < .01$, ***, $p < .001$, ****, $p < .0001$.

S9 Fig: GABAergic cells in the lateral septum are significantly spatially modulated during free exploration in a 2D environment.

(A) Probability P(active | location) of an example cell to be active in a bin (3 cm) of the open field (45 or 49 cm size). (B) Significance computed from n = 1000 circular permutations, $p <$ .01 is considered significant. (C) Within session stability is computed by correlation of the first half (left) and the second half (right) of the recording. (D) MI computed from actual traces (red) and shuffled traces (black), sorted by the magnitude of the difference between

these values (one-way ANOVA, $F(1898, 110142) = 65.50$, $p < .0001$ for interaction effect). Left inset: zoomed version of first 20 cells. Right inset: zoomed version for 20 not significant cells. (E) Cells are ranked according to the difference between their bootstrapped mean mutual information (MI) value and 30 circularly shuffled surrogates. Ranks are color-coded for clarity, n = 1899 cells from N = 28 mice. (F) Examples of significantly spatially modulated cells with corresponding mean MI value (top) and split within-session stability (bottom) representative for each rank. (G) Computation of activity index (probability inactive to active) and bursting index (probability active to active) . (H) Left: Activity index for spatial vs. non-spatial cells (Mann-Whitney test, $U = 342219$, $p < .0001$). Right: Bursting index for spatial versus non-spatial cells (Mann-Whitney test, $U = 368276$, $p < .0001$).

S10 Fig: LS spatially modulated cells do not anchor to foodzones or objects.

(A) Experimental set-up, with animals freely exploring the same open field for 5 consecutive days, with two food zones and two objects added in opposing corners on day 2 and 4 respectively. Representative trajectories are shown in grey. Green circles and stars represent locations of food and objects. (B) Representative example of the average number of cells active per 3 cm bin for an example mouse (baseline 1: n = 132 cells; food zones: n = 110 cells; baseline 2: n = 118 cells; objects: n = 118 cells; baseline 3: n = 72 cells). (C) For the same animal, red dots are centroids of spatially modulated cells. (D) Centroids for each significantly spatially modulated cell of all animals included in analysis (baseline 1: n = 730 cells, n = 10 mice; food zones: n = 559 cells, n = 10 mice; baseline 2: n = 749 cells; n = 10 mice; objects: n = 407 cells, n = 8 mice; baseline 3: n = 471 cells; n = 8 mice). (E) Time spent in food zone as a percentage of total time spent in session for all animals (n = 10 mice). (F) Number of visits to food zone (n = 10 mice). (G) Likelihood of cell being active within the food zone as compared to a shuffle for all cells recorded (Wilcoxon matched-pairs signed

rank test, W = -3490, p = .6497, n = 559 cells, n = 10 mice). (H) Time spent in object zone as a percentage of total time spent in session for all animals (n = 8 mice). (I) Number of visits to objects (n = 8 mice). (J) Likelihood of a cell being active closely around the objects as compared to a shuffle (Wilcoxon matched-pairs signed rank test, W = 3789, p = .4251, n = 407 cells, n = 8 mice).

S11 Fig: Significantly spatially modulated cells are not centered around the reward zone in a non-match to place task

(A) Schematic of T-maze non-match to place task, consisting of a first forced run, followed by a free run in which the previously non-visited arm is rewarded. (B) Example trajectory of well-trained animal, with Probability (active | location) of three example cells using 5 cm bins. (C) For two example animals, red dots are centroids of spatially modulated cells. (D) Time spent in food zone as a percentage of total time spent in session for all animals (n = 6 mice). (E) Number of visits to reward zone (n = 6 mice). (F) Likelihood of a cell being active within the reward zone as compared to a shuffle for all cells recorded (Wilcoxon matched-pairs signed rank test, W = -4783, p = 0.2358; n = 365 cells from n = 6 mice, day 10 of training).

S12 Fig: Differences in spatial coding not due to inclusion of pseudo-silent cells

(A) Probability of being active for spatially modulated cells (Kruskal-Wallis, H(3) = 295.0, p < .0001; Dunn's multiple comparisons test; LS: n = 718 spatial cells from n = 28 mice; dCA1: n = 323 spatial cells, n = 6 mice; dCA3: n = 138 spatial cells, n = 7 mice). (B) Left: Using an activity cut-off of P(A) > .001, proportion of spatial cells per animal (one way ANOVA, F(2,39) = 0.9849, p = 0.3826; Tukey's multiple comparisons test; LS: n = 1889 cells from n = 28 mice; dCA1: n = 1017 cells, n = 6 mice; dCA3: n = 521 cells, n = 8 mice).

Middle: Within session stability for spatial cells (Kruskal-Wallis, H(3) = 89.52, $p < .0001$; Dunn's multiple comparisons test; LS: n = 718 spatial cells from n = 28 mice; dCA1: n = 323 spatial cells, n = 6 mice; dCA3: n = 138 spatial cells, n = 7 mice). Right: Mean dispersion for spatial cells (Kruskal-Wallis, H(3) = 155.5, $p < .0001$; Dunn's multiple comparisons test; LS: n = 718 spatial cells from n = 28 mice; dCA1: n = 323 spatial cells, n = 6 mice; dCA3: n = 138 spatial cells, n = 7 mice). *, $p < .05$, **, $p < .01$, ***, $p < .001$, ****, $p < .0001$.

S13 Fig: Decoding using fewer cells still leads to significant differences between septohippocampal regions and shuffled surrogates in 2D environment.

(A) Mean decoding error for location decoding in the open field using LS cells computed for 30 bootstrapped samples of 40, 60, 80, and 100 cells (black, each dot represents mean of an animal) compared to a decoded location using shuffled tuning maps (red, each dot represents mean of an animal; two-way RM ANOVA, F(1,33) = 174.9, $p < 0.0001$ for main effect of shuffling, F(3,33) = 0.2041, $p = 0.893$ for main effect of number of included cells. (B) Left: same as A, for mean decoding agreement (two-way RM ANOVA, F(1,33) = 132.8, $p < .0001$ for main effect of shuffling, F(3,33) = 1.132, $p = .3505$ for main effect of number of included cells). Right: Method for computing the mean decoding agreement for each bootstrap estimate. (C) Same as A, for cells recorded from dorsal CA1. In addition to 30 bootstrap samples of 40, 60, 80 and 100 cells, panel includes mean decoding error using all recorded cells (two-way RM ANOVA, F(1,17) = 649.0, $p < .0001$ for main effect of shuffling, F(4,17) = .7948, $p = .5447$ for main effect of number of included cells) (D) Same as A, for cells recorded from dorsal CA3 (two-way RM ANOVA, F(1,11) = 44.13, $p < .0001$ for main effect of shuffling, F(3,11) = 17.99, $p = .9078$ for main effect of number of included cells). (E) Effect of temporal filtering on decoding error in the open field for LS (two-way RM ANOVA, F(1,25) = 123.7, $p < .0001$ for main effect of shuffling, F(4,25) = 0.1169, $p = .9753$

for main effect of number of included cells. (F) Comparison of mean decoding error using P(A) > .001 activity cut-off for cell selection versus without such cut off using 80 cells (LS: n = 8 mice, CA1: n = 4 mice, CA3: n = 4 mice; two-way RM ANOVA, $F(1,12) = 1.374$, $p = 2.639$ for main effect of activity cut-off, $F(2,12) = 1.023$, $p = .3889$, for main effect of structure). *, $p < .05$, **, $p < .01$, ***, $p < .001$, ****, $p < .0001$, Test used in A-F, two-way RM ANOVA.

S14 Fig: LS place code over days

(A) Within session stability for each spatially modulated cell recorded cells in LS (Kruskal-Wallis, $H(4)= 8.921$, $p = 0.0304$; Dunn's multiple comparisons test; day 1, n = 181; day 2, n = 172; day 3, n = 178; day 8, n = 209, n = 5 mice). (B) Average MI for each day for all recorded cells (Kruskal-Wallis, $H(4)= 13.27$, $p = 0.0041$; Dunn's multiple comparisons test; day 1, n = 562; day 2, n = 600; day 3, n = 477; day 8, n = 492, n = 5 mice). (C) Proportion of cells for tuning map correlation (Friedman test, $\chi 2(2) = 0.400$, $p = .9537$, significant cell pairs only, day1-2, n = 158; day 2-3, n = 122, day 3-8, n = 129). (D) Proportion of stable cells (tuning map correlation > .3) for each progressive day correlation (one-way ANOVA, $F(3,16) = 1.457$, $p = 0.2637$; significant cell pairs only, day 1-2, n = 158; day 2-3, n = 122, day 3-8, n = 129). (E) Proportion of spatially modulated cells per day (day 1, n = 562; day 2, n = 600; day 3, n = 477; day 8, n = 492, n = 5 mice). *, $p < .05$, **, $p < .01$

S15 Fig: Direction encoding by lateral septum cells.

(A) Examples of significantly modulated cells. The polar plot indicates the probability of the cell being active as a function of the animal's head direction. lack lines, p(active | bin); red lines indicate 95% upper and lower percentile; blue lines indicate the normalized time spent in each direction. MI calculated using 9° bins. (B) Same as A, for non-modulated cells. (C)

Trajectories (grey) with binarized activity superimposed, color-coded from beginning to end of the recording for representative cells shown in A. (D) Same as C, but for example, cells shown in B. (E) Examples of significantly directionally modulated cells with corresponding mean MI value (top) and within-session stability (bottom) representative for each rank.

S16 Fig: Stability of direction and self-motion encoding over short and longer timescales

(A) Tuning plots for a stable directionally modulated cell over days, using a similar set up as described as Fig 4. Tuning map correlation indicated at the bottom in red. (B) Significant tuning map correlation for aligned cell-pairs (black) versus shuffled pairs (red) for progressive days for LS (day 1-2, n = 161 cells; day 2-3, n = 119 cells; day 3-8, n = 110 cells; n = 5 mice) and dorsal CA1 (day 1-2, n = 149 cells; day 2-3, n = 102 cells; day 3-8, n = 90 cells; n = 3 mice). (C) Significant direction map correlations for cells found on all days for LS (n = 29 cells) and CA1 (n = 24 cells). (D) Same as B, for velocity tuning in LS (day 1-2, n = 110 cells; day 2-3, n = 73 cells; day 3-8, n = 73 cells; n = 5 mice) and dorsal CA1 (day 1-2, n = 109 cells; day 2-3, n = 72 cells; day 3-8, n = 61 cells; n = 3 mice). (E) Same as B, for acceleration tuning in LS (day 1-2, n = 73 cells; day 2-3, n = 47 cells; day 3-8, n = 43 cells; n = 5 mice) and dorsal CA1 (day 1-2, n = 45 cells; day 2-3, n = 40 cells; day 3-8, n = 35 cells; n = 3 mice) ****, $p < .0001$. Test used in B, D, E two-way ANOVA, with Sidak's multiple comparisons test

S17 Fig: Direction, speed and acceleration encoding in dorsal hippocampus.

(A) Left: Distribution of MI (left) and p-values (right) for direction for dCA1, dCA3 and LS. Right: MI (bits) per binarized event, for all cells recorded from each region (Kruskal-Wallis, H(3) = 351.2, $p < .0001$; Dunn's multiple comparisons test; LS: n = 1230 cells, n = 19

animals, CA1: n = 677 cells, n = 4 animals, CA3: n = 546 cells, n = 7 animals). (B) Same as A, for velocity (Kruskal-Wallis, H(3) = 325.3, $p < .0001$; Dunn's multiple comparisons test) (C) Same as B, for acceleration (Kruskal-Wallis, H(3) = 262.2, $p < .0001$; Dunn's multiple comparisons test). (D) Left: Proportion of cells that are significantly modulated by only one modality (grey), two modalities (yellow), three (red) or all 4 of the investigated variables (black) for dCA1 (n = 677 cells, n = 4 mice). Right: absolute proportion of cells modulated by any combination of variables. E) Same as D, for dCA3 (n = 546 cells, N = 7 mice). *, $p < .05$, ****, $p < .0001$

S18 Fig: LS GABAergic neurons project to the medial septum, hypothalamus and ventral tegmental area.

(A) Injection of anterograde, Cre-dependent eYFP (green) viral tracing in VGAT-Cre mouse LS. (B) Injection site in intermediate/dorsal LS (LSd) with some cell bodies labelled in intermediate LS (LSi; Green, eYFP; blue, DAPI counterstaining). (C) eYFP-positive fibers in the medial septum, (D) hypothalamus and (E) ventral tegmental area. (F) Coronal hippocampal section shows no anterograde labelling of the hippocampal formation, either dorsal or (G) ventral. Scale bars: B, 500 μm, C, 500 μm, D, 500 μm, E, 500 μm and F, 500 μm, G) 700 μm. DB = diagonal band, DG = dentate gyrus, LSd = dorsal lateral septum, LSi = intermediate lateral septum, LSv = ventral lateral septum, MS = medial septum, S = subiculum, 3V = third ventricle.

S19 Fig: Extent of primary injection sites in dorsal CA1 and CA3.

(A) Coronal sections showing expression of tdTom (red) in dorsal CA1 along anterior to posterior axis. (B) Same as A, for primary injections in dorsal CA3. Scale bars: 500 μm for all sections.

S20 Fig: Anterograde transsynaptic tracing shows that CA1 and CA3 project preferentially to dorsal LS.

(A) Primary AAV1 injections in CA1 and CA3, using the same injection strategy as described in Fig 6A. (B) Coronal section showing expression pattern at different anterior-posterior levels of the LS, with (red) tdTOM positive CA3 projections to LS and eYFP-positive second-order transduction in LS (left). Bottom schematic: an overview of the approximate bregma level of coronal slices shown. Bottom right: zoomed versions showing tdTom-positive hippocampal afferents, eYFP-positive LS cell bodies, and merge. (C) Total eYFP-positive cells counted at the level of LS following transsynaptic tracer injection in dCA1 versus dCA3 (dCA1-LS, N = 3 mice; dCA3-LS, N = 5 mice). (D) Total eYFP-positive cells along the dorsal-ventral and anterior-posterior axis observed in LS for dorsal CA3 injection and (E) for dorsal CA1 injection. Scale bars: B, top: 500 μm, bottom: 500 μm. C, all overview images, 500 μm, all zoomed images, 50 μm. ns = not significant.

S21 Fig: No changes in cell activity along dorsal-ventral or anterior-posterior axis of the LS.

(A) Probability of being active for each cell along the anterior-posterior axis (left), medial-lateral axis (middle), and dorsal-ventral axis (right). All cells were recorded during free exploration in the open field (linear regression, AP: $R^2 = 2.014 \times 10^4$, $p = 0.5611$; ML: $R^2 = 1.012 \times 10^4$, $p = 0.6803$; DV: $R^2 = 2.717 \times 10^4$, $p = 0.6803$; n = 1679 cells, n = 24 mice). (B) Same as A, but for activity index as described in S5 Fig (linear regression, AP: $R^2 = 2.691 \times 10^4$, $p = 0.5017$; ML: $R^2 = 3.287 \times 10^5$, $p = 0.8144$; DV: $R^2 = 3.254 \times 10^4$, $p = 0.4601$; n = 1679 cells, n = 24 mice). (C) Same as for A, but for bursting index (linear regression, AP: R^2

= 7.085 x 10^4, p = 0.2757; ML: R^2 = 7.457 x 10^5, p = 0.7237; DV: R^2 = 3.731 x 10^3, p = 0.0123; n = 1679 cells, n = 24 mice).

References

1. Zhao C, Eisinger B, Gammie S. Characterization of GABAergic neurons in the mouse lateral septum: a double fluorescence in situ hybridization and immunohistochemical study using tyramide signal amplification. PLoS One. 2013;8: 1–24. doi:10.1371/journal.pone.0073750
2. Lin W, McKinney K, Liu L, Lakhlani S, Jennes L. Distribution of vesicular glutamate transporter-2 messenger ribonucleic acid and protein in the septum-hypothalamus of the rat. Endocrinology. 2003;144: 662–670.
3. Risold PY, Swanson LW. Structural evidence for functional domains in the rat hippocampus. Science. 1996;272: 1484–1486. doi:10.1126/science.272.5267.1484
4. Tingley D, Buzsáki G. Transformation of a spatial map across the hippocampal-lateral septal circuit. Neuron. 2018;98: 1229-1242.e5. doi:10.1016/j.neuron.2018.04.028
5. Swanson LW, Cowan WM. The connections of the septal region in the rat. J Comp Neur. 1979;186: 621–656. doi:10.1038/nature19789
6. Brito GNO, Thomas GJ. T-maze alternation, response patterning, and septo-hippocampal circuitry in rats. Behav Brain Res. 1981;3: 319–340. doi:10.1016/0166-4328(81)90003-6
7. Rawlins JNP, Olton DS. The septo-hippocampal system and cognitive mapping. Behav Brain Res. 1982;5: 331–358. doi:10.1016/0166-4328(82)90039-0
8. Stanton ME, Thomas GJ, Brito GNO. Posterodorsal septal lesions impair performance on both shift and stay working memory tasks. Behav Neurosci. 1984;98: 405–415. doi:10.1037/0735-7044.98.3.405

9. Thomas GJ. Comparison of effects of small lesions in posterodorsal septum on spontaneous and rerun correction (contingently reinforced) alternation in rats. J Comp Physiol Psychol. 1979;93: 685–694. doi:10.1037/h0077608

10. Thomas GJ, Brito GN. Recovery of delayed alternation in rats after lesions in medial frontal cortex and septum. J Comp Physiol Psychol. 1980;94: 808–818. doi:10.1037/h0077834

11. Calderwood MT, Tseng A, Glenn Stanley B. Lateral septum mu opioid receptors in stimulation of feeding. Brain Res. 2020;1734: 146648. doi:10.1016/j.brainres.2020.146648

12. Carus-Cadavieco M, Gorbati M, Ye L, Bender F, van der Veldt S, Kosse C, et al. Gamma oscillations organize top-down signalling to hypothalamus and enable food seeking. Nature. 2017;542: 232–236. doi:10.1038/nature21066

13. Sweeney P, Yang Y. An inhibitory septum to lateral hypothalamus circuit that suppresses feeding. J Neurosci. 2016;36: 11185–11195. doi:10.1523/JNEUROSCI.2042-16.2016

14. Xu Y, Lu Y, Cassidy RM, Mangieri LR, Zhu C, Huang X, et al. Identification of a neurocircuit underlying regulation of feeding by stress-related emotional responses. Nat Commun. 2019;10. doi:10.1038/s41467-019-11399-z

15. Anthony TE, Dee N, Bernard A, Lerchner W, Heintz N, Anderson DJ. Control of stress-induced persistent anxiety by an extra-amygdala septohypothalamic circuit. Cell. 2014;156: 522–536. doi:10.1016/j.cell.2013.12.040

16. Besnard A, Gao Y, Kim MT, Twarkowski H, Reed AK, Langberg T, et al. Dorsolateral septum somatostatin interneurons gate mobility to calibrate context-specific behavioral responses. Nat Neurosci. 2019;22: 436–446. doi:10.1038/s41593-018-0330-y

17. Sparks P, Ledoux J. The septal complex as seen through the context of fear. In: the behavioral neuroscience of the septal region. Springer-Verlag; 2000.

18. Trent NL, Menard JL. The ventral hippocampus and the lateral septum work in tandem to regulate rats' open-arm exploration in the elevated plus-maze. Physiol Behav. 2010;101: 141–152. doi:10.1016/j.physbeh.2010.04.035

19. Bender F, Gorbati M, Cadavieco MC, Denisova N, Gao X, Holman C, et al. Theta oscillations regulate the speed of locomotion via a hippocampus to lateral septum pathway. Nat Commun. 2015;6: 8521. doi:10.1038/ncomms9521

20. Wirtshafter HS, Wilson MA. Locomotor and hippocampal processing converge in the lateral septum. Curr Biol. 2019;29: 3177-3192.e3. doi:10.1016/j.cub.2019.07.089

21. Bredewold R, Schiavo JK, van der Hart M, Verreij M, Veenema AH. Dynamic changes in extracellular release of GABA and glutamate in the lateral septum during social play behavior in juvenile rats: Implications for sex-specific regulation of social play behavior. Neuroscience. 2015;307: 117–127. doi:10.1016/j.neuroscience.2015.08.052

22. Chee S-SA, Menard JL, Dringenberg HC. The lateral septum as a regulator of hippocampal theta oscillations and defensive behavior in rats. J Neurophysiol. 2015;113: 1831–1841. doi:10.1152/jn.00806.2014

23. Clemens AM, Wang H, Brecht M. The lateral septum mediates kinship behavior in the rat. Nat Commun. 2020;11: 1–11. doi:10.1038/s41467-020-16489-x

24. Leroy F, Park J, Asok A, Brann DH, Meira T, Boyle LM, et al. A circuit from hippocampal CA2 to lateral septum disinhibits social aggression. Nature. 2018;564: 213–218.

25. Risold PY, Swanson LW. Connections of the rat lateral septal complex. Brain Res Rev. 1997;24: 115–195. doi:10.1016/S0165-0173(97)00009-X

1341 26. Swanson LW, Cowan WM. An autoradiographic study of the organization of the
1342 efferent connections of the hippocampal formation in the rat. J Comp Neur. 1977;172:
1343 49–84. doi:10.1002/cne.901720104
1344 27. Kita T, Nishijo H, Eifuku S, Terasawa K, Ono T. Place and contingency differential
1345 responses of monkey septal neurons during conditional place-object discrimination. J
1346 Neurosci. 1995;15: 1683–1703.
1347 28. Leutgeb S, Mizumori S. Context-specific spatial representations by lateral septal cells.
1348 Neuroscience. 2002;112: 655–663. doi:10.1016/S0306-4522(02)00101-X
1349 29. Nishijo H, Kita T, Tamura R, Uwano T, Terasawa K. Septal neuronal responses related
1350 to spatial representation in monkeys. Hippocampus. 1997;464: 460–464.
1351 30. Takamura Y, Tamura R, Zhou TL, Kobayashi T, Tran AH, Eifuku S, et al. Spatial
1352 firing properties of lateral septal neurons. Hippocampus. 2006;16: 635–644.
1353 doi:10.1002/hipo
1354 31. Zhou TL, Tamura R, Kuriwaki J, Ono T. Comparison of medial and lateral septal
1355 neuron activity during performance of spatial tasks in rats. 1999;234: 220–234.
1356 32. Wirtshafter HS, Wilson MA. Differences in reward biased spatial representations in
1357 the lateral septum and hippocampus. Elife. 2020;9: 1–20. doi:10.7554/eLife.55252
1358 33. Risold PY, Swanson LW. Chemoarchitecture of the rat lateral septal nucleus. Brain
1359 Res Rev. 1997;24: 91–113. doi:10.1016/S0165-0173(97)00008-8
1360 34. Gonzalez WG, Zhang H, Harutyunyan A, Lois C. Persistence of neuronal
1361 representations through time and damage in the hippocampus. Science. 2019;365:
1362 821–825. doi:10.1126/science.aav9199
1363 35. Howard MW, Kahana MJ. A distributed representation of temporal context. J Math
1364 Psychol. 2002;46: 269–299. doi:10.1006/jmps.2001.1388
1365 36. Mankin EA, Diehl GW, Sparks FT, Leutgeb S, Leutgeb JK. Hippocampal CA2

activity patterns change over time to a larger extent than between spatial contexts. Neuron. 2015;85: 190–202. doi:10.1016/j.neuron.2014.12.001

37. Rubin A, Geva N, Sheintuch L, Ziv Y. Hippocampal ensemble dynamics timestamp events in long-term memory. Elife. 2015;4: 1–16. doi:10.7554/eLife.12247

38. Ziv Y, Burns LD, Cocker ED, Hamel EO, Ghosh KK, Kitch LJ, et al. Long-term dynamics of CA1 hippocampal place codes. Nat Neurosci. 2013;16: 264–266. doi:10.1038/nn.3329

39. Luo AH, Tahsili-Fahadan P, Wise RA, Lupica CR, Aston-Jones G. Linking context with reward: a functional circuit from hippocampal CA3 to ventral tegmental area. Science. 2011;333: 353–358.

40. McGlinchey EM, Aston-Jones G. Dorsal hippocampus drives context-induced cocaine seeking via inputs to lateral septum. Neuropsychopharmacology. 2018;43: 987–1000. doi:10.1038/npp.2017.144

41. Butler CW, Wilson YM, Gunnersen JM, Murphy M. Tracking the fear memory engram: Discrete populations of neurons within amygdala, hypothalamus, and lateral septum are specifically activated by auditory fear conditioning. Learn Mem. 2015;22: 370–384. doi:10.1101/lm.037663.114

42. Garcia R, Vouimba RM, Jaffard R. Contextual conditioned fear blocks the induction but not the maintenance of lateral septal LTP in behaving mice. J Neurophysiol. 1997;78: 76–81. doi:10.1152/jn.1997.78.1.76

43. Reis DG, Scopinho AA, Guimarães FS, Corrêa F, Resstel LBM. Involvement of the lateral septal area in the expression of fear conditioning to context. Learn Mem. 2010;17: 134–138. doi:10.1101/lm.1534710

44. Vetere G, Kenney JW, Tran LM, Xia F, Steadman PE, Parkinson J, et al. Chemogenetic interrogation of a brain-wide fear memory network in mice. Neuron.

2017;94: 363-374.e4. doi:10.1016/j.neuron.2017.03.037

45. Leutgeb S, Mizumori S. Excitotoxic septal lesions result in spatial memory deficits and altered flexibility of hippocampal single-unit representations. J Neurosci. 1999;19: 6661–72. Available: http://www.ncbi.nlm.nih.gov/pubmed/10414995

46. M'Harzi M, Jarrard LE. Effects of medial and lateral septal lesions on acquisition of a place and cue radial maze task. Behav Brain Res. 1992;49: 159–165. doi:10.1016/S0166-4328(05)80160-3

47. Etter G, Manseau F, Williams S. A probabilistic framework for decoding behavior from in vivo calcium imaging data. Front Neural Circuits. 2020;14: 1–16. doi:10.3389/fncir.2020.00019

48. Shannon CE. A mathematical theory of communication. Bell Syst Tech J. 1948;27: 379–423. doi:10.1145/584091.584093

49. Skaggs WE, McNaughton BL, Gothard KM. An information-theoretic approach to deciphering the hippocampal code. Advances in Neural Information Processing Systems 5 eds Hanson, SJ, Giles, CL & Cowan, JD. 1993. pp. 1030–1037. doi:10.1109/EUMC.2007.4405137

50. Souza BC., Pavão R, Belchior H, Tort A. On information metrics for spatial coding. Neuroscience. 2018;375: 62–73. doi:10.1016/j.neuroscience.2018.01.066

51. Gallagher JP, Zheng F, Hasuo H, Shinnick-Gallagher P. Activities of neurons within the rat dorsolateral septal nucleus (DLSN). Prog Neurobiol. 1995;45: 373–395. doi:10.1016/0301-0082(95)98600-A

52. Markus EJ, Qin YL, Leonard B, Skaggs WE, McNaughton BL, Barnes CA. Interactions between location and task affect the spatial and directional firing of hippocampal neurons. J Neurosci. 1995;15: 7079–7094. doi:10.1523/JNEUROSCI.15-11-07079.1995

53. McNaughton BL, Barnes CA, O'Keefe J. The contributions of position, direction and velocity to single unit activity in the hippocampus of freely-moving rats. Exp Brain Res. 1983;52.

54. Navratilova Z, Hoang LT, Daniela Schwindel C, Tatsuno M, McNaughton BL. Experience-dependent firing rate remapping generates directional selectivity in hippocampal place cells. Front Neural Circuits. 2012;6: 1–14. doi:10.3389/fncir.2012.00006

55. Mau W, Sullivan DW, Kinsky NR, Hasselmo ME, Howard MW, Eichenbaum H. The same hippocampal CA1 population simultaneously codes temporal information over multiple timescales. Curr Biol. 2018;28: 1499-1508.e4. doi:10.1016/j.cub.2018.03.051

56. Pedemonte M, Barrenechea C, Nuñez A, Gambini JP, García-Austt E. Membrane and circuit properties of lateral septum neurons: Relationships with hippocampal rhythms. Brain Res. 1998;800: 145–153. doi:10.1016/S0006-8993(98)00517-4

57. Twery MJ, Gallagher JP. Somatostatin depresses GABA receptor-mediated inhibition in the rat dorsolateral septal nucleus. Brain Res. 1990;519: 277–286. doi:10.1016/0006-8993(90)90089-T

58. Twery MJ, Phelan KD, Gallagher JP. Spontaneous bursting and non-bursting activity in morphologically identified neurons of the rat dorsolateral septal nucleus, in vitro. Neuroscience. 1992;46: 669–679. doi:10.1016/0306-4522(92)90153-S

59. Acharya L, Aghajan ZM, Vuong C, Moore JJ, Mehta MR. Causal influence of visual cues on hippocampal directional selectivity. Cell. 2016;164: 197–207. doi:10.1016/j.cell.2015.12.015

60. Leutgeb S, Ragozzino KE, Mizumori S. Convergence of head direction and place information in the CA1 region of hippocampus. Neuroscience. 2000;100: 11–19. doi:10.1016/S0306-4522(00)00258-X

1441 61. Muller RU, Bostock E, Taube JS, Kubie J. On the directional firing properties of
1442 hippocampal place cells. J Neurosci. 1994;14: 7235–7251. doi:10.1523/jneurosci.14-
1443 12-07235.1994
1444 62. Czurko A, Hirase H, Csicsvari J, Buzsáki G. Sustained activation of hippocampal
1445 pyramidal cells by “space clamping” in a running wheel. Eur J Neurosci. 1999;11:
1446 344–352. doi:10.1046/j.1460-9568.1999.00446.x
1447 63. Góis ZHTD, Tort ABL. Characterizing speed cells in the rat hippocampus. Cell Rep.
1448 2018;25: 1872–1884. doi:10.1016/j.celrep.2018.10.054
1449 64. Iwase M, Kitanishi T, Mizuseki K. Cell type, sub-region, and layer-specific speed
1450 representation in the hippocampal–entorhinal circuit. Sci Rep. 2020;10: 1–23.
1451 doi:10.1038/s41598-020-58194-1
1452 65. Zingg B, Chou X lin, Zhang Z gang, Mesik L, Liang F, Tao HW, et al. AAV-mediated
1453 anterograde transsynaptic tagging: mapping corticocollicular input-defined neural
1454 pathways for defense behaviors. Neuron. 2017;93: 33–47.
1455 doi:10.1016/j.neuron.2016.11.045
1456 66. Leranth C, Deller T, Buzsáki G. Intraseptal connections redefined: lack of a lateral
1457 septum to medial septum path. Brain Res. 1992;583: 1–11. doi:10.1016/S0006-
1458 8993(10)80004-6
1459 67. Staiger JF, Nürnberger F. The efferent connections of the lateral septal nucleus in the
1460 guinea pig: projections to the diencephalon and brainstem. Cell Tissue Res. 1991;264:
1461 391–413. doi:10.1007/BF00319031
1462 68. Witter MP, Daelmans HE, Jorritsma-Byham B, Staiger JF, Wouterlood FG. Restricted
1463 origin and distribution of projections from the lateral to the medial septal complex in
1464 rat and guinea pig. Neurosci Lett. 1992;148: 164–168. Available:
1465 http://www.ncbi.nlm.nih.gov/entrez/query.fcgi?cmd=Retrieve&db=PubMed&dopt=Cit

ation&list_uids=1284441

69. Beier KT, Steinberg EE, Deloach KE, Kremer EJ, Malenka RC, Luo L, et al. Circuit architecture of VTA dopamine neurons revealed by systematic input-output mapping. Cell. 2015;162: 622–634. doi:10.1016/j.cell.2015.07.015

70. Jung MW, Wiener SI, McNaughton BL. Comparison of spatial firing characteristics of units in dorsal and ventral hippocampus of the rat. J Neurosci. 1994;14: 7347–7356. doi:10.1523/jneurosci.14-12-07347.1994

71. Kjelstrup KB, Solstad T, Brun VH, Hafting T, Leutgeb S, Witter MP, et al. Finite scale of spatial representation in the hippocampus. Science. 2008;321: 140–143. doi:10.1126/science.1157086

72. Maurer AP, Cowen SL, Burke SN, Barnes CA, McNaughton BL. Phase precession in hippocampal interneurons showing strong functional coupling to individual pyramidal cells. J Neurosci. 2006;26: 13485–13492. doi:10.1523/JNEUROSCI.2882-06.2006

73. Taube J, Muller R, Ranck J. Head-direction cells recorded from the postsubiculum in freely moving rats. I. Description and quantitative analysis. J Neurosci. 1990;10: 420–435. doi:10.1523/jneurosci.10-02-00420.1990

74. Taube JS, Muller RU, Ranck JB. Head-direction cells recorded from the postsubiculum in freely moving rats. II. Effects of environmental manipulations. J Neurosci. 1990;10: 436–447. doi:10.1523/jneurosci.10-02-00436.1990

75. Taube JS. Head direction cells recorded in the anterior thalamic nuclei of freely moving rats. J Neurosci. 1995;15: 70–86. doi:10.1523/jneurosci.15-01-00070.1995

76. Stackman RW, Taube JS. Firing properties of rat lateral mammillary single units: Head direction, head pitch, and angular head velocity. J Neurosci. 1998;18: 9020–9037. doi:10.1523/jneurosci.18-21-09020.1998

77. Sargolini F, Fyhn M, Hafting T, McNaughton BL, Witter MP, Moser MB, et al.

Conjunctive representation of position, direction, and velocity in entorhinal cortex. Science. 2006;312: 758–762. doi:10.1126/science.1125572

78. Chen LL, Lin LH, Green EJ, Barnes CA, McNaughton BL. Head-direction cells in the rat posterior cortex. I. Anatomical distribution and behavioral modulation. Exp Brain Res. 1994;101: 8–23. doi:10.1007/BF00243212

79. Sharp PE, Blair HT, Cho J. The anatomical and computational basis of the rat head-direction cell signal. Trends Neurosci. 2001;24: 289–294. doi:10.1016/s0030-6657(08)70226-9

80. Boccara CN, Sargolini F, Thoresen VH, Solstad T, Witter MP, Moser EI, et al. Grid cells in pre-and parasubiculum. Nat Neurosci. 2010;13: 987–994. doi:10.1038/nn.2602

81. Cacucci F, Lever C, Wills TJ, Burgess N, O'Keefe J. Theta-modulated place-by-direction cells in the hippocampal formation in the rat. J Neurosci. 2004;24: 8265–8277. doi:10.1523/JNEUROSCI.2635-04.2004

82. Oh SW, Harris JA, Ng L, Winslow B, Cain N, Mihalas S, et al. A mesoscale connectome of the mouse brain. Nature. 2014;508: 207–214. doi:10.1038/nature13186

83. Eichenbaum H. Time cells in the hippocampus: A new dimension for mapping memories. Nat Rev Neurosci. 2014;15: 732–744. doi:10.1038/nrn3827

84. Pastalkova E, Itskov V, Amarasingham A, Buzsáki G. Internally generated cell assembly sequences in the rat hippocampus. Science. 2008;321: 1322–1328. doi:10.1126/science.1159775

85. Deshmukh SS, Bhalla US. Representation of odor habituation and timing in the hippocampus. J Neurosci. 2003;23: 1903–1915. doi:10.1523/jneurosci.23-05-01903.2003

86. MacDonald CJ, Carrow S, Place R, Eichenbaum H. Distinct hippocampal time cell sequences represent odor memories in immobilized rats. J Neurosci. 2013;33: 14607–

14616. doi:10.1523/JNEUROSCI.1537-13.2013

87. Aronov D, Nevers R, Tank DW. Mapping of a non-spatial dimension by the hippocampal-entorhinal circuit. Nature. 2017;543: 719–722. doi:10.1038/nature21692

88. Alonso JR, Frotscher M. Organization of the septal region in the rat brain: a Golgi EM study of lateral septal neurons. J Comp Neurol. 1989;286: 472–487.

89. Staiger JF, Nürnberger F. Pattern of afferents to the lateral septum in the guinea pig. Cell Tissue Res. 1989;257: 471–490. doi:10.1007/BF00221457

90. Phelan KD, Hasuo H, Twery MJ, Gallagher JP. Projection neurons in the rat dorsolateral septal nucleus possess recurrent axon collaterals. Neurosci Lett. 1989;97: 259–265. doi:10.1016/0304-3940(89)90607-1

91. Isely G, Hillar CJ, Sommer FT. Deciphering subsampled data: Adaptive compressive sampling as a principle of brain communication. Adv Neural Inf Process Syst 23 24th Annu Conf Neural Inf Process Syst 2010, NIPS 2010. 2010; 1–9.

92. Palm G, Sommer FT. Associative data storage and retrieval in neural networks. Domany E., van Hemmen JL, Schulten K, editors. Models of Neural Networks III. Physics of Neural Networks. Springer, New York, NY.; 2006.

93. Staiger JF, Nürnberger F. The efferent connections of the lateral septal nucleus in the guinea pig: intrinsic connectivity of the septum and projections to other telencephalic areas. Cell Tissue Res. 1991;264: 415–426. doi:10.1007/BF00319032

94. Tóth K, Borhegyi Z, Freund TF. Postsynaptic targets of GABAergic hippocampal neurons in the medial septum-diagonal band of broca complex. J Neurosci. 1993;13: 3712–3724. doi:10.1523/jneurosci.1413-04.2004

95. Manseau F, Goutagny R, Danik M, Williams S. The hippocamposeptal pathway generates rhythmic firing of GABAergic neurons in the medial septum and diagonal bands: an investigation using a complete septohippocampal preparation in vitro. J

Neurosci. 2008;28: 4096–4107. doi:10.1523/JNEUROSCI.0247-08.2008

96. Leão RN, Targino ZH, Colom L V., Fisahn A. Interconnection and synchronization of neuronal populations in the mouse medial septum/diagonal band of Broca. J Neurophysiol. 2015;113: 971–980. doi:10.1152/jn.00367.2014

97. Patel J, Schomburg EW, Bere A, Fujisawa S. Local generation and propagation of ripples along the septotemporal axis of the hippocampus. 2013;33: 17029–17041. doi:10.1523/JNEUROSCI.2036-13.2013

98. Robinson J, Manseau F, Ducharme G, Vigneault E, El Mestikawy S, Williams S. Optogenetic activation of septal glutamatergic neurons drive hippocampal theta rhythms. 2016;36: 3016–3023. doi:10.1523/JNEUROSCI.2141-15.2016

99. Buzsáki G. Theta oscillations in the hippocampus. Neuron. 2002;33: 325–340. doi:10.1016/S0896-6273(02)00586-X

100. Fuhrmann F, Justus D, Sosulina L, Kaneko H, Beutel T, Friedrichs D, et al. Locomotion, theta oscillations, and the speed-correlated firing of hippocampal neurons are controlled by a medial septal glutamatergic circuit. Neuron. 2015;86: 1253–1264. doi:10.1016/j.neuron.2015.05.001

101. Justus D, Dalügge D, Bothe S, Fuhrmann F, Hannes C, Kaneko H, et al. Glutamatergic synaptic integration of locomotion speed via septoentorhinal projections. Nat Neurosci. 2017;20: 16–19. doi:10.1038/nn.4447

102. Stuber GD, Wise RA. Lateral hypothalamic circuits for feeding and reward. Nat Neurosci. 2016;19: 198–205. doi:10.1016/j.physbeh.2017.03.040

103. Burdakov D, Peleg-Raibstein D. The hypothalamus as a primary coordinator of memory updating. Physiol Behav. 2020;223: 112988. doi:10.1016/j.physbeh.2020.112988

104. Aitta-Aho T, Pappa E, Burdakov D, Apergis-Schoute J. Cellular activation of

hypothalamic hypocretin/orexin neurons facilitates short-term spatial memory in mice. Neurobiol Learn Mem. 2016;136: 183–188. doi:10.1016/j.nlm.2016.10.005

105. Izawa S, Chowdhury S, Miyazaki T, Mukai Y, Ono D, Inoue R, et al. REM sleep-active MCH neurons are involved in forgetting hippocampus-dependent memories. Science. 2019;365: 1308–1313. doi:10.1126/science.aax9238

106. Kosse C, Burdakov D. Natural hypothalamic circuit dynamics underlying object memorization. Nat Commun. 2019;10: 1–8. doi:10.1038/s41467-019-10484-7

107. Petrovich GD. Lateral hypothalamus as a motivation-cognition interface in the control of feeding behavior. Front Syst Neurosci. 2018;12: 1–7. doi:10.3389/fnsys.2018.00014

108. Gladfelter WE, Brobeck JR. Decreased spontaneous locomotor activity in the rat induced by hypothalamic lesions. Am J Physiol. 1962;203: 811–817. doi:10.1152/ajplegacy.1962.203.5.811

109. Grillner S, Wallén P, Saitoh K, Kozlov A, Robertson B. Neural bases of goal-directed locomotion in vertebrates-An overview. Brain Res Rev. 2008;57: 2–12. doi:10.1016/j.brainresrev.2007.06.027

110. Kosse C, Schöne C, Bracey E, Burdakov D. Orexin-driven GAD65 network of the lateral hypothalamus sets physical activity in mice. Proc Natl Acad Sci U S A. 2017;114: 4525–4530. doi:10.1073/pnas.1619700114

111. Sinnamon HM. Preoptic and hypothalamic neurons and the initiation of locomotion in the anesthetized rat. Prog Neurobiol. 1993;41: 323–344. doi:10.1016/0301-0082(93)90003-B

112. Mahler S V., Moorman DE, Smith RJ, James MH, Aston-Jones G. Motivational activation: A unifying hypothesis of orexin/hypocretin function. Nat Neurosci. 2014;17: 1298–1303. doi:10.1038/nn.3810

113. Mogenson GJ, Jones DL, Yim CY. From motivation to action: Functional interface

between the limbic system and the motor system. Prog Neurobiol. 1980;14: 69–97. doi:10.1016/0301-0082(80)90018-0

114. Callaway EM. Transneuronal circuit tracing with neurotropic viruses. Curr Opin Neurobiol. 2008;18: 617–623. doi:10.1016/j.conb.2009.03.007

115. Wickersham IR, Finke S, Conzelmann KK, Callaway EM. Retrograde neuronal tracing with a deletion-mutant rabies virus. Nat Methods. 2007;4: 47–49. doi:10.1038/nmeth999

116. Cai DJ, Aharoni D, Shuman T, Shobe J, Biane J, Song W, et al. A shared neural ensemble links distinct contextual memories encoded close in time. Nature. 2016;534: 115–118. doi:10.1038/nature17955

117. Ghosh KK, Burns LD, Cocker ED, Nimmerjahn A, Ziv Y, Gamal A El, et al. Miniaturized integration of a fluorescence microscope. Nat Methods. 2011;8: 871–878. doi:10.1038/nmeth.1694

118. Ting JT, Daigle TL, Chen Q, Feng G. Acute brain slice methods for adult and aging animals: Application of targeted patch clamp analysis and optogenetics. Methods Mol Biol. 2014;1183: 221–242. doi:10.1007/978-1-4939-1096-0_14

119. Pnevmatikakis EA, Giovannucci A. NoRMCorre: An online algorithm for piecewise rigid motion correction of calcium imaging data. J Neurosci Methods. 2017;291: 83–94. doi:10.1016/j.jneumeth.2017.07.031

120. Zhou P, Resendez SL, Rodriguez-Romaguera J, Jimenez JC, Neufeld SQ, Stuber GD, et al. Efficient and accurate extraction of in vivo calcium signals from microendoscopic video data. 2017. doi:http://arxiv.org/abs/1605.07266

121. Mathis A, Mamidanna P, Cury KM, Abe T, Murthy VN, Mathis MW, et al. DeepLabCut: markerless pose estimation of user-defined body parts with deep learning. Nat Neurosci. 2018;21: 1281–1289. doi:10.1038/s41593-018-0209-y

122. Nath T, Mathis A, Chen AC, Patel A, Bethge M, Mathis MW. Using DeepLabCut for 3D markerless pose estimation across species and behaviors. Nat Protoc. 2019;14: 2152–2176. doi:10.1038/s41596-019-0176-0

123. Cohen MX. Analyzing neural time series data: Theory and practice. Cambridge, MA: The MIT Press; 2014.

124. Sheintuch L, Rubin A, Brande-Eilat N, Geva N, Sadeh N, Pinchasof O, et al. Tracking the same neurons across multiple days in Ca2+ imaging data. Cell Rep. 2017;21: 1102–1115. doi:10.1016/j.celrep.2017.10.013

Figure 1

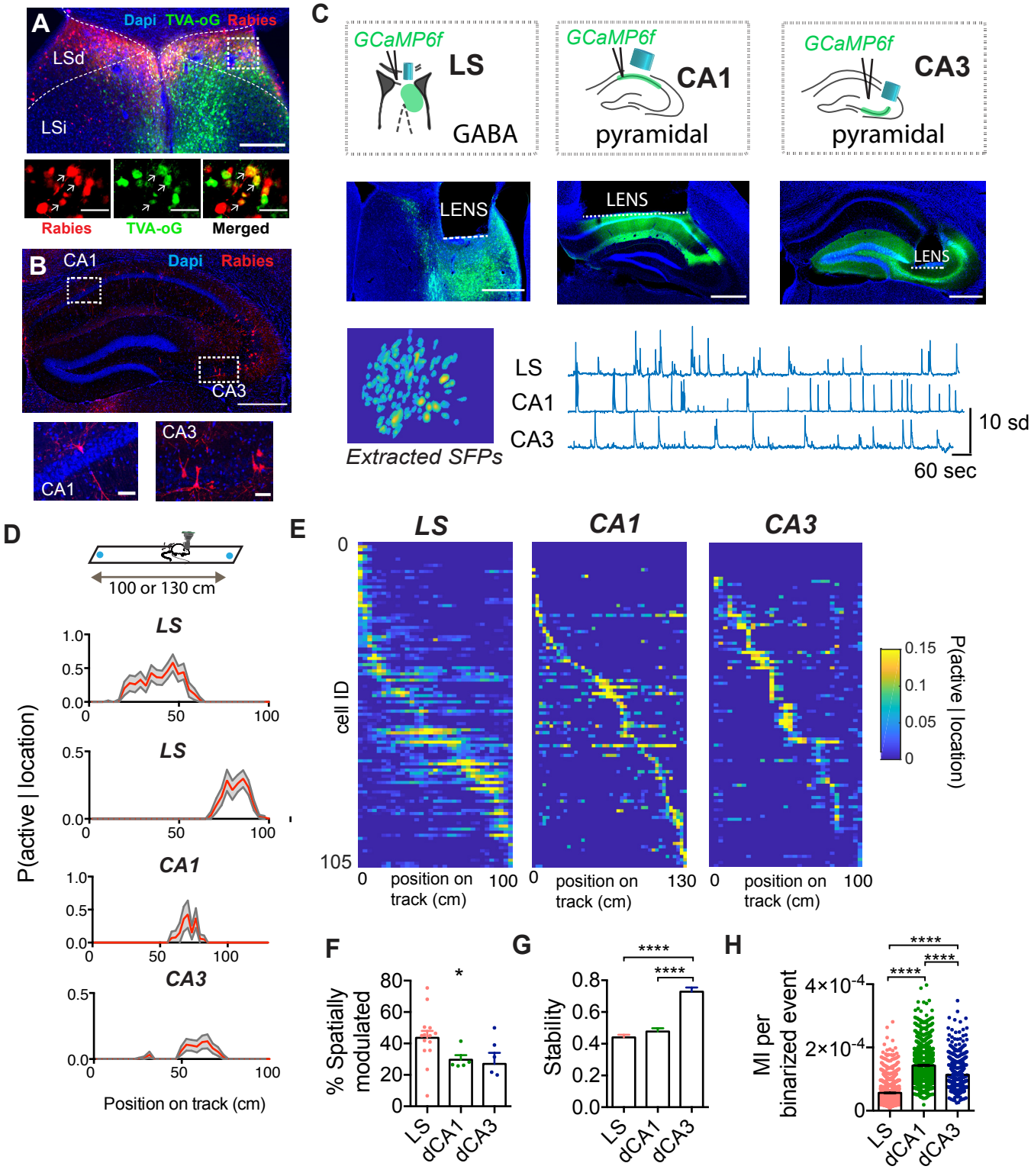

Figure 2

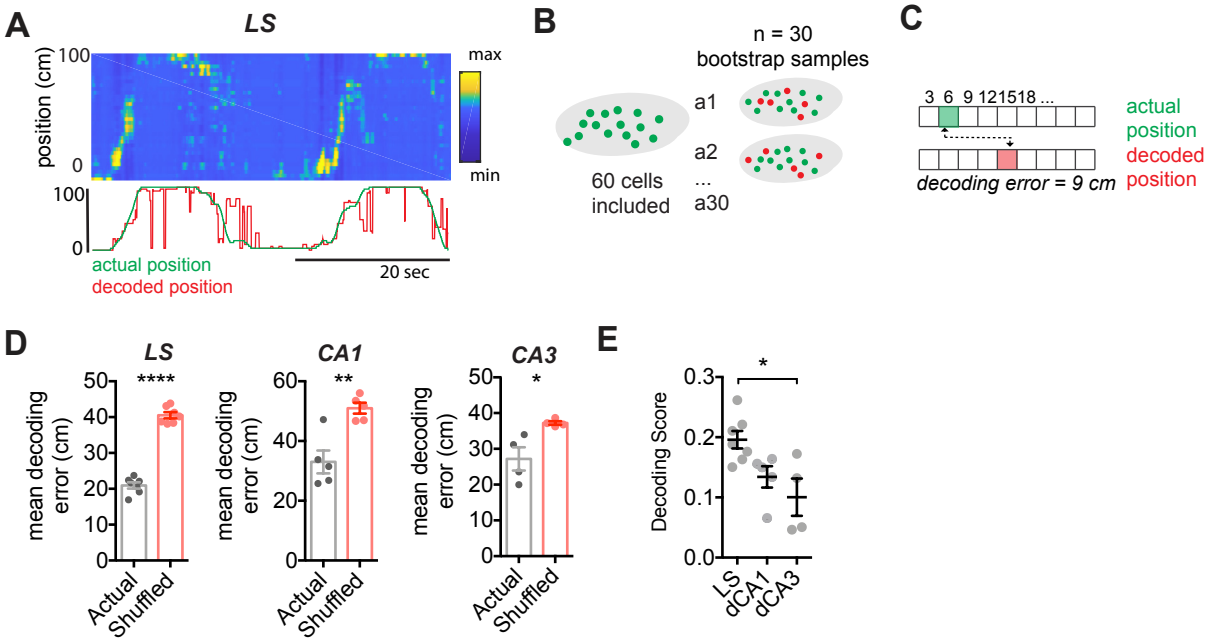

Figure 3

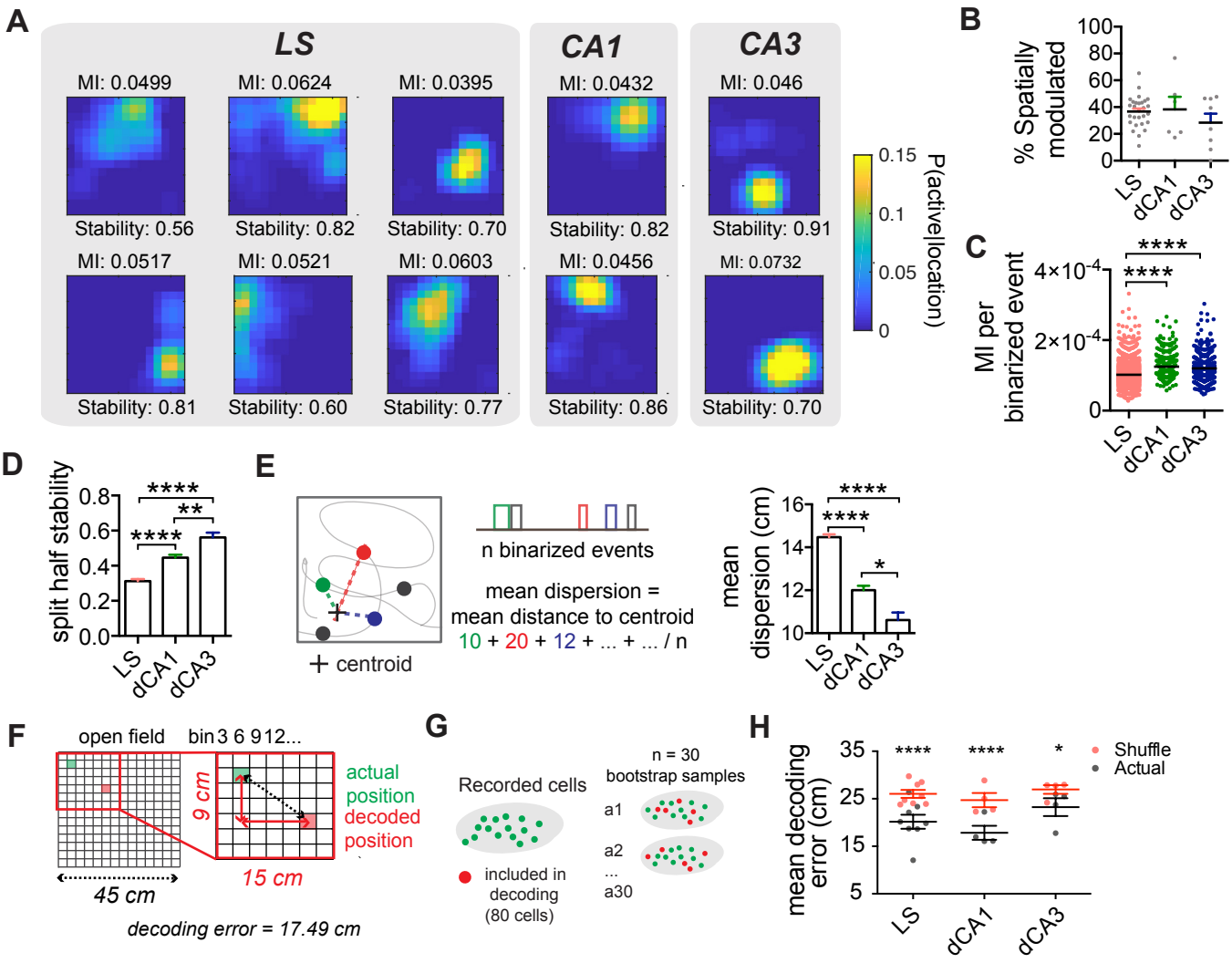

Figure 4

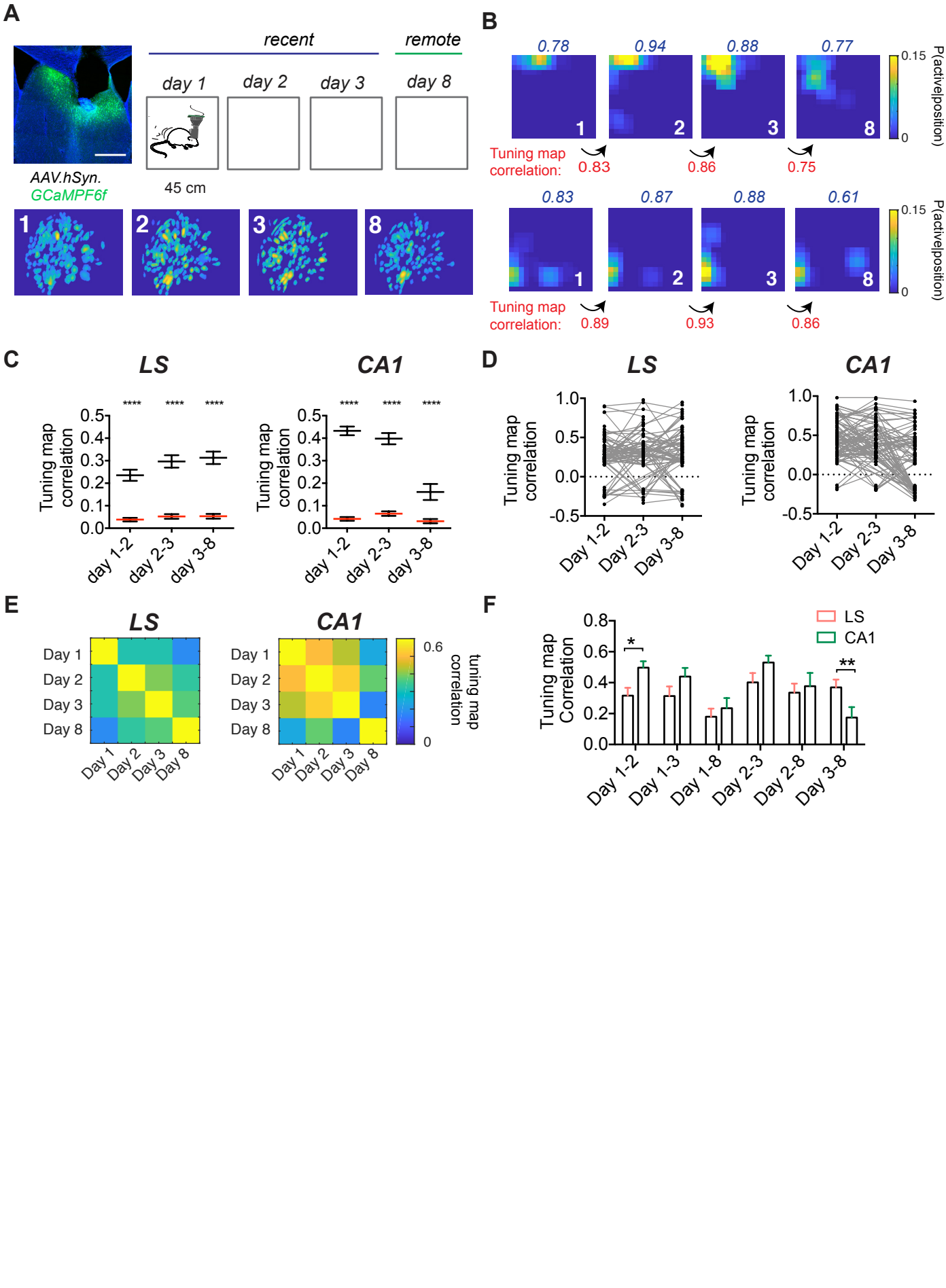

Figure 5

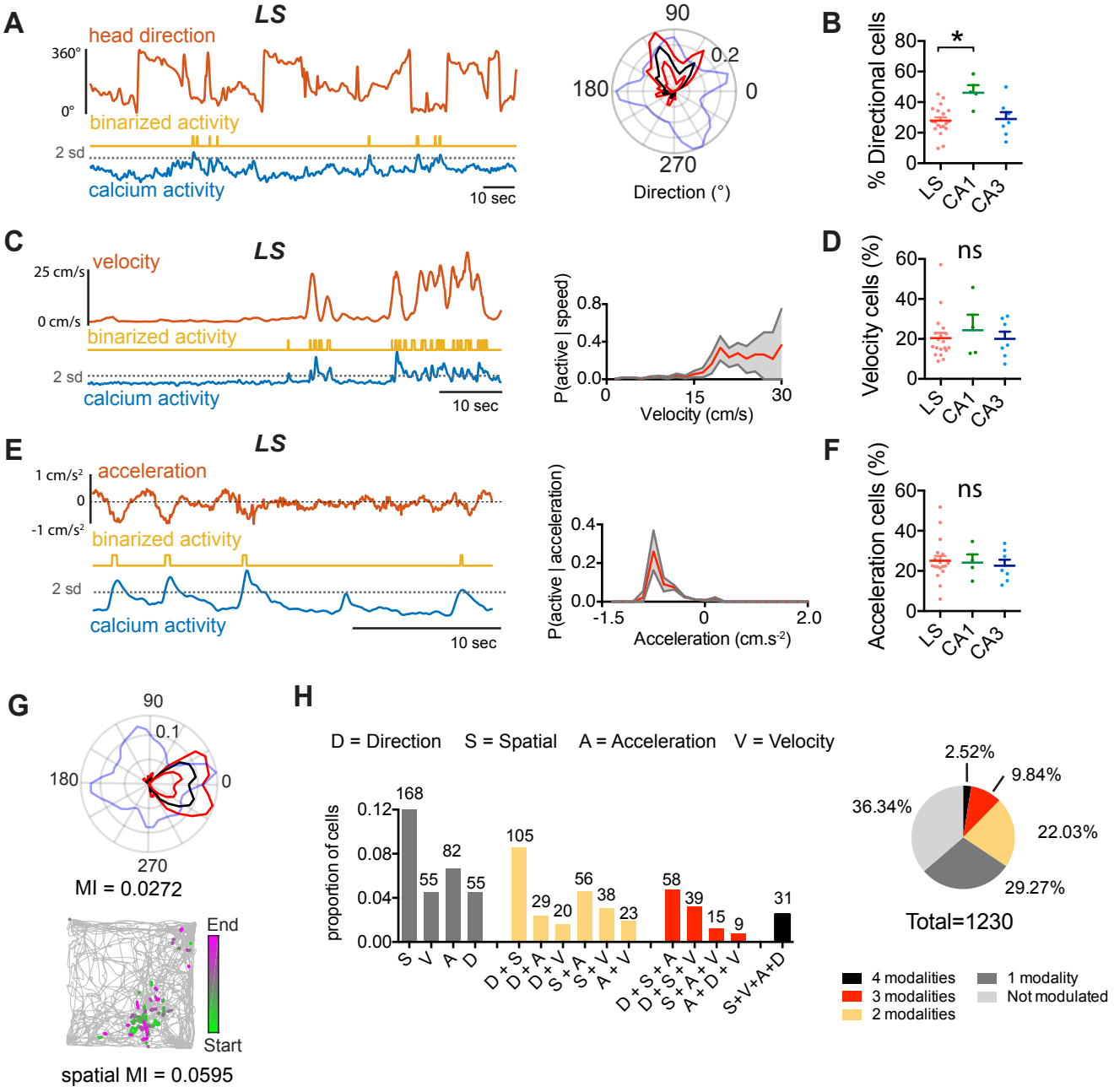

Figure 6

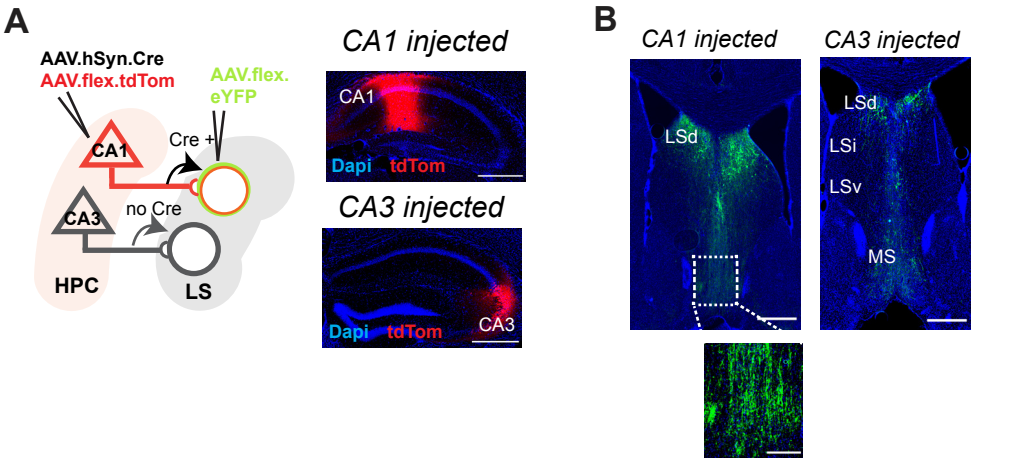

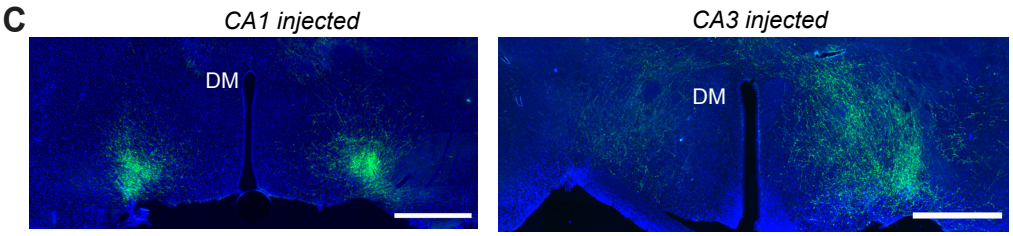

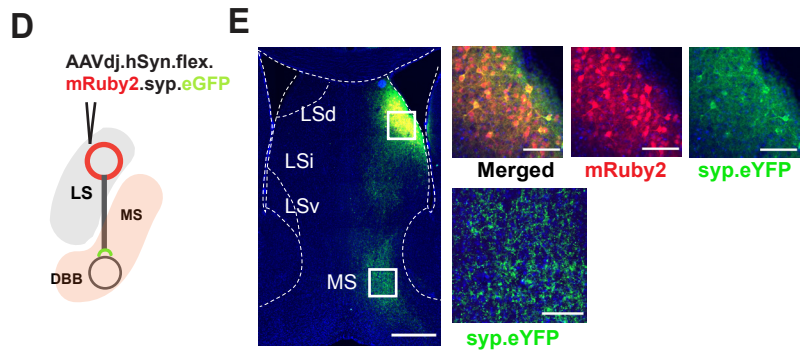

Figure 7

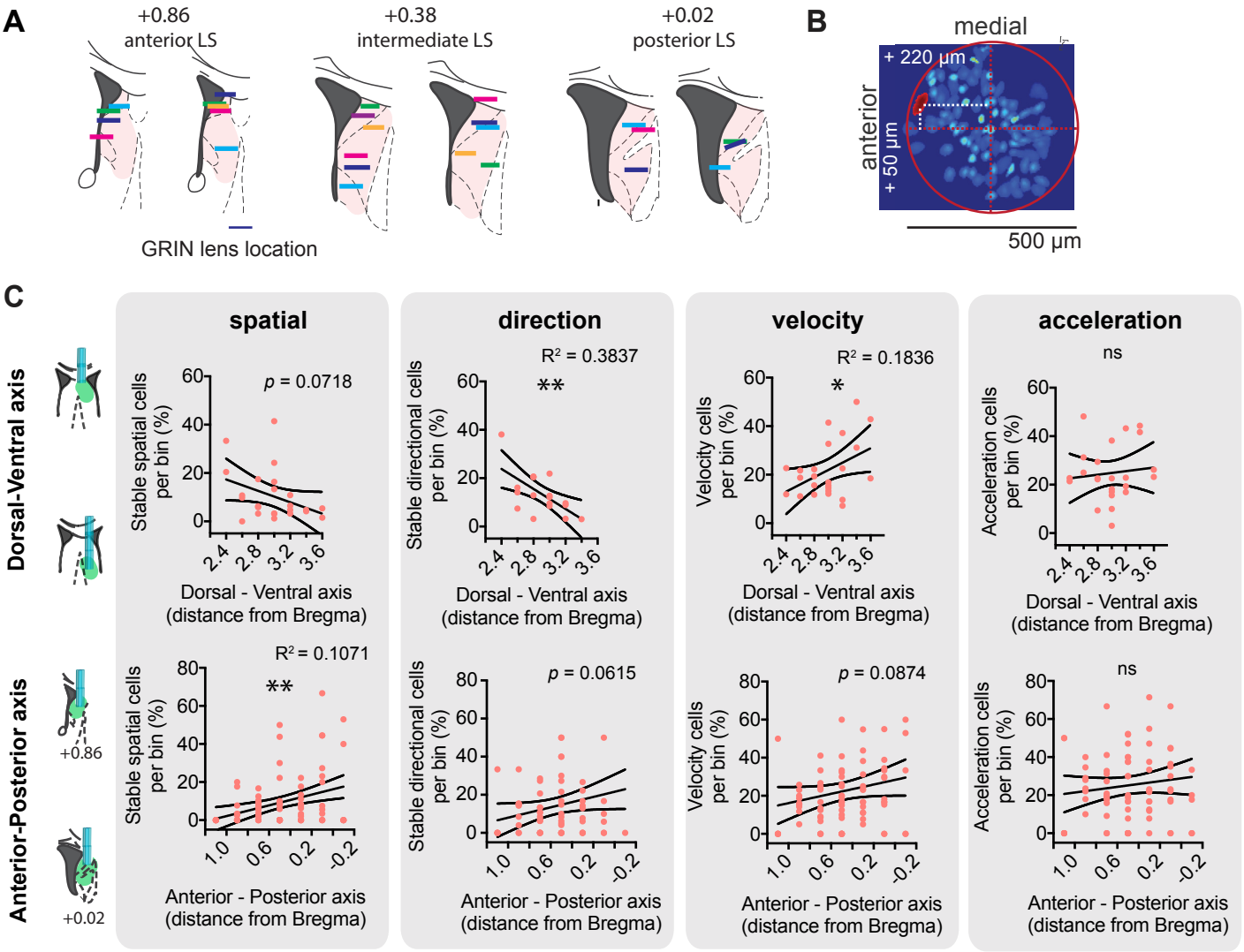

S1 Fig

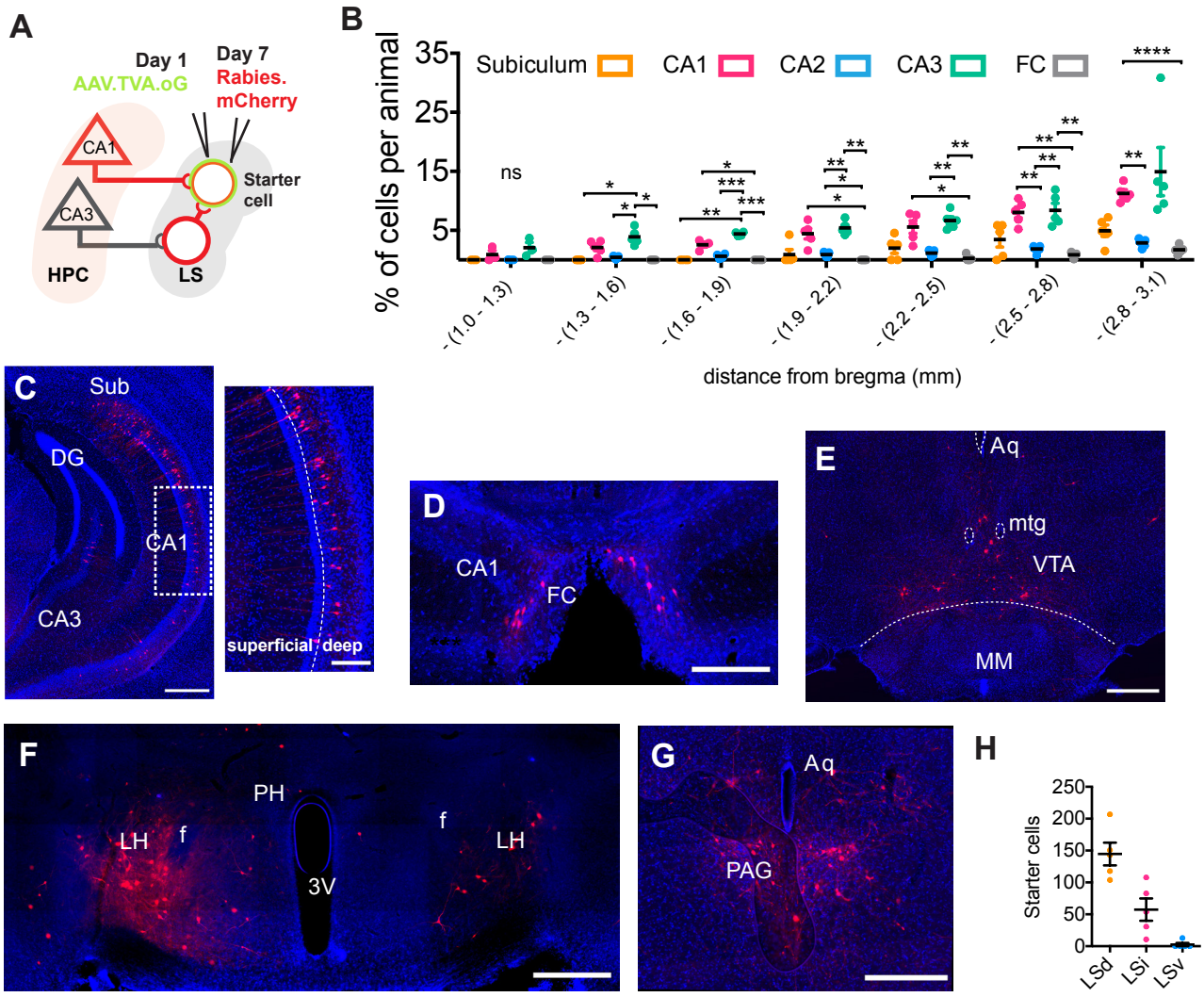

S2 Fig

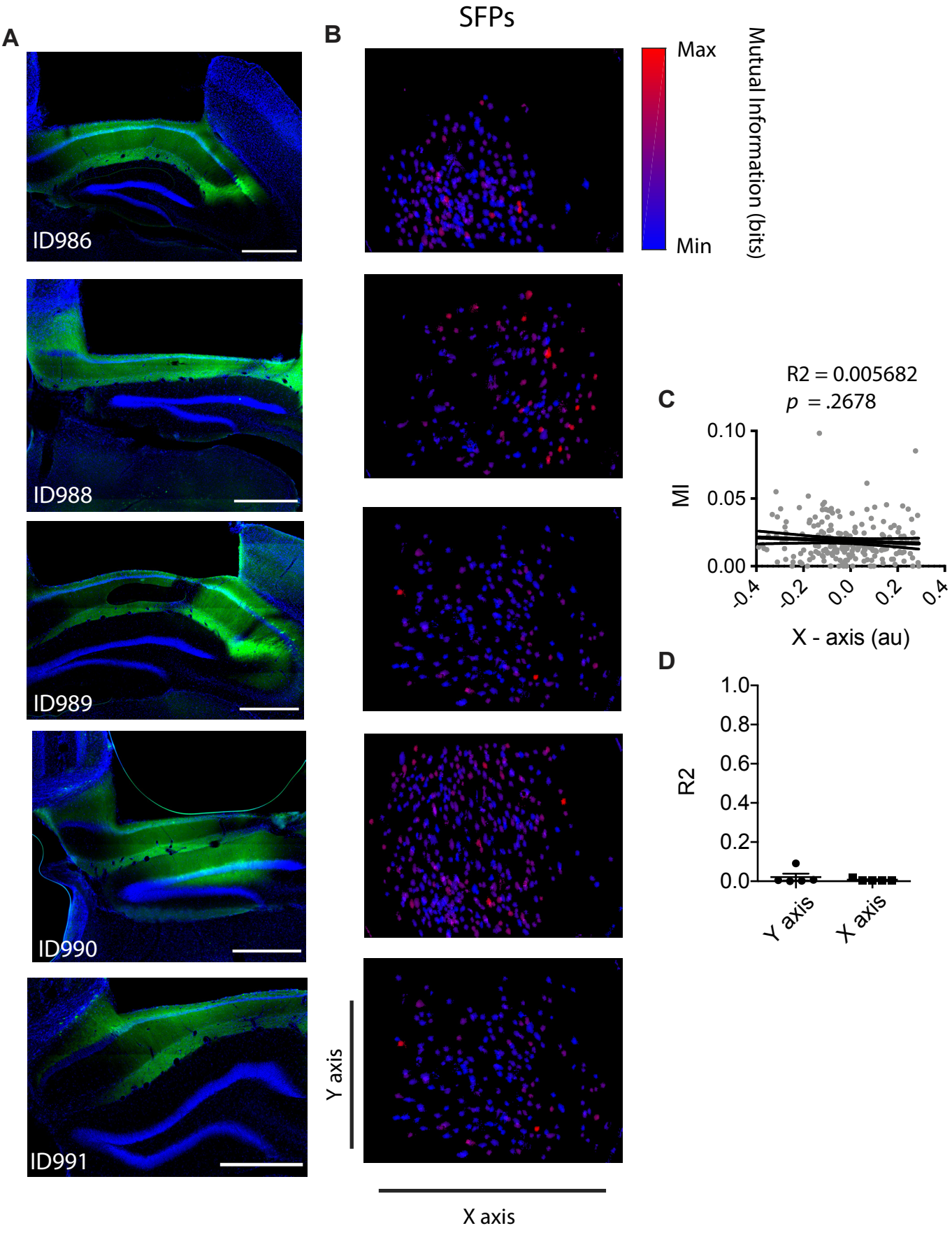

S3 Fig

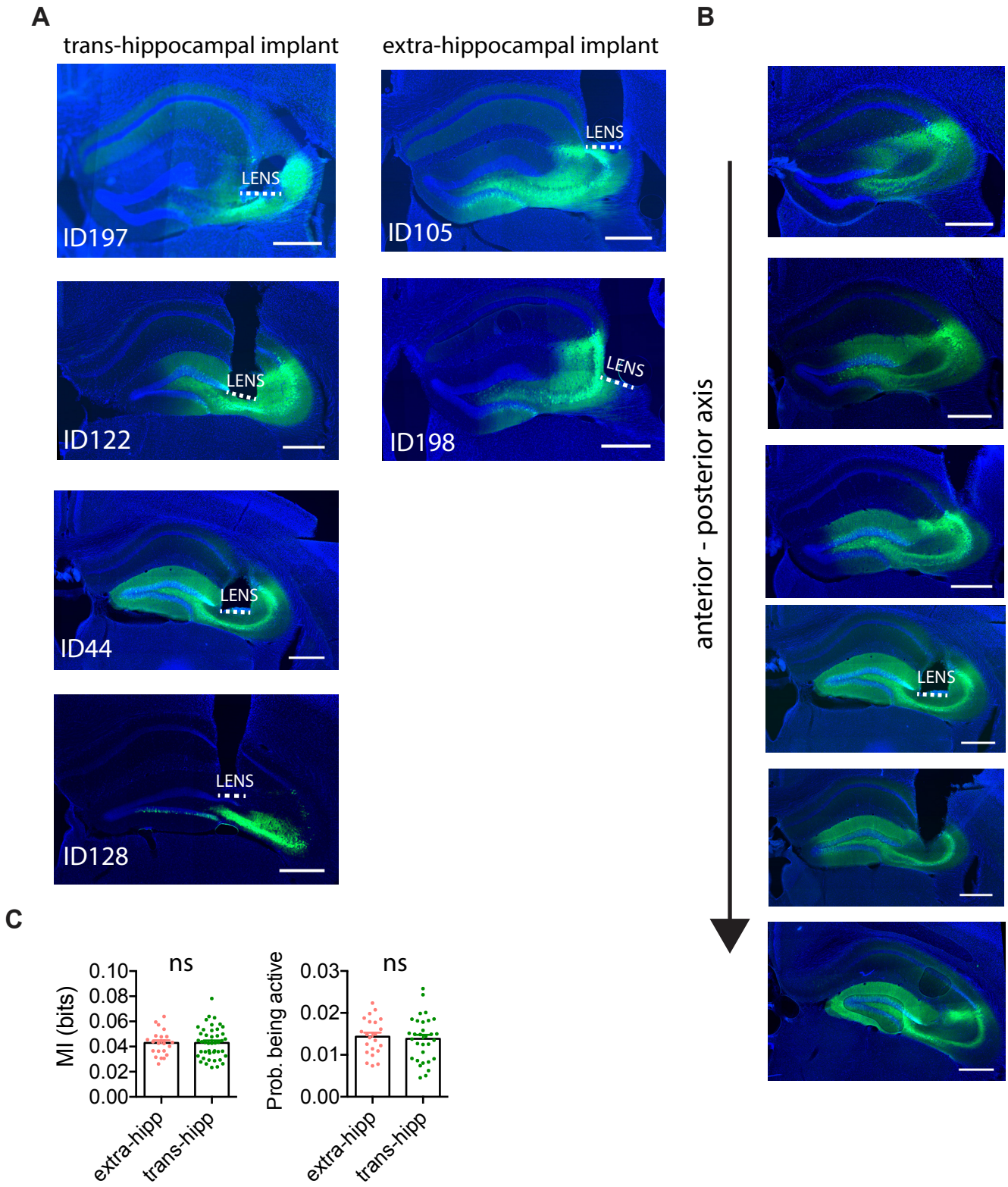

S4 Fig

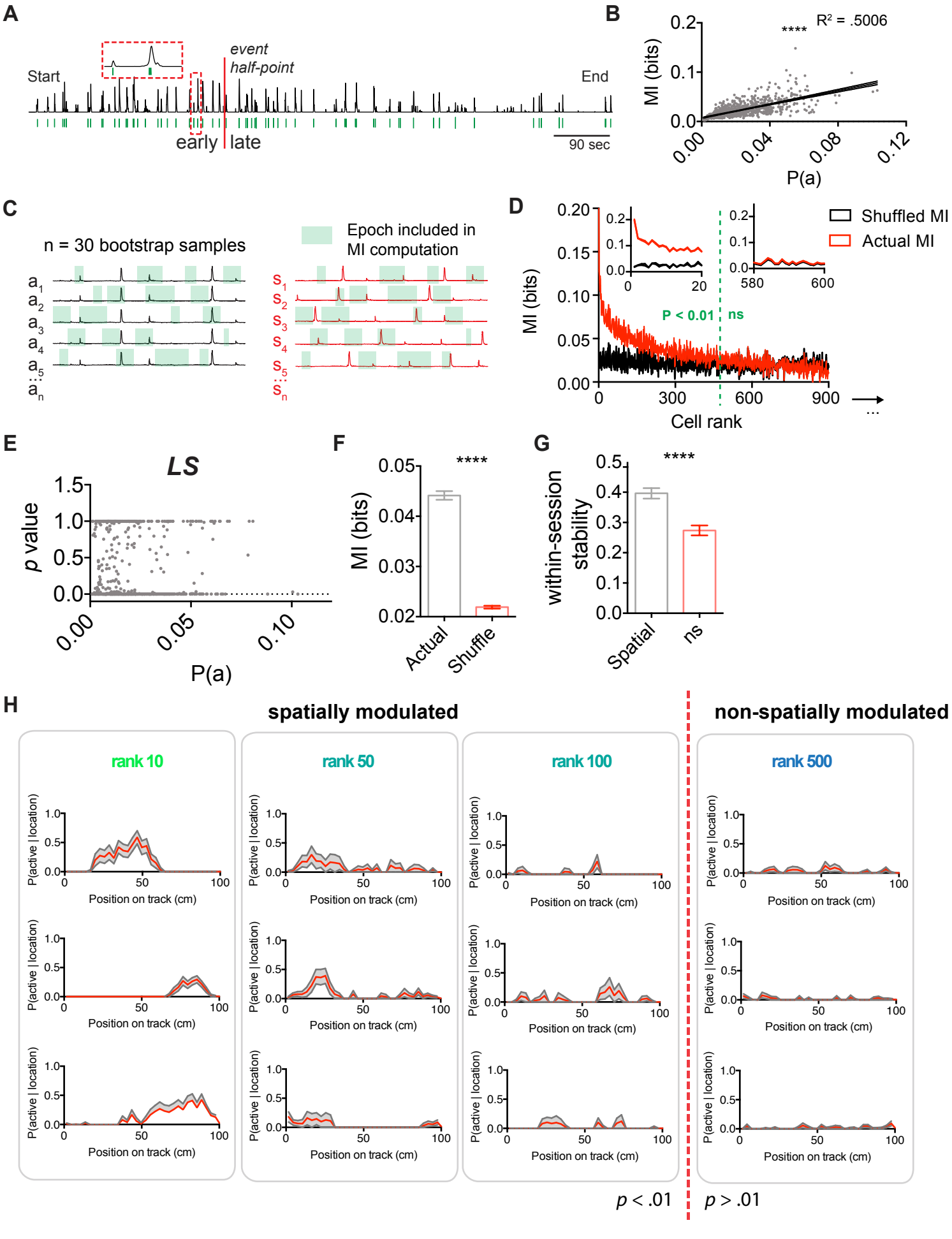

S5 Fig

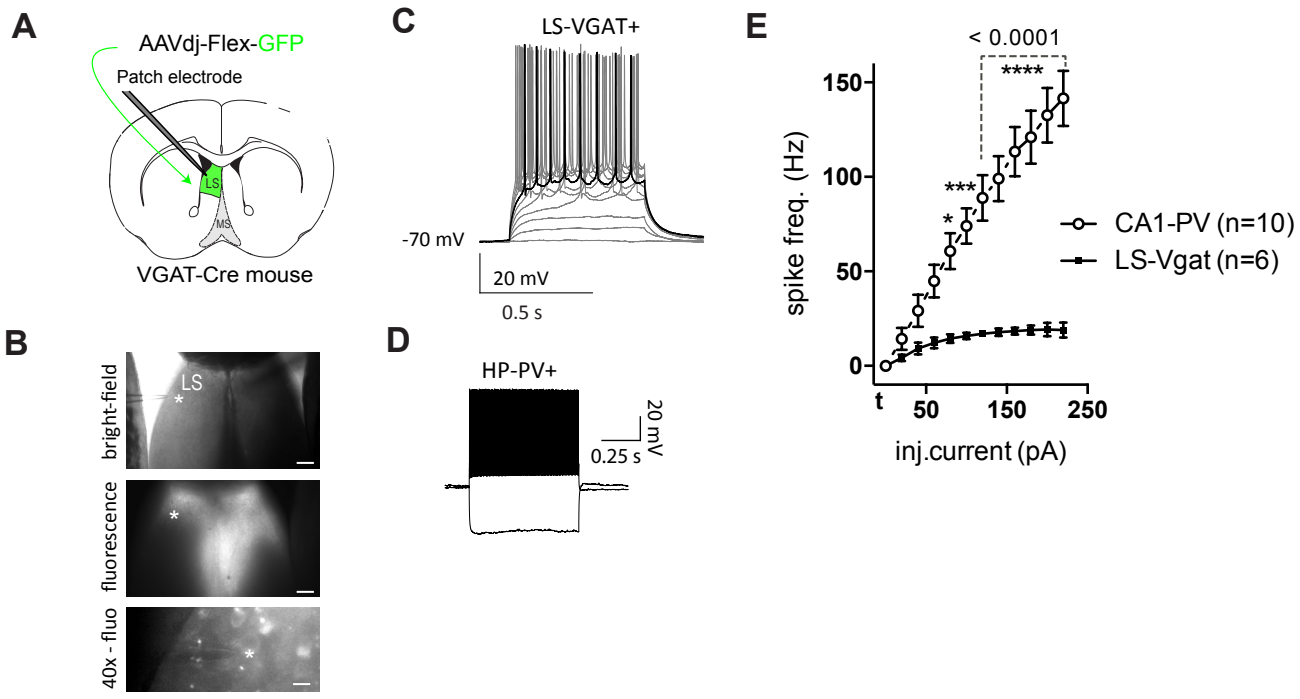

S6 Fig

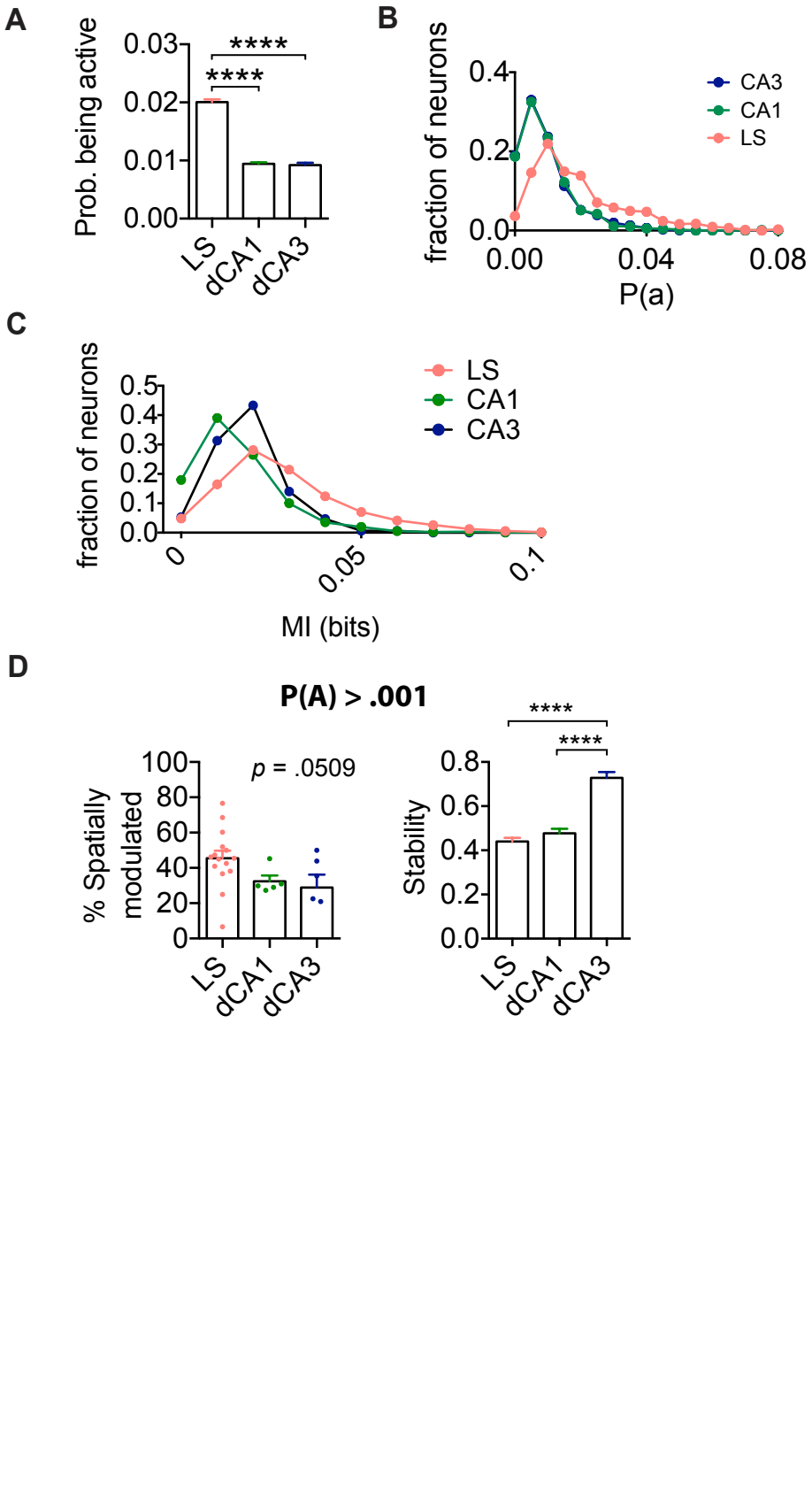

S7 Fig

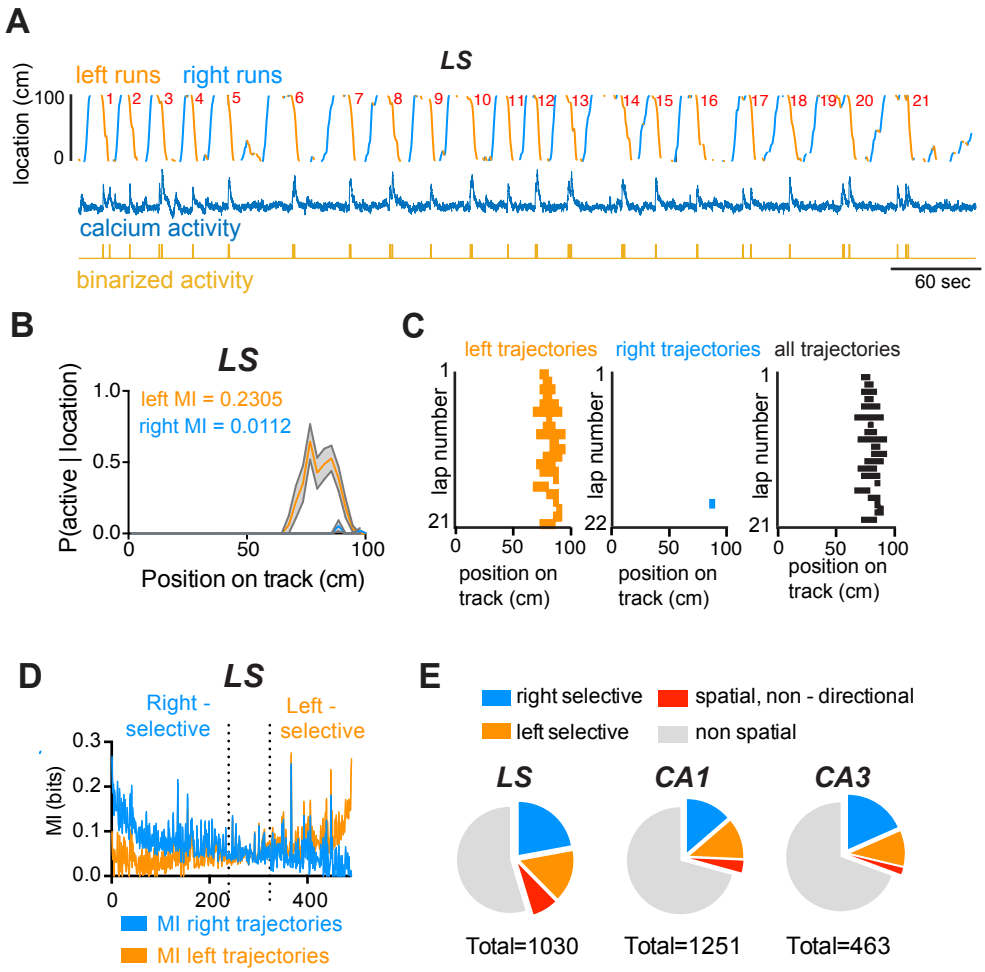

S8 Fig

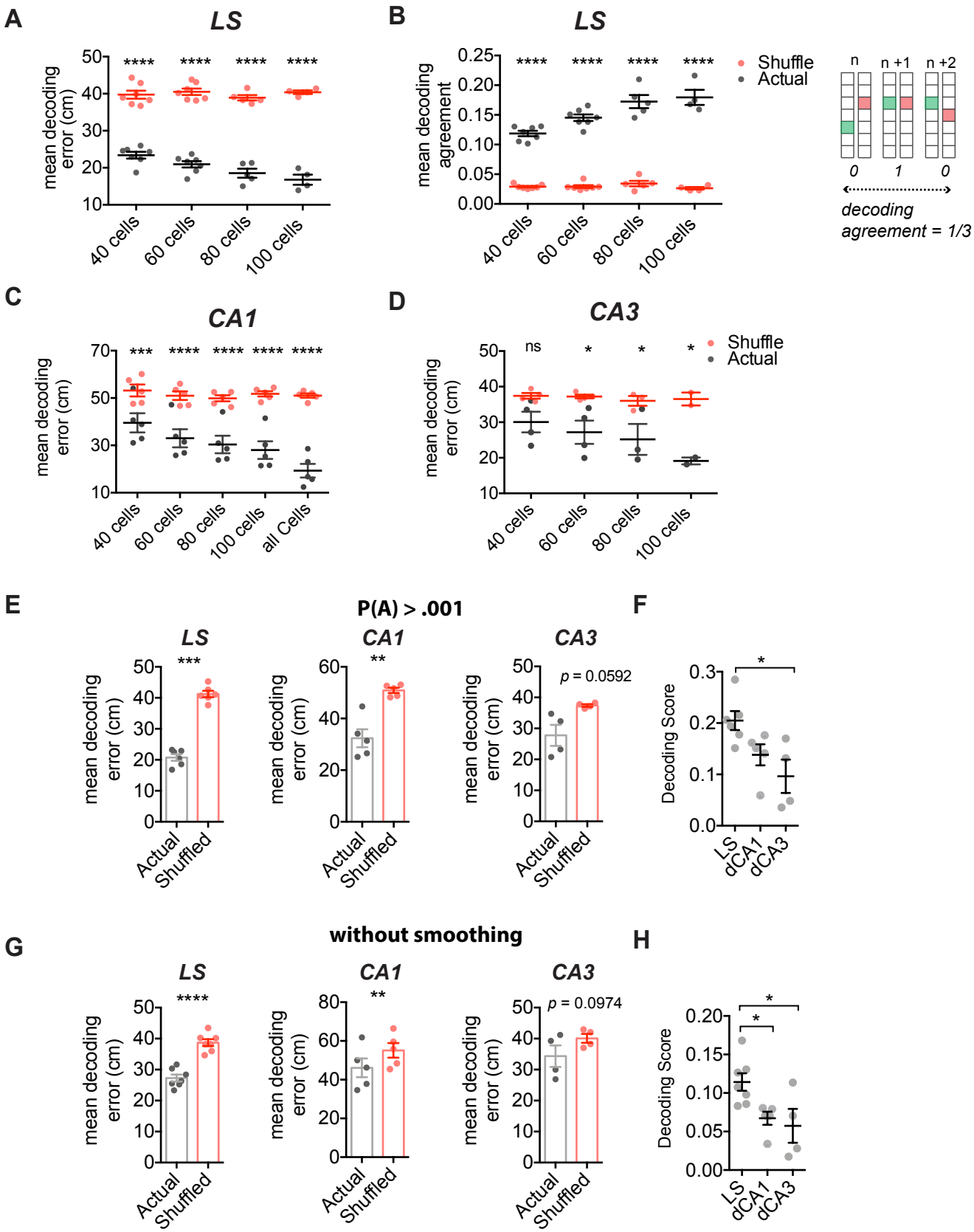

S9 Fig

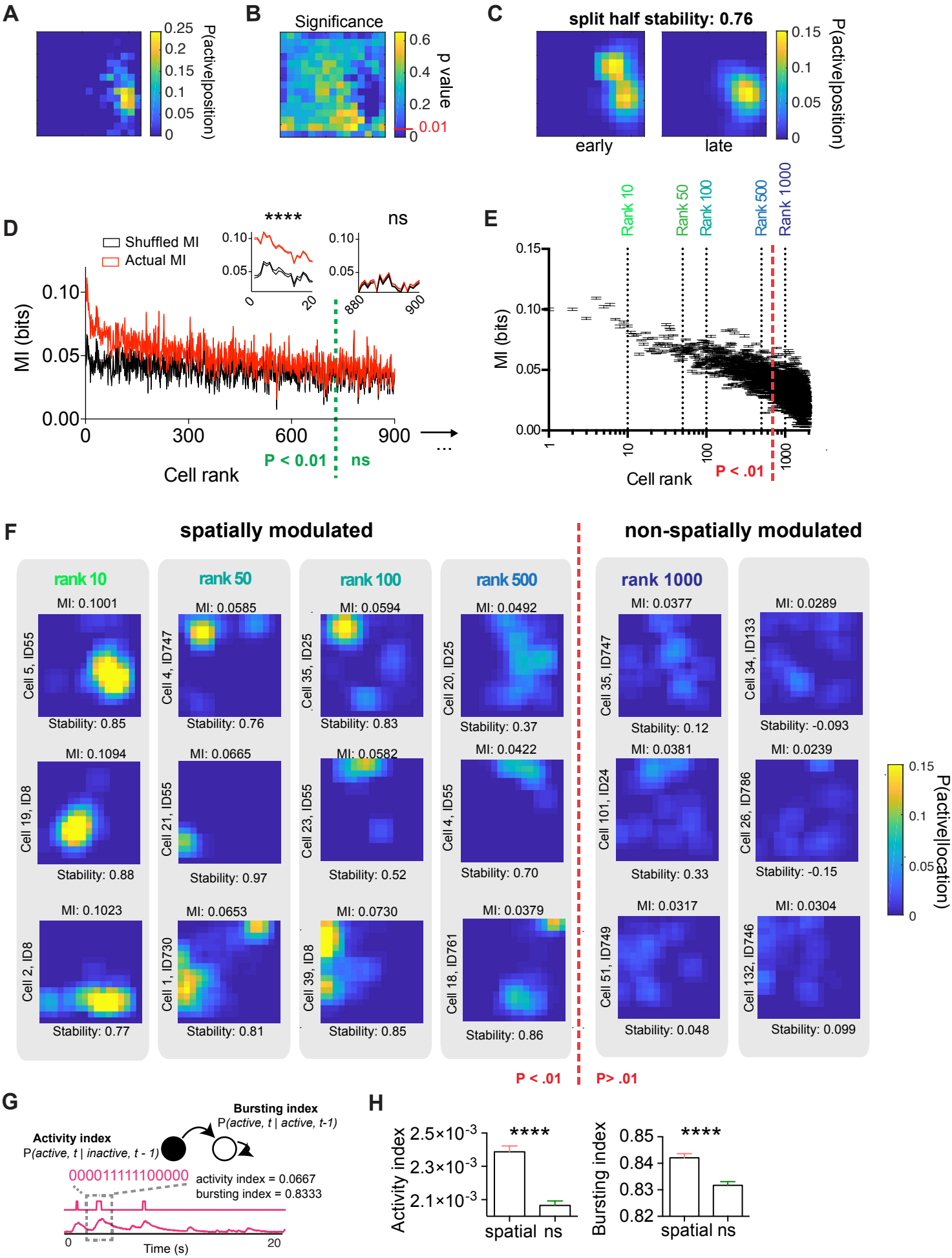

S10 Fig

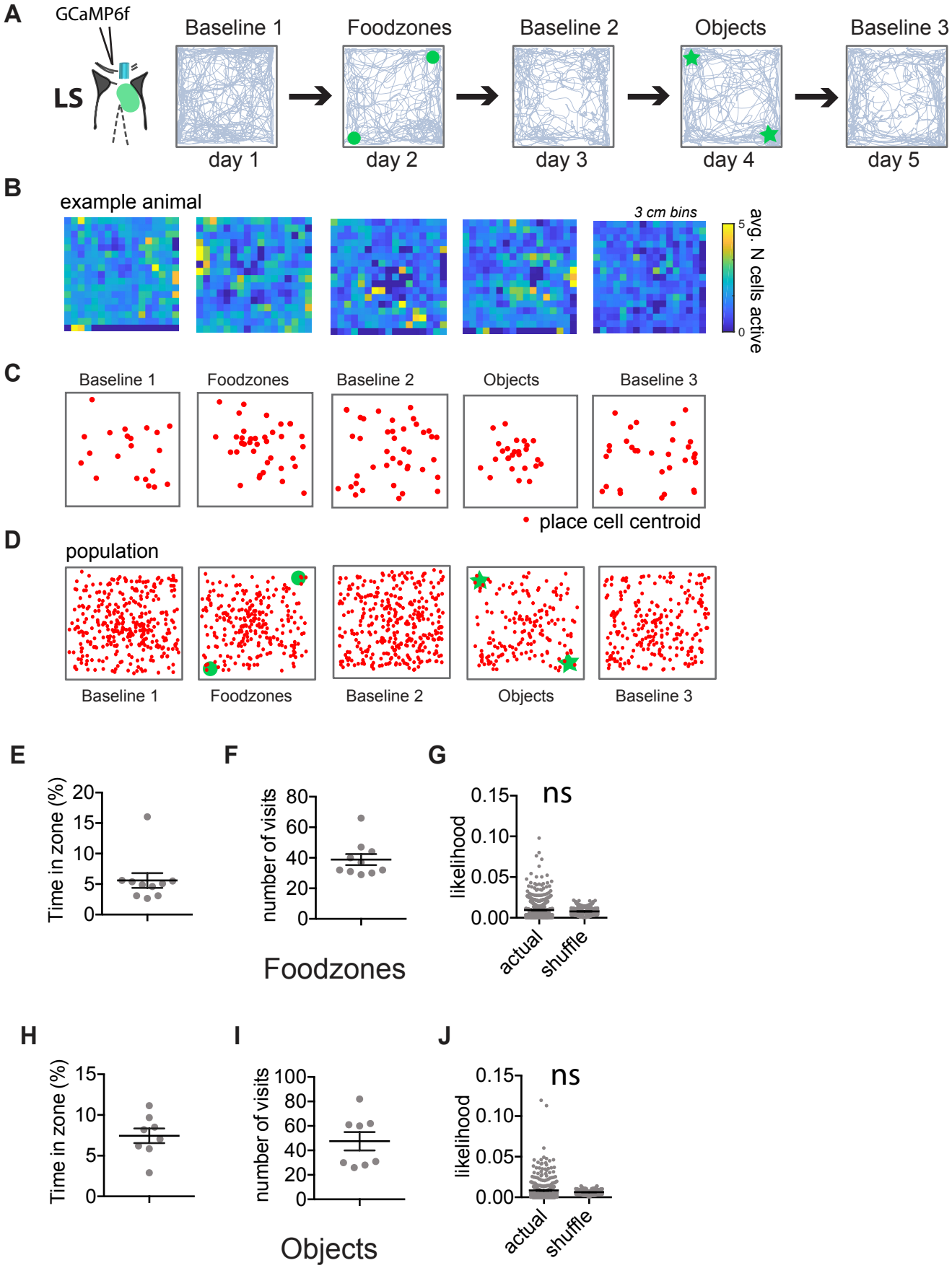

S11 Fig

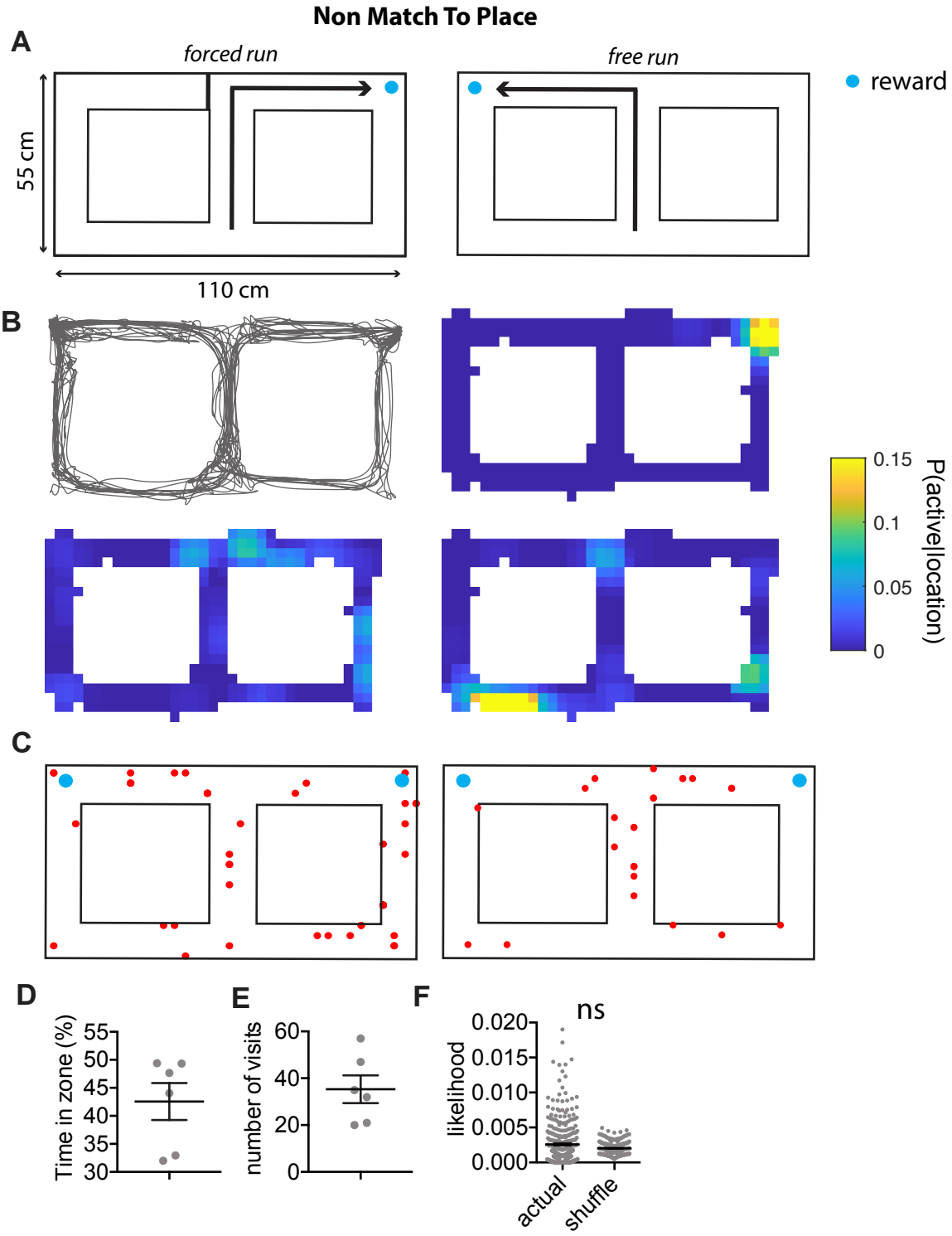

S12 Fig

P(A) > .001

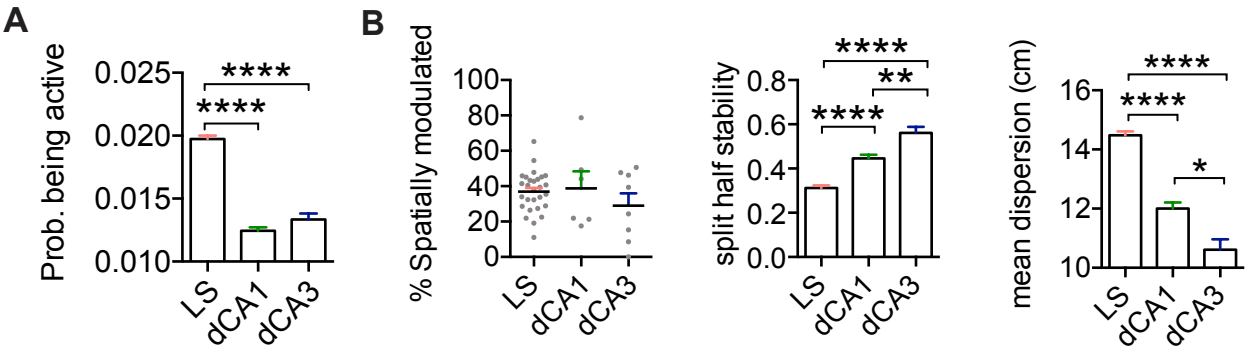

S13 Fig

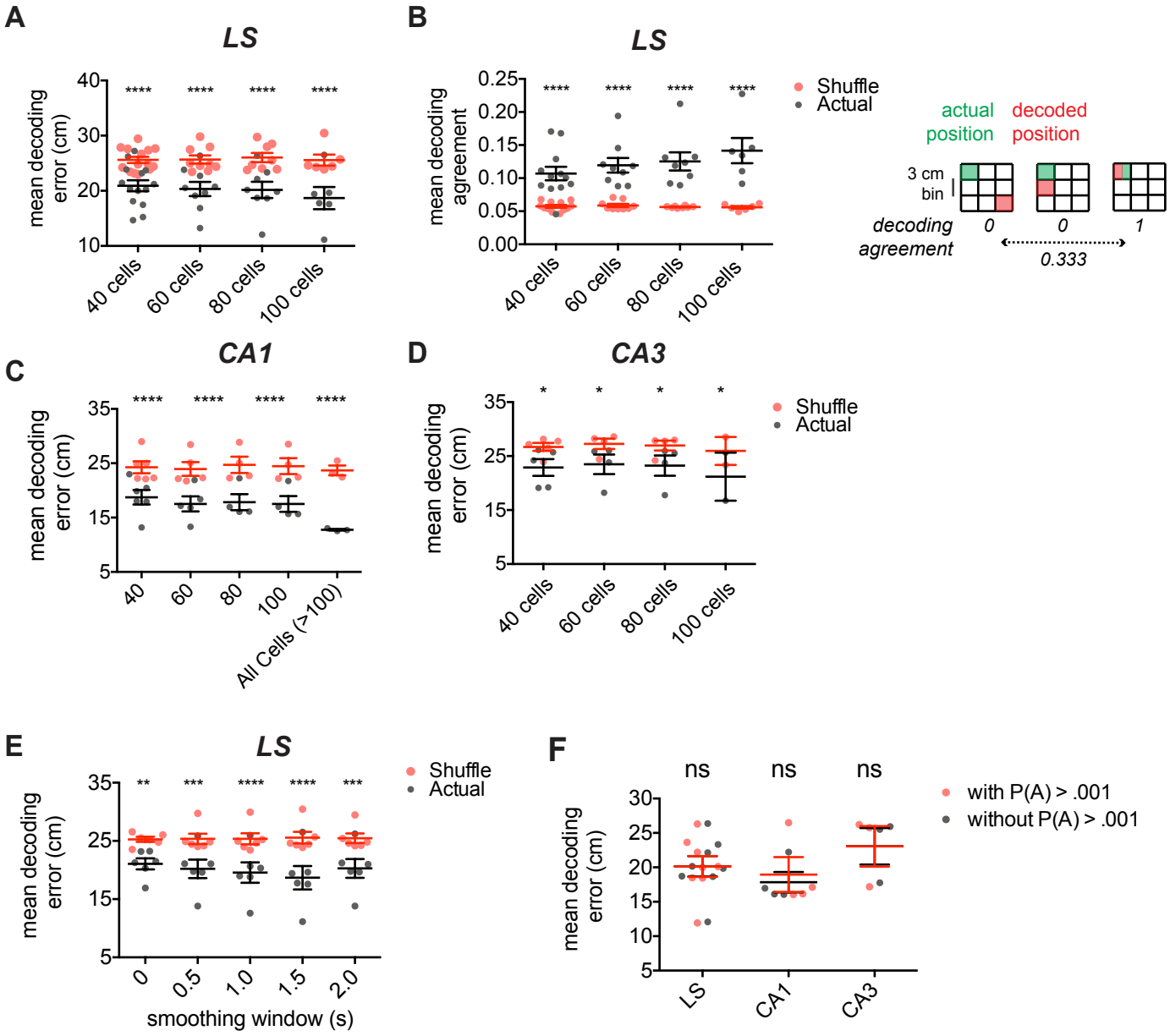

S14 Fig

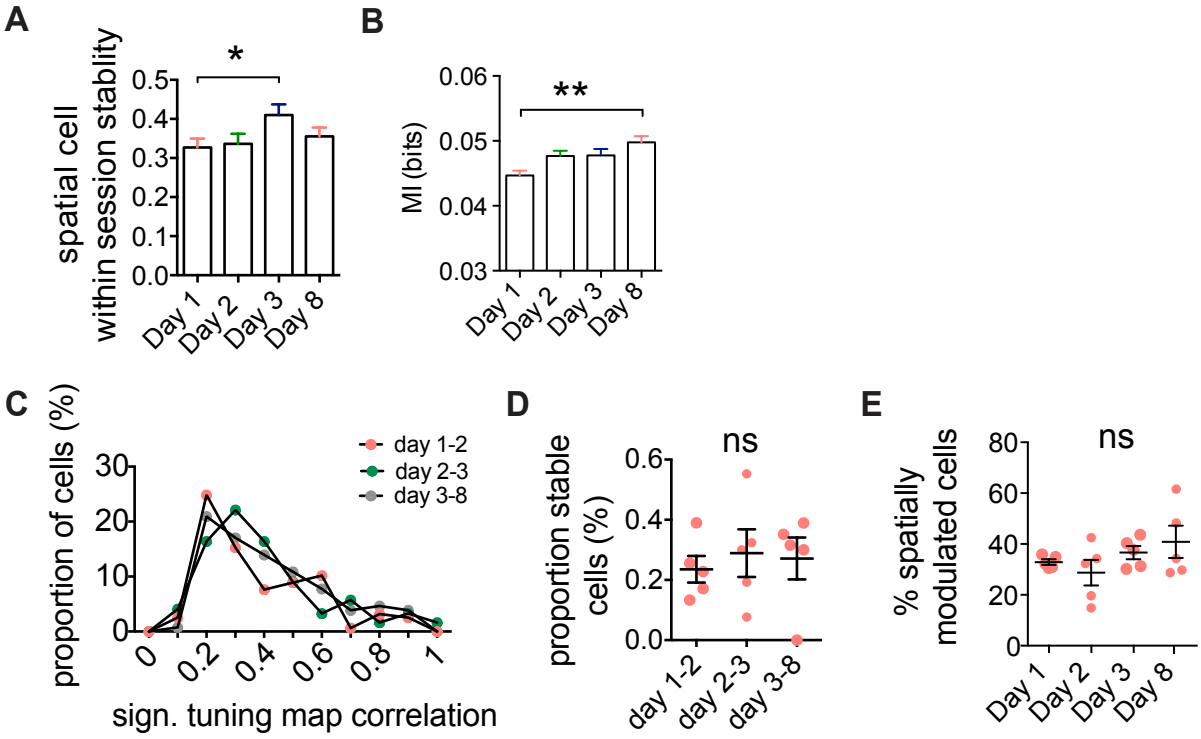

S15 Fig

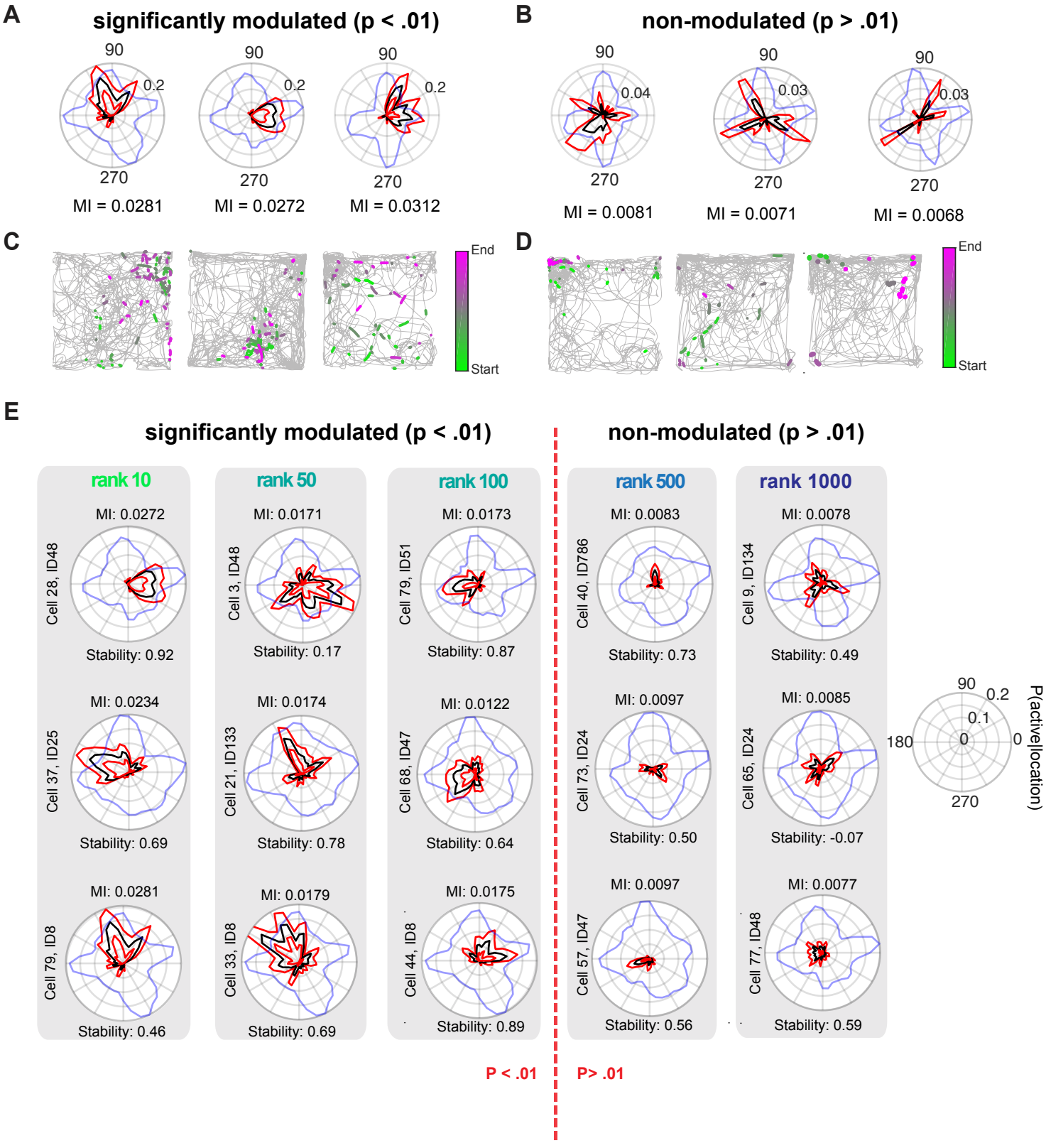

S16 Fig

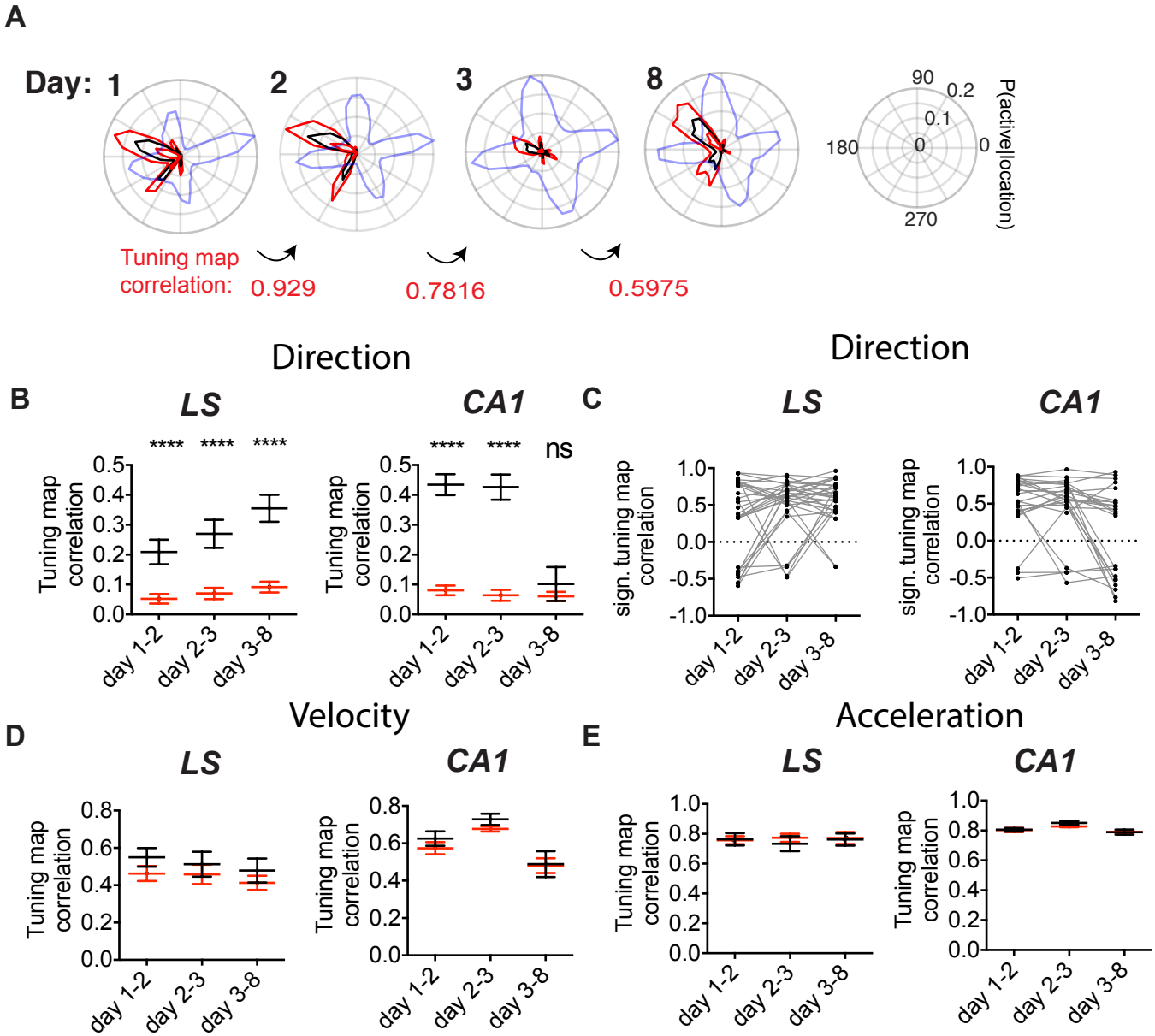

S17 Fig

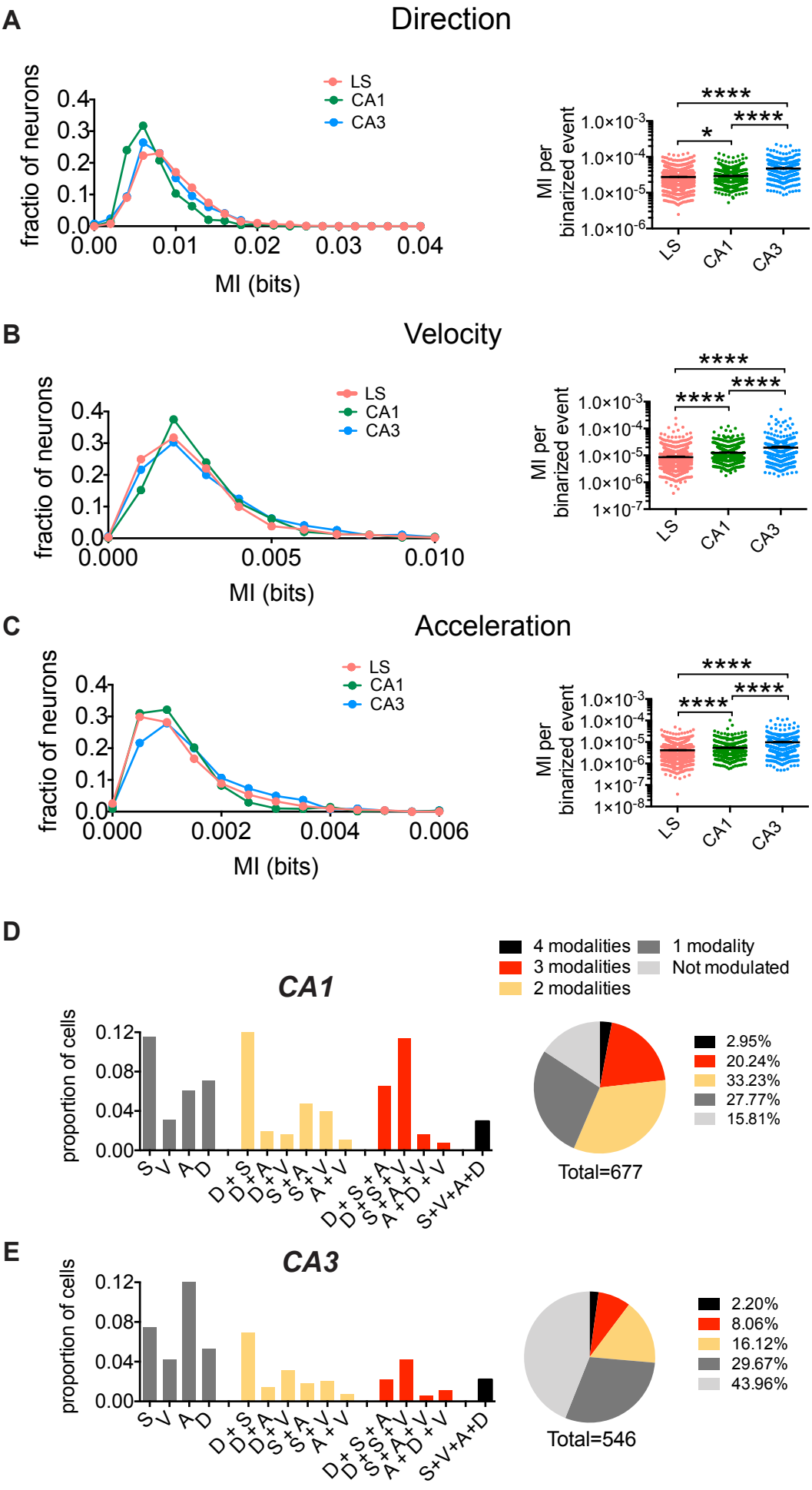

S18 Fig

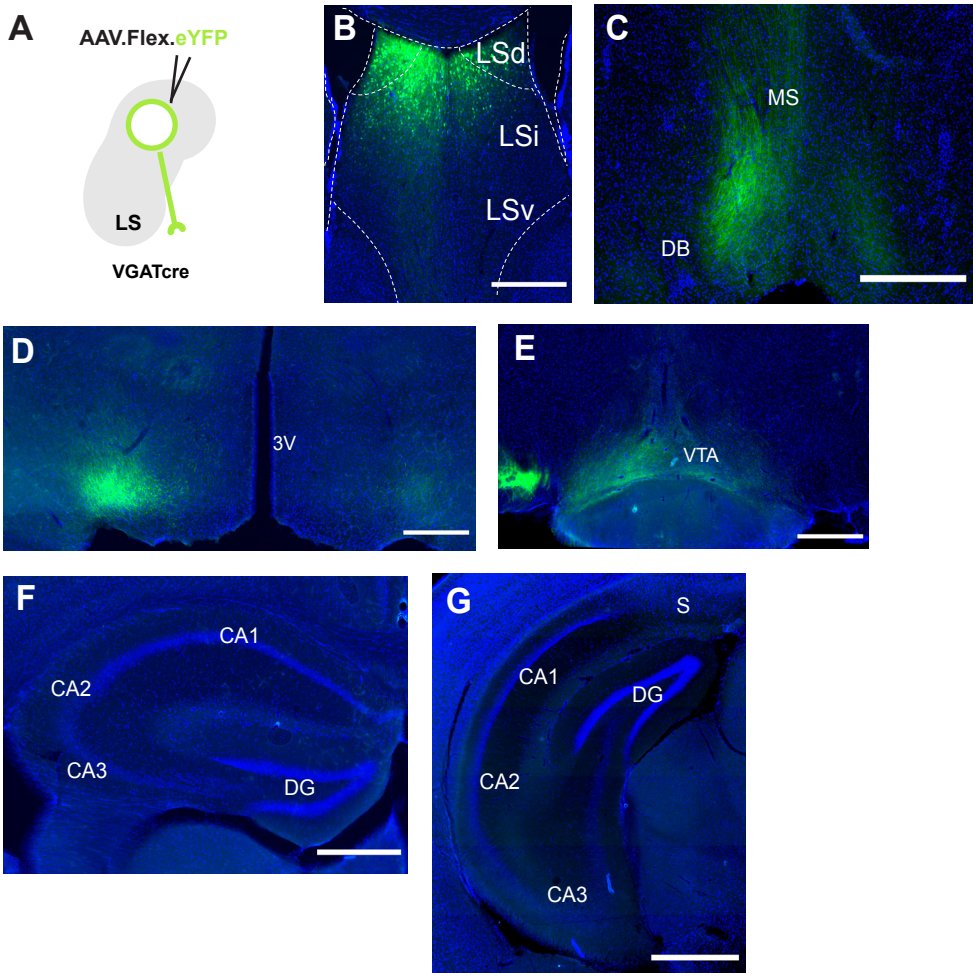

S19 Fig

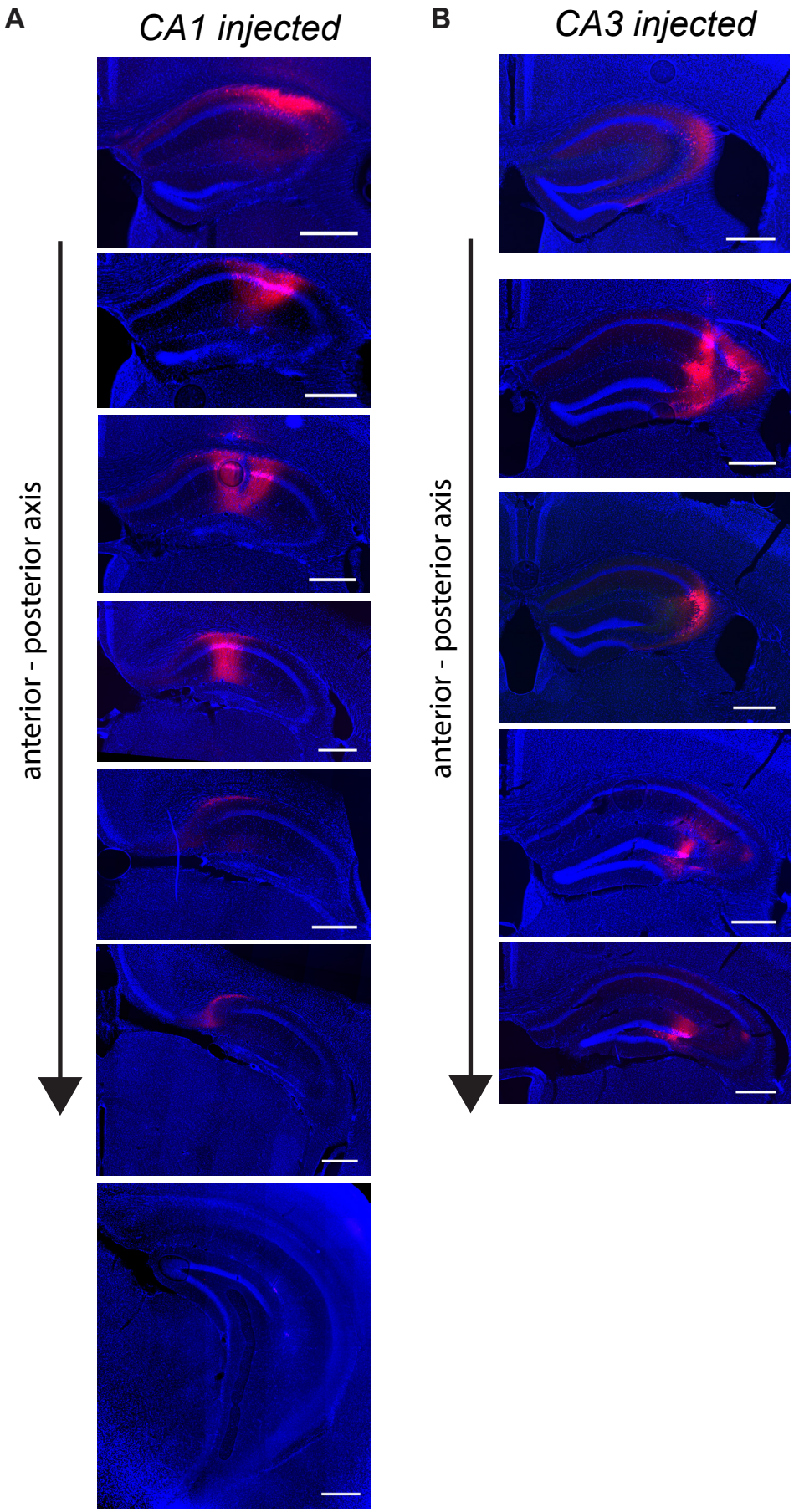

S20 Fig

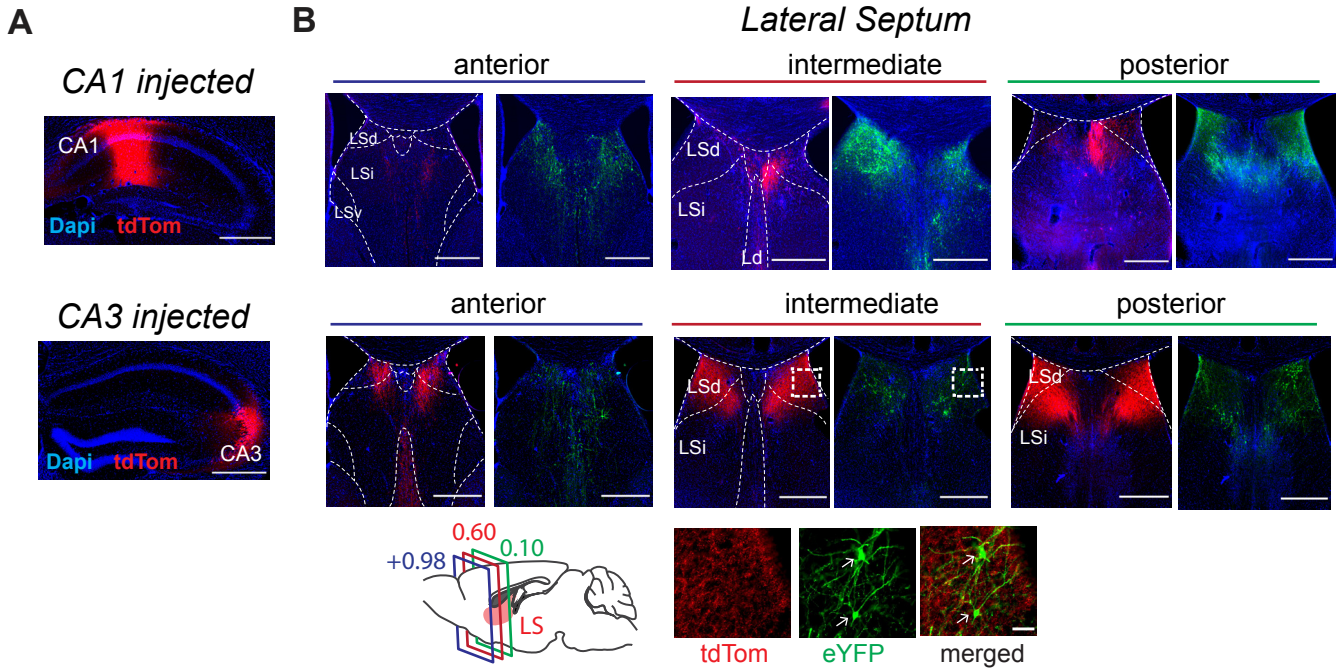

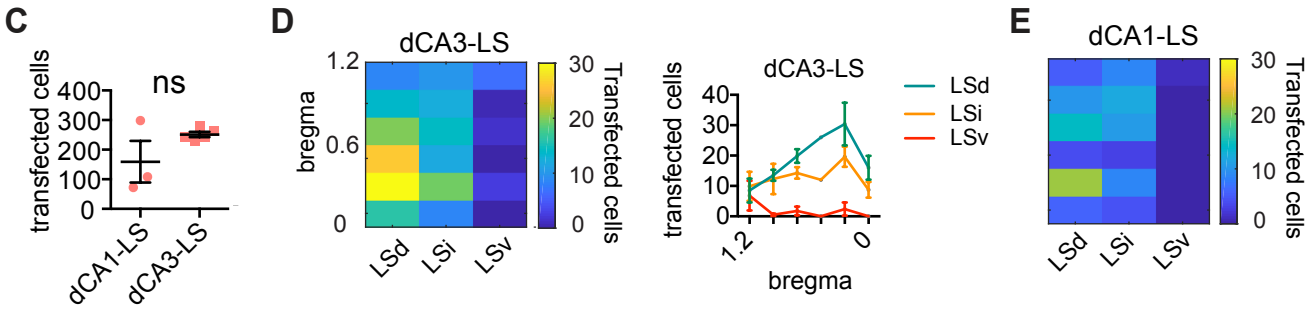

S21 Fig